Anti-Idling Systems for Service Vehicles with A/C-R Units: Modeling, Holistic Control, and Experiments

by

Yanjun Huang

A thesis
presented to the University of Waterloo
in fulfillment of the
thesis requirement for the degree of
Doctor of Philosophy
in
Mechanical Engineering

Waterloo, Ontario, Canada, 2016

AUTHOR'S DECLARATION

I hereby declare that I am the sole author of this thesis. This is a true copy of the thesis, including any required final revisions, as accepted by my examiners.

I understand that my thesis may be made electronically available to the public.

Yanjun Huang

Abstract

As people have begun to pay more attention to energy conservation and emission reduction in recent years, anti-idling has become a growing concern for automobile engineers due to the low efficiency and high emissions caused by engine idling, i.e., the engine is running when the vehicle is not moving. Currently, different technologies and products have emerged in an effort to minimize engine idling. By studying and comparing most of these methods, the conclusion can be drawn that there is still much room to improve existing anti-idling technologies and products. As a result, the optimized Regenerative Auxiliary Power System (RAPS) is proposed.

Service vehicles usually refer to a class of vehicles that are used for special purposes, such as public buses, delivery trucks, and long-haul trucks. Among them, there are vehicles with auxiliary devices such as air conditioning or refrigeration (A/C-R) systems that are essential to be kept running regardless of the vehicle motion. In addition, such auxiliary systems usually account for a large portion of fuel from the tank. Food delivery trucks, tourist buses, and cement trucks are examples of such service vehicles. As a leading contributor to greenhouse gas emissions, these vehicles sometimes have to frequently idle to for example keep people comfortable, and keep food fresh on loading and unloading stops. This research is intended to develop and implement a novel RAPS for such service vehicles with the A/C-R system as the main auxiliary device. The proposed RAPS can not only electrify the auxiliary systems to achieve anti-idling but also use regenerative braking energy to power them.

As the main power consuming device, the A/C-R system should be treated carefully in terms of its efficiency and performance. Thus, the developments of an advanced controller for A/C-R system to minimize energy consumption and an optimum power management system to maximize the overall efficiency of the RAPS are the primary objectives of this thesis. In this thesis, a model predictive controller (MPC) is designed based on a new A/C-R simplified model to minimize the power consumption while meeting the temperature requirements. The controller is extensively validated under both common and frosting conditions. Meanwhile, after integrating the RAPS into a service vehicle, its powertrain turns into a parallel hybrid system due to the addition of an energy storage system (ESS). For the sake of maximizing the overall efficiency, RAPS requires a power management controller to determine the power flow between different energy sources. As a result, a predictive power management controller is developed to achieve this objective, where a regenerative

braking control strategy is developed to meet the driver's braking demand while recovering the maximum braking energy when vehicles brake. For the implementation of the above controllers, a holistic controller of the RAPS is designed to deal with the auxiliary power minimization and power management simultanously so as to maximize the overall energy efficiency and meet the high nonlinearities and wide operating conditions.

Acknowledgements

I would like to take this opportunity to express my deep gratitude and appreciation to those who have contributed to this achievement.

First and foremost, I would like to extend sincere gratitude to my supervisor, Professor Amir Khajepour for his intellectual guidance, constant encouragement and valuable experience from both academic and non-academic perspectives.

I would also like to thank the members of my thesis committee, Prof. Mehrdad Kazerani, Prof. Baris Fidan, and Prof. Cecile Devaud, for their insightful comments and suggestions on this work. Special thanks to Prof. Saeid Habibi for serving as my external committee member.

I am grateful to our partners in Laboratory for Alternative Energy Conversion at Simon Fraser University for making the experimental tests possible. Thanks also go to my friends and colleagues in Mechatronic Vehicle Systems Laboratory, who have made University of Waterloo and Waterloo-Kitchener region such an enjoyable place to study and live.

Financial support provided by Automotive Partnership Canada is gratefully acknowledged.

Finally and most importantly, I would like to express my heartfelt gratitude to my family (grandparents, parents, and elder sister) for their endless love and support. Profound thanks to my wife for her unfailing support, love, and concern all these years. Without them, this accomplishment would not have been possible.

Dedication

This thesis is dedicated to my beautiful, caring and supportive wife, Ruiping and our coming baby.

Table of Contents

AUTHOR'S DECLARATION ii
Abstract iii
Acknowledgements v
Dedication vi
List of Figures x
List of Tables xiv
Nomenclature xv
Chapter 1 Introduction 1
1.1 Objective 1
1.2 Outline 6
Chapter 2 Literature Review 7
2.1 Anti-idling Technologies and Products 7
2.1.1 Mobile Anti-idling Products 7
2.1.2 Stationary Anti-idling Products 10
2.1.3 Summary 11
2.2 A/C-R System Modeling and Control Strategies 12
2.2.1 The Modeling Methods of A/C-R Systems 12
2.2.2 The Control Strategies of A/C-R Systems 14
2.2.3 Summary 18
2.3 Power Management Control Strategies in Hybrid Electric Vehicles 19
2.3.1 Rule-Based Control Strategies 20
2.3.2 Optimization-Based Control Strategies 21
2.3.3 Summary 25
Chapter 3 Modeling of the A/C-R System and RAPS 27
3.1 Potential Configurations of RAPS 27
3.1.1 Power Takeoff via Serpentine Belt 27
3.1.2 Power Takeoff from PTOs 27
3.2 Modeling of the Powertrain System 28
3.2.1 Longitudinal Dynamics of Vehicle 28
3.2.2 Engine 29
3.2.3 Alternator 30

3.2.4 Battery 30
3.3 Modeling of A/C-R Systems 31
3.3.1 Evaporator 32
3.3.2 Condenser 39
3.3.3 Compressor 40
3.3.4 Expansion Valve 41
3.3.5 Other Components 41
3.3.6 The Cargo Space Model 41
3.3.7 MATLAB/Simulink Model 43
3.4 Summary 44
Chapter 4 Experimental Studies and Model Validation 45
4.1 Experimental A/C-R System 45
4.2 Validation 47
4.2.1 Parameter Estimation 47
4.2.2 Comparison Results 50
4.3 Experimental Powertrain System 54
4.4 Summary 55
Chapter 5 Development of A/C-R Controllers and Analysis 56
5.1 Controller Development 56
5.1.1 On/off Controller 56
5.1.2 PI Controller 57
5.1.3 Set-point Controller 58
5.1.4 Nonlinear MPC 61
5.1.5 Linear MPC 63
5.2 Real Performance Comparison 66
5.2.1 On/off Controller 67
5.2.2 Set-point Controller 68
5.2.3 Discrete Linear MPC 71
5.2.4 Result Comparison 75
5.3 Case Study 75
5.3.1 Hybrid Controllers 76
5.3.2 Continuous MPC 76

5.3.3 Controllers Comparison 76
5.3.4 Results Analysis 79
5.4 Summary 79
Chapter 6 Power Management Control Systems for RAPS 81
6.1 Regenerative Braking Controller Development 81
6.1.1 Braking Force Allocation between Mechanical and Electric 81
6.2 MPC-based PMS Development for RAPS 83
6.2.1 Known Drive Cycles 83
6.2.2 Unknown Drive Cycles 93
Chapter 7 Holistic Controller Development for the Whole System 104
7.1 Holistic Controller Configuration and Modeling 104
7.2 Case study 105
7.2.1 Drive Cycle 105
7.2.2 Service Cycle 106
7.2.3 Results Analysis 107
Chapter 8 Conclusions and Future Work 112
Bibliography 115
Appendix A 128
Appendix B 130

List of Figures

Figure 1.1 Structural diagram of RAPS with the holistic controller 2
Figure 2.1 Thermo King APU [19] 8
Figure 2.2 ABP unit from eCAMION [21] 9
Figure 2.3 Hybrid trucks from Freightliner [26] 10
Figure 2.4 Advanced Travel Center Electrification services by IdleAir [29] 11
Figure 2.5 Power management strategies currently used in literature 19
Figure 2.6 MPC-based PMS types 25
Figure 3.1 RAPS configuration for light (a) and heavy (b) service vehicles 28
Figure 3.2 Schematic of the RAPS with light service vehicle 28
Figure 3.3 Schematic diagram of A/C-R system 32
Figure 3.4 Vapor compression cycle in a $h-\log(p)$ diagram [36] 32
Figure 3.5 Fin-tube evaporator with plate fins 32
Figure 3.6 Microchannel condenser with louver fins 32
Figure 3.7 Two-zone mode of evaporator and condenser 34
Figure 3.8 Schematic of evaporator with equivalent parameters 36
Figure 3.9 Schematic of heat transfer processes in the cargo space model [36] 42
Figure 3.10 Heat exchanger model structure diagram 43
Figure 3.11 Simulink model of A/C-R system with the cargo space 44
Figure 4.1 Schematic of the A/C-R system 45
Figure 4.2 Experimental A/C-R system 45
Figure 4.3 Chamber 46
Figure 4.4 Refrigerant mass flow meter 46
Figure 4.5 Thermocouple &pressure transducer 46
Figure 4.6 Air temperature & velocity sensors 46
Figure 4.7 Schematic of the whole experimental system 46
Figure 4.8 Inputs of the system 50
Figure 4.9 Air temperature at the outlet of two heat exchangers 50
Figure 4.10 Refrigerant temperature at inlet and outlet of evaporator 51
Figure 4.11 Refrigerant temperature at inlet and outlet of condenser 51
Figure 4.12 Pressures of evaporator and condenser 51
Figure 4.13 Inputs of the system 51

Figure 4.14 Air temperature at the outlet of two heat exchangers..... 52
Figure 4.15 Refrigerant temperature at inlet and outlet of evaporator..... 52
Figure 4.16 Refrigerant temperature at inlet and outlet of condenser..... 52
Figure 4.17 Pressures of evaporator and condenser..... 52
Figure 4.18 Inputs of the system..... 53
Figure 4.19 Air temperature at the outlet of two heat exchangers..... 53
Figure 4.20 Refrigerant temperature at inlet and outlet of evaporator..... 53
Figure 4.21 Refrigerant temperature at inlet and outlet of condenser..... 53
Figure 4.22 Pressures of evaporator and condenser..... 54
Figure 4.23 HIL setup..... 55
Figure 4.24 The controllable heater..... 55
Figure 5.1 Diagram of the on/off controller..... 56
Figure 5.2 PI controller model structure diagram..... 58
Figure 5.3 A/C-R system power consumption with respect to two pressures..... 58
Figure 5.4 Diagram of A/C-R system with set-point controller..... 60
Figure 5.5 The optimizer developing process..... 60
Figure 5.6 Illustration of the MPC scheme [134]..... 62
Figure 5.7 MPC structure in LabVIEW..... 65
Figure 5.8 Discrete MPC structure in LabVIEW..... 65
Figure 5.9 Diagram of experimental system with controllers..... 66
Figure 5.10 Controlled temperature under case1..... 67
Figure 5.11 System inputs under case1..... 67
Figure 5.12 Controlled temperature under case2..... 68
Figure 5.13 System inputs under case2..... 68
Figure 5.14 Controlled temperature under case3..... 68
Figure 5.15 System inputs under case3..... 68
Figure 5.16 Controlled temperature under case1..... 69
Figure 5.17 System inputs under case1..... 69
Figure 5.18 Pressures response under case1..... 70
Figure 5.19 Controlled temperature under case2..... 70
Figure 5.20 System inputs under case2..... 70
Figure 5.21 Pressures response under case2..... 70

Figure 5.22 Controlled temperature under case3 70
Figure 5.23 System inputs under case3 70
Figure 5.24 Pressures response under case2 71
Figure 5.25 Controlled temperature under case1 72
Figure 5.26 System inputs under case1 72
Figure 5.27 Controlled temperature under case2 73
Figure 5.28 System inputs under case2 73
Figure 5.29 Controlled temperature under case3 73
Figure 5.30 System inputs under case3 73
Figure 5.31 TXV without frost 74
Figure 5.32 TXV with frost 74
Figure 5.33 Temperature performance under the first scenario 74
Figure 5.34 System inputs under the first scenario 74
Figure 5.35 Temperature performance under second scenario 74
Figure 5.36 System inputs under second scenario 74
Figure 5.37 A heating load pattern 77
Figure 5.38 Temperature performance and energy consumption 77
Figure 5.39 System inputs of on/off controller 77
Figure 5.40 Temperature performance and energy consumption 77
Figure 5.41 System inputs of discrete MPC 77
Figure 5.42 Temperature performance and energy consumption 78
Figure 5.43 System inputs of discrete MPC 78
Figure 5.44 Temperature performance and energy consumption 78
Figure 5.45 System inputs of adaptive hybrid controller 78
Figure 5.46 Temperature performance and energy consumption 79
Figure 5.47 System inputs of continuous MPC 79
Figure 6.1 Drive cycles and prediction points of the proposed MPC 87
Figure 6.2 The ambient temperature and corresponding HL 88
Figure 6.3 Vehicle mass, extra HL, and total HL 88
Figure 6.4 Drive cycles under two scenarios 89
Figure 6.5 Drive cycles of UDDS and vehicle power 89
Figure 6.6 System inputs under scenario 1 91

Figure 6.7 System inputs under scenario 2 91
Figure 6.8 SoC responses under scenario 1 91
Figure 6.9 SoC responses under scenario 2 91
Figure 6.10 Vehicle mass estimation under scenario 1 92
Figure 6.11 Vehicle mass estimation under scenario 2 92
Figure 6.12 Driving information of UDDS 94
Figure 6.13 Vehicle power with the moving window 94
Figure 6.14 Vehicle power with a 50s window 95
Figure 6.15 Vehicle power with a 100s window 95
Figure 6.16 Vehicle power with a 200s window 95
Figure 6.17 Vehicle power estimation 96
Figure 6.18 SoC performance of different MPC 97
Figure 6.19 system input and engine efficiency 98
Figure 6.20 SoC performance of different MPC 99
Figure 6.21 System input and engine efficiency 100
Figure 6.22 Combined drive cycle 101
Figure 6.23 SoC performance of different MPC 101
Figure 6.24 System input and engine efficiency 102
Figure 7.1 Whole structure of the RAPS with the holistic controller 105
Figure 7.2 Nominal and real drive cycles 106
Figure 7.3 Ambient temperature and HL 106
Figure 7.4 SoC trajectories 108
Figure 7.5 Temperature performance of the cargo 108
Figure 7.6 Speed of the compressor 108
Figure 7.7 Frequency of the evaporator fan VFD 109
Figure 7.8 Frequency of the condenser fan VFD 109
Figure 7.9 Direct charging power 109
Figure 7.10 Temperature of the cargo in the conventional vehicle 110
Figure 7.11 A/C-R system inputs in the conventional vehicle 110

List of Tables

Table 4.1 The known and identified parameters at one steady state 49
Table 4.2 The MPAE between simulation and test data 54
Table 5.1 Operating conditions and constraints of inputs and states 66
Table 5.2 Experimental cases 67
Table 5.3 controller gains and parameters 69
Table 5.4 MPC parameters 72
Table 5.5 Result comparison of controllers 75
Table 5.6 Energy consumptions under different heating load conditions 75
Table 5.7 Energy consumptions of different controllers 79
Table 6.1 drive cycles 88
Table 6.2 Driving power and auxiliary power 90
Table 6.3 MPC Parameters 90
Table 6.4 Result comparison of Two Scenarios 93
Table 6.5 MPC Types 96
Table 6.6 MPC Parameters 97
Table 6.7 Result comparison for each MPC 99
Table 6.8 Result Comparison for each MPC 100
Table 6.9 Combined Drive cycle 101
Table 6.10 Result comparison for each MPC 102
Table 7.1 Drive cycles 105
Table 7.2 MPC Parameters 107
Table 7.3 Result comparison for each MPC 111

Nomenclature

ABP	Auxiliary battery powered units
AI	Artificial intelligence
ANN	Artificial neural network
APU	Auxiliary power unit
CAN	Controller area network
COP	Coefficient of performance
DAQ	Data Acquisition
DP	Dynamic programming
ECMS	Equivalent fuel consumption minimization strategy
ESS	Electric storage system
EVs	Electric vehicles
FC	Fuel consumption
FTP75	Federal Test Procedure
GA	Genetic algorithm
HEVs	Hybrid electric vehicles
HIL	Hardware-in-the-loop
HVAC	Heating ventilation air conditioning
HWFET	Highway Fuel Economy Test
MIMO	Multi-input Multi-output
MPC	Model predictive control
NI	National instrument
PID	Proportional–integral–derivative
PMS	Power management strategy
PTO	Power takeoff
QP	Quadratic problem
RAPS	Regenerative auxiliary power system
SISO	Single-input single-output
SMC	Sliding mode control
SoC	State of charge
TXV	Thermostatic expansion valve

UDDS	Urban dynamometer driving schedule
VFD	Variable frequency drive
A_c	Sectional area of the condenser tube
A_e	Sectional area of the evaporator tube
A_f	Frontal area of the vehicle
A_i	Interior area of heat exchanger
A_{oe}	Total outside area of the tube wall & fins
A_v	Area of the valve opening
α_{ic}	Heat transfer coefficient of two-phase section in condenser
α_{icsh}	Heat transfer coefficient of superheat section in condenser
α_{ie}	Heat transfer coefficient of two-phase section in evaporator
α_{iesh}	Heat transfer coefficient of superheat section in evaporator
α_{oc}	Air-side heat transfer coefficient in condenser
α_{oc0}	Initial air-side heat transfer coefficient in condenser
α_{oe}	Air-side heat transfer coefficient in evaporator
α_{oe0}	Initial air-side heat transfer coefficient in evaporator
C_{batt}	Nominal capacity of the battery
C_D	Coefficient of aerodynamic resistance
C_p	Thermal conductivity of air
C_{p_air}	Specific heat of the air
C_r	Coefficient of rolling resistance
C_v	Discharge coefficient
D_{ic}	Inner diameter of the tube in condenser
D_{ie}	Inner diameter of the tube in evaporator
f_q	Heat loss factor
F_a	Aerodynamics resistance
F_g	Grade resistance

F_r	Tire rolling resistance
F_x	Vehicle longitudinal force
F_z	Vehicle normal force
G	Air mass flux across the heat exchanger
h_g	Enthalpy of gas refrigerant
h_{ic}	Enthalpy of refrigerant at the inlet of compressor
h_{ie}	Enthalpy of refrigerant at the inlet of evaporator
h_{is}	Isentropic enthalpy of refrigerant during the compression process
h_l	Enthalpy of liquid refrigerant
h_{le}	Enthalpy of liquid refrigerant at the inlet of evaporator
h_{lg}	Latent enthalpy of refrigerant
h_{oc}	Enthalpy at the outlet of condenser
j	Colburn factor
k_p	Controller gain
k_i	Controller gain
l_c	Length of the two-phase section of the condenser
l_e	Length of the two-phase section of the evaporator
L_c	Total length of the condenser tube wall
L_e	Total length of the evaporator tube wall
$\dot{m}_{air}$	Air mass flow rate
$\dot{m}_{c\_air}$	Air mass flow rate of condenser fan
$\dot{m}_{comp}$	Mass flow of refrigerant through the compressor
$\dot{m}_{e\_air}$	Air mass flow rate of evaporator fan
$\dot{m}_F$	Fuel mass flow
m_{pipe}	Mass of refrigerant inside the pipe
m_{total}	Total mass of the refrigerant inside the whole system
$\dot{m}_v$	Refrigerant flow rate throughout the valve

N_{comp}	Compressor pump speed
N_{cond}	Condenser fan control signal
N_{evap}	Evaporator fan control signal
$N_{evap-mpc}$	Speed found by the discrete MPC at the switching point
P_{batt}	Battery power
P_{alt}	Electrical power
P_{aux}	Auxiliary system power
P_c	Pressure of condenser
P_e	Pressure of evaporator
P_{eng}	Engine power
$P_{eng \rightarrow alt}$	Engine power going to the alternator
$P_{eng \rightarrow veh}$	Engine power going to the vehicle
P_{reg}	Regenerative braking energy
P_{veh}	Vehicle power
$\dot{Q}_{cool}$	Cooling capacity generated by A/C-R system
$\dot{Q}_{door}$	Heating load due to door opening
$\dot{Q}_{load}$	total heating load applied onto the cargo
T_a	Mean air temperature around heat exchangers
T_{ac}	Mean air temperature around condenser
T_{ae}	Mean air temperature around evaporator
T_{amb}	Ambient temperature
T_{ao}	Air temperature at the outlet of heat exchanger
T_{ai}	Air temperature at the inlet of heat exchanger
$T_{c\_air\_in}$	Air temperature at the inlet of condenser
T_{cargo}	Cargo temperature
T_{cargo_init}	Cargo initial temperature

$T_{e\_air\_in}$	Air temperature at the inlet of evaporator
T_{eng}	Engine torque
$T_{eng \rightarrow alt}$	Engine torque goes to alternator
T_{ic}	Refrigerant temperature at the inlet of condenser
T_r	Refrigerant temperature
T_{rc}	Saturation temperature of refrigerant
T_s	Sampling time
T_{sh}	Superheat
$T_{setpoint}$	Temperature set point of the cargo
T_{wfc}	Equivalent temperature of tube wall & fins in condenser
T_{wfe}	Equivalent temperature of tube wall & fins in evaporator
V_d	Volumetric displacement of compressor
V_{ED}	Displacement
V_{OC}	Open circuit voltage
V_{veh}	Vehicle speed
$\dot{W}_{comp}$	Power consumption of compressor
$\dot{W}_{cond}$	Power consumption of condenser fan
$\dot{W}_{evap}$	Power consumption of evaporator fan
ρ_g	Density of vapor refrigerant
ρ_{gc}	Density of vapor refrigerant in condenser
ρ_{ge}	Density of vapor refrigerant in evaporator
ρ_{lc}	Density of liquid refrigerant in condenser
ρ_{le}	Density of liquid refrigerant in evaporator
ρ_{ref}	Density of refrigerant
ρ_{shc}	Refrigerant density of superheat region in condenser
ρ_{she}	Refrigerant density of superheat region in evaporator

ρ_l	Density of liquid refrigerant
$\overline{\gamma}_c$	Mean void fraction of two-phase section in condenser
$\overline{\gamma}_e$	Mean void fraction of two-phase section in evaporator
ω_{eng}	Angular velocity of the engine
η_a	Adiabatic efficiency of compressor
η_{alt}	Efficiency of the alternator
η_{char}	Charging efficiency of the battery
η_{dis}	Discharging efficiency of the battery
η_{eng}	Engine efficiency
η_{reg}	Regenerative braking efficiency
η_{tran}	Powertrain efficiency
η_{vol}	Volumetric efficiency of compressor

Chapter 1
Introduction

1.1 Objective

There are different auxiliary systems that are used in service vehicles. Engines sometimes have to idle to power these auxiliary systems during vehicle stops. Large diesel engines of long-haul trucks are designed to run at high speeds on highways and are able to reach efficiencies of more than 40%. However, when the engine idles, the efficiencies drop to 1-11% and more pollutants are release [1]. Although in recent years many types of anti-idling products have been introduced to reduce this kind of idling, there are still many improvements that need to be made. As a result, the optimum regenerative auxiliary power system (RAPS) proposed in this thesis not only satisfies the auxiliary power device (*e.g.* A/C-R system) requirements of service vehicles to achieve anti-idling but also maximizes the use of regenerative braking energy and fuel efficiency. The application of RAPS in current service trucks can significantly improve their fuel efficiencies and reduce emissions by elimination of idling.

Figure 1.1 shows the diagram of a RAPS with a holistic controller. The target vehicles of this research are service vehicles with A/C-R units as their main auxiliary power system. Thus, in the RAPS, there is a main power consumption source - the A/C-R system - and three energy providing sources - plug-in energy, regenerative braking energy, and the engine. Regarding high efficiency and energy saving, the following should occur: the A/C-R system should consume the minimum fuel while meeting the temperature or other requirements; the recovered kinetic energy during vehicle braking should be at maximum without affecting the drivability; the aforementioned power sources should be coordinated to pursue the maximum powertrain overall efficiency. Accordingly, the main roles of this thesis: development of a high efficient holistic controller, which is able to minimize the fuel consumption of A/C-R systems, maximize the recovered kinetic energy while maintaining the drivability, and coordinate different on-board power sources for the maximum powertrain efficiency.

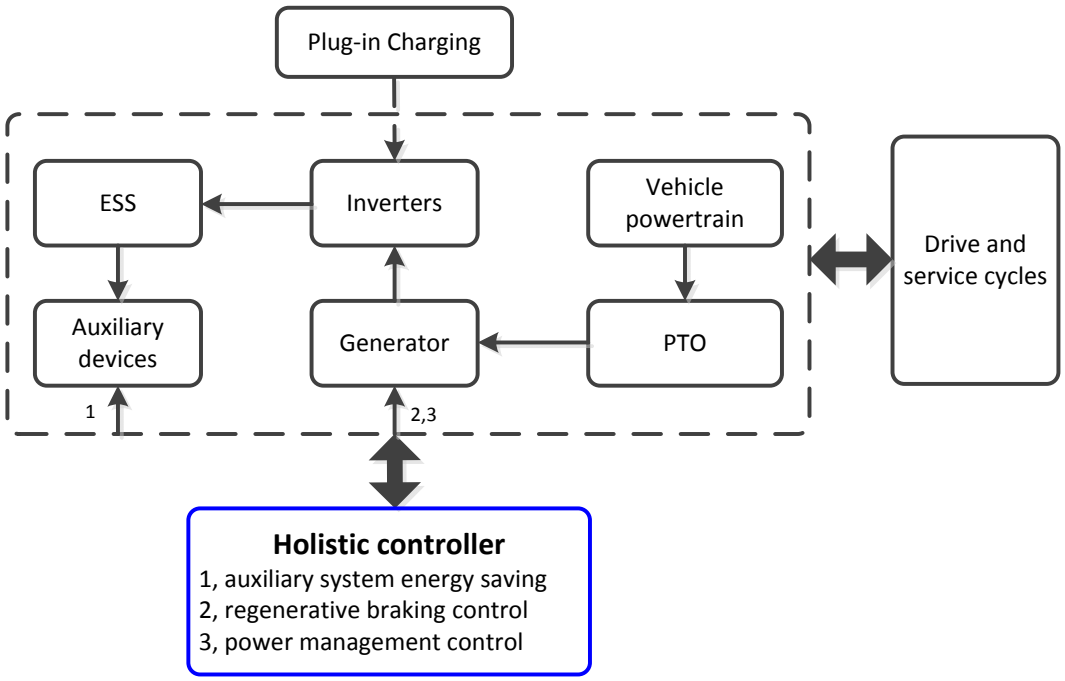

Figure 1.1 Structural diagram of RAPS with the holistic controller

The continuously increasing demands on lower emission levels and better fuel economy have driven researchers to develop more efficient, less polluting vehicles [2]. However, as the main auxiliary load of vehicles, the A/C-R systems can consume up to 25% of the total fuel or even more in long-haul service vehicles. In addition, as the main energy consumption source of the A/C-R system, the compressor is usually connected directly to the engine via a belt in conventional vehicles, such that engines sometimes have to idle to power A/C-R systems during vehicle stops. For example, long-haul trucks are equipped with a sleeper cabin where the drivers can live on the road [3]. Usually, trucks idle to provide power to the air conditioning system for cabin temperature control. Similarly, food service trucks need to idle to provide power to the refrigeration system while loading or unloading. When it comes to the vehicle idling, many drawbacks appear, such as the low efficiency of the engine and excessive emissions [1]. Thus, there are significant benefits in operating A/C-R systems efficiently, both in terms of both operating costs and their effects on the environment [4]. An important step in achieving better performance and higher energy efficiency is a control-based model and a proper control strategy [5].

Making more efficient auxiliary devices can definitely bring many benefits to vehicle owners as well as the environment. But in most conventional vehicles, the compressor speed is proportional to engine speed instead of actively varying [6]. This impedes the advanced controller development for

the automotive A/C-R system given that the controllers are usually applied to manipulate the speeds of compressor and fans. However, as the development of anti-idling technologies such as the Auxiliary Battery Powered (ABP) units, hybrid electric vehicles (HEVs) and electric vehicles (EVs), the on-board ESS is capable to power the A/C-R system independently such that the A/C-R system can be disconnected from the engines [7]. That means the electrification of the A/C-R system and then the application of advanced controller in vehicles are possible [6]. As a result, the idling caused by powering auxiliary devices when the vehicle stops can be eliminated such that the performance and efficiency of the automotive A/C-R system largely improved [8]. This can be achieved partially by developing advanced controllers to replace the conventional on/off (bang-bang) controllers.

The design of advanced controllers requires a control-based model of the A/C-R systems that is accurate but simple enough for real-time implementation. A control-based model is actually a trade-off between accuracy and simplicity. If the model is too simple, it will not be able to reflect the main characteristics of the system, resulting a poor closed-loop control performance. On the other hand, if it is too complex, it slows down the controller by increasing computation time, which may not be used in real-time implementations [9], though it can describe the dynamics of the system well enough and produce good predictions. Consequently, this study presents a simplified but accurate model for A/C-R systems that has been validated by experimental results, and then several controllers are designed, tested and compared to obtain the most promising one.

By introducing the RAPS to a conventional service vehicle, its powertrain turns into a parallel hybrid system due to the addition of a battery. The only difference from a standard parallel hybrid powertrain is that the ESS in RAPS only powers the auxiliary devices instead of assisting the engine in driving the vehicle. The ESS is able to power the auxiliary devices, such as an A/C-R system, independently so as to achieve the anti-idling purpose. For the sake of overall high efficiency, RAPS requires a power management strategy (PMS) to determine whether and when the ESS needs to be charged. Using the alternator connected to the engine via the serpentine belt or the gearbox via the power take-off (PTO), the RAPS is capable of recapturing a portion of the kinematic energy during vehicle braking. A strategy is used to guarantee the maximum braking energy recovered without affecting the drivability of the vehicle. Meanwhile, when the recaptured energy is not enough, the engine can directly charge the battery in an efficient way that is guaranteed by the developed MPC PMS [10]. Thus, these characteristics differentiate it from the existing auxiliary power unit (APU) and ABP.

In development of the above controllers, each controller is designed individually although the communications between them are considered as the predefined. For instance, the power consumption of the A/C-R system is preset and varied proportionally with the ambient temperature. However, under the real conditions, its power consumption should be optimized by its own controller and sent to the power management controller to coordinate the power flows. Therefore, a holistic controller is developed by combining the aforementioned controllers to automatically deal with the mutual communications. Actually, the holistic controller is a centralized MPC to guarantee the service vehicle saving energy by achieving three objectives: minimize the energy consumption of the auxiliary systems, maximize the energy recovered when braking happens, and optimize the output power of the engine. Thanks to the multi-objective optimization feature of the MPC, the proposed holistic controller optimizes the power consumption of auxiliary systems and power flow of the powertrain simultaneously for the first time. In order to show the advantages brought by the proposed RAPS with the controller over the conventional vehicles, a case study is performed and analyzed. The results demonstrate that the RAPS can help a light service vehicle to eliminate idling and obviously save fuel under the study scenario.

In general, the contributions of this thesis are:

I. A control-oriented dynamic model of an A/C-R system based on the moving boundary and lumped parameter method is developed and validated experimentally. Unlike existing models, the proposed model lumps the fins' effects into two equivalent parameters without adding any complexity and considers the effect brought by the superheat section of the condenser, resulting in a model that is not only simpler but also more accurate than the existing models.

II. A set-point controller is proposed for A/C-R system with two different time-scale layers. The outer or the slow time-scale layer called a set-point optimizer is used to find the set points related to energy efficiency by using the steady state model; whereas, the inner or the fast time-scale layer is used to track the obtained set points. In the inner loop, thanks to its robustness, an SMC is utilized to track the set point of the cargo temperature. The experimental results under several disturbed scenarios are analyzed to demonstrate how the proposed controller can improve performance while reducing the energy consumption by 9% comparing with the on/off controller. The controller is suitable for any type of A/C-R system even though it is applied to an automotive A/C-R system.

III. To study the potential energy saving for A/C-R systems, a discrete MPC is designed based on the proposed model for an automotive A/C-R system with a three-speed compressor. A proper terminal

weight is chosen to guarantee its robustness under both regular and frost conditions. Following that, a case study is conducted under various heating load conditions. Two hybrid controllers are made; these combine the advantages of both the on/off controller and discrete MPC such that they will be more efficient under any ambient heating condition. In addition, a continuous MPC is developed for systems with continuous variable components. Finally, the experimental and simulation results of the new controllers and the conventional on/off controller are provided and compared to show that the proposed controllers can save up to 23% more energy.

IV. Since service vehicles, such as delivery trucks or public buses, usually have predetermined routes, thus, it is possible and beneficial to utilize an MPC to improve the fuel economy of RAPS. However, the mass/load of such service vehicles is time-varying during a drive cycle. Therefore, an adaptive predictive power management controller is designed to account for the time-varying load of service vehicles. Although the drive cycle is preset, it would experience uncertainties or disturbances caused by traffic or weather conditions in real situations. To deal with this problem, a large step size prediction method is used in the adaptive MPC to enhance its robustness. The proposed adaptive MPC is compared with a prescient MPC in different scenarios to demonstrate its applicability and optimality. The proposed approach is independent of the powertrain topology such that it can be directly extended to other types of HEVs.

V. To loosen the assumption that the route is preset, an average concept based MPC is developed to improve the overall efficiency of the RAPS without a priori driving information. The analysis shows that the RAPS with the proposed MPC obviously decreases the total fuel consumption. Meanwhile, the average concept based MPC has a similar performance as the prescient MPC. In addition, the robustness of this MPC is also tested under other drive cycles. The proposed MPC is independent of powertrain topology such that it can be straightforwardly extended to other types of HEVs, and it provides a way to apply the MPC even though the future driving information is unavailable.

VI. For the sake of ease of implementation of the above controllers, a holistic controller of a RAPS is designed for service vehicles to reduce engine idling. The proposed controller is an MPC to guarantee the service vehicle saving energy by achieving three objectives: minimize the energy consumption of the auxiliary systems, maximize the regenerative braking energy and optimize the output power of the engine. Thanks to the multi-objective optimization feature of the MPC, the proposed holistic controller optimizes the power consumption of auxiliary systems and power flow of the powertrain simultaneously for the first time. In order to show the advantages brought by the

proposed RAPS with the controller over the conventional vehicles, a case study is performed and analyzed. The results demonstrate that the RAPS can help a light service vehicle significantly save fuel under the study scenario and save more for heavy vehicles.

1.2 Outline

This thesis is organized as follows:

Chapter 2 presents a literature review on three different aspects. Firstly, the available anti-idling products and technologies in the market are studied and compared. The advantages of the proposed RAPS over such products are identified. Secondly, the modeling methods and control schemes used in all-purpose A/C-R systems are reviewed. Thirdly, power management strategies utilized in HEVs, especially the MPC-based, are studied.

Chapter 3 begins by showing two potential structures of the RAPS for service vehicles and describes how to model the powertrain system as well as the A/C-R system.

Chapter 4 briefly introduces the experimental A/C-R system and powertrain system, and then comprehensively validates the models built in Chapter 3 by test data obtained from the experimental systems.

Chapter 5 elaborates the development process of several controllers for the A/C-R system and then implements them experimentally. After that, the real performance of all the controllers are presented and compared under several preset working conditions. Finally, the performance of the controllers is tested in a more realistic scenario to obtain a more efficient controller under any working conditions.

Chapter 6 firstly shows a regenerative braking strategy to maximize the energy recovery while sustaining the drivability of the vehicle. Then, the predictive power management strategies are developed under two scenarios: with and without knowing the future drive cycles as a priori.

Chapter 7 presents a centralized MPC as the holistic controller for RAPS, which combines the aforementioned controllers. Although all the individual controllers are developed and their performance is verified, they should communicate with each other when they are working. Therefore, a centralized controller is needed to guarantee the stability of the controlled system.

Chapter 8 draws the conclusions and discusses the future work.

Chapter 2
Literature Review

In this chapter, the literature review is divided into three sections. Firstly, the current anti-idling technologies and products are discussed, followed by the modeling and control strategies of A/C-R systems. Lastly, the existing power management control strategies, especially the MPC-based, used in hybrid powertrains are examined.

2.1 Anti-idling Technologies and Products

Idling refers to a situation when the engine is running but the vehicle is not moving. It is one of the main contributors to poor air quality, extreme noise pollution, and serious health issues. In addition, it impacts drivers, site personnel at stations or nearby [11], and increases costs for drivers or companies. For example, diesel engines have efficiencies of 40% running at highways, however, when idling their efficiencies drop to 1-11% and discharge more pollutants. As such, it is imperative to reduce or even eliminate automotive idling. There are many quantitative studies [12-16] to demonstrate its negative impacts along with many corresponding regulations and bylaws, which require a complete ban on idling in many countries [12-13].

Due to the urgent demand for high fuel economy and low emissions in the automotive industry, a number of anti-idling technologies have emerged over the last several decades [11-16]. A variety of products with exclusive functionalities have been developed by different manufacturers. In general, according to a comprehensive review of existing literature, two main classification methods were employed to categorize these technologies. First of all, the mobile and stationary products are utilized to differentiate the products whether move with vehicles or not [12]. In addition, they can be classified as fully functional and partial functional types depending on whether they can provide all power required by auxiliary systems.

2.1.1 Mobile Anti-idling Products

Mobile systems are installed in and moving with vehicles, including automatic engine shutdown devices, APUs, ABPs, and a number of individual components designed to meet part of the heating, cooling, and other requirements [11]. Among them, APUs and ABPs can fully provide the desired power, referred to as the fully functional type; while the other types belong to the partial functional type because they can only provide limited functionalities such as either heating or cooling.

2.1.1.1 APUs/Generator sets

APUs, or fuel-fired APUs, are the most conventional and popular anti-idling solutions. APU consists of a comparatively small engine and an alternator that is fully integrated into a vehicle's existing heating, ventilating, and air conditioning (HVAC) as well as the battery charging system [11]. Many types of APUs have been proposed and manufactured by different companies, such as Thermo King, Carrier, Pony Pack, Dometic, RigMaster Power, Dynasys, and Ecamion. For more information about corresponding APUs, please refer to [17] or their official websites. Test results of several APUs are also examined by [18].

Figure 2.1 Thermo King APU [19]

APUs usually can provide all the auxiliary power demanded by vehicles or drivers, and can thus reduce engine idling. Nevertheless, the addition of external components makes vehicles more expensive, heavier, noisier, and more maintenance intensive. Besides, the added engine may eventually produce more pollutes than the main engine if not properly designed [11].

2.1.1.2 ABPs with Inverters

Recently, ABPs [20] have emerged as a competitive alternative to conventional APUs. The additional engine and generator in conventional APUs are replaced by a package of batteries, which offer the same functionalities without the extra emissions or noise asSoCiated with their conventional counterparts. The batteries are either charged by the engine during operation or charged by stationary type anti-idling devices (*e.g.*, Shorepower); and discharged when the vehicle stops. Inverters are capable of converting the battery power into the desired AC power for other appliances or accessories.

Figure 2.2 ABP unit from eCAMION [21]

However, ABPs should confront some problems asSoCiated with batteries, such as the short lifecycle, and the asSoCiated costs, among others without properly being designed. As a result, other technologies have been proposed to replace the battery, including fuel cell systems and solar energy systems, but they are still in their early development stages. The shortcomings of these alternatives including expensive materials, large modification of the existing structure, and longer start-up times impede their popularization [3].

2.1.1.3 Hybrid Electric Trucks

In 2003, GM introduced a hybrid diesel-electric military light truck equipped with a diesel engine and a fuel cell APU. Hybrid electric light trucks were proposed in 2004 by Mercedes-Benz [21], and after that, many truck companies have developed their own hybrid trucks and buses. As one of the most famous companies that develop and manufactures hybrid commercial vehicles [23], Eaton, currently, provides both electric and hydraulic hybrid powertrain systems. In Freightliner, the anti-idling technology employed by the M2 106 diesel-electric hybrid uses an optional electronic PTO (ePTO) to reduce idling, which makes the vehicle suitable for high-idling applications such as utility and tree-trimming. Idling time is reduced by up to 87%, and fuel consumption up to 60% in ePTO mode. Truckers can also add an optional 5 kW auxiliary power generation (APG) unit and realize additional savings [24]. Other truck companies such as Mitsubishi Fuso Truck & Bus Corporation [25], Hino Motors, and UD Trucks also have their own hybrid products and adopt similar technologies to minimize the amount of idling time.

Figure 2.3 Hybrid trucks from Freightliner [26]

2.1.1.4 Automatic Shut-down/turn-on Systems

Automatic shut-down/turn-on systems are referred to as engine management systems, and allow truckers to program their engines to turn on or off in accordance to some specific parameters, which include, for example, a preset period of time, compartment or engine temperature, and/or battery voltage. They are easy to install and costless, and capable of reducing idling to some extent. Nevertheless, they cannot power HVAC system and other appliances. Above all, they cannot address the inherent inefficiencies asSoCiated with idled engines [12].

2.1.1.5 Direct-fired Heaters and Thermal Energy Storage (TES)

According to a study conducted by American Transportation Research Institute (ATRI), direct-fired heaters are one of the most popular idle-reduction technologies [27]. The working principle is that one portion of fuel is imported from the fuel tank and burnt in a small assembly, usually mounted beneath the bunk. It helps provide cabin space heating [11]. Instead, TES is charged during the daytime when the truck is being driven and uses an innovative cold storage cell to provide cooling for the driver at night without starting the engine.

2.1.2 Stationary Anti-idling Products

Stationary anti-idling products are fixed in locations where truckers can purchase services such as heating, cooling, electricity, and the Internet. They are also referred to as truck stop electrification (TSE) systems and classified as either onboard (dual system) or off-board (single system) systems. Onboard systems (*e.g.*, Shorepower Technology and CabAire LLC [28]) require the installation of

dedicated heating and cooling systems and inverters in the truck, while off-board systems (IdleAire, Envirodock and AireDock [28]) offer heating, cooling, and electricity through an external device [12].

Figure 2.4 Advanced Travel Center Electrification services by IdleAir [29]

2.1.3 Summary

According to pros and cons of the aforementioned anti-idling products, to achieve the goal of anti-idling in service vehicles with auxiliary devices such as A/C-R systems, APUs, and ABPs capable of providing enough power can be integrated into such vehicles. Besides, as a significant feature of the hybrid technologies, anti-idling can be achieved by hybrid vehicles. Nonetheless, the optimized RAPS presented in Figure 1.1 can be a promising alternative compared to its counterparts. After component-sizing via multi-disciplinary optimization, the optimized RAPS can be more compact, light-weight, and efficient, thus requiring less modification to the vehicles and fewer costs to the owners. It is able to not only satisfy power requirements of service vehicles but also utilize the recovered braking energy to maximize the fuel economy. Above all, compared to the aforementioned of anti-idling technologies, the optimized RAPS have the following main advantages: firstly, the optimized RAPS does not contain a small-scaled engine, therefore, it will be quieter and cleaner than the conventional APUs. Secondly, the optimized RAPS is similar to an ABP, but has the ability to recapture braking energy, therefore, a smaller battery pack can meet the requirements, resulting in lower costs after sizing the component. Thirdly, the developed PMS will guarantee the powertrain working in maximum efficiency. Lastly, the hybrid service vehicles are not very popular because of their high costs. Thus, the conventional ones will still dominate in the following decades. In the development process of HEVs, the auxiliary power is assumed as a constant or even neglected such

that the solutions will not be optimal. Therefore, the techniques adopted in the development process of RAPS can be directly extended to any types of HEVs.

2.2 A/C-R System Modeling and Control Strategies

A/C-R systems usually refer to vapor compression units, which operate on the vapor compression cycle and generally consist of a set of evaporator, compressor, expansive valve, and a condenser. They are extensively adopted in the automotive industry and have become the main auxiliary load on a vehicle engine or other energy sources when operating. Thus, there are significant benefits to operating A/C-R systems efficiently, both in terms of running costs, as well as its effect on the environment [30]. However, an indispensable factor to achieve good performance and efficient energy consumption is a control-based model and a proper control strategy [5].

2.2.1 The Modeling Methods of A/C-R Systems

Generally, only the dynamics of the four main components and connecting pipes are modeled. The dynamics of other auxiliary components such as the accumulator and receiver are incorporated into the connecting pipes or two heat exchangers. In the literature, the modeling of compressor and expansion valve, regardless of their types (electric, thermostatic or automatic expansion valve), is demonstrated by algebraic empirical equations [31]. This is because the dynamics of a compressor and expansion valve is an order of magnitude faster than those of heat exchangers (evaporator and condenser) [32].

Several types of models have been built for heat exchangers according to different purposes. For instance, discretized or finite difference models are more accurate and usually utilized in many commercial software packages. These types of models can result in high accuracy in prediction [33]; however, they are too complicated to be used in real-time control strategy development and implementation. Another type of heat exchanger model is based on lumped parameters and is usually a first order time-invariant dynamic model; however, it has oversimplified most of the dynamic characteristics of heat exchangers [34]. Above all, the most popular modeling approach is the moving-boundary/interface lumped-parameter method, which is capable of capturing the dynamics of multiple fluid phase heat exchangers while keeping the simplicity of lumped parameter models [34]. Wedekind *et al.* [35] contributed significantly by simplifying a class of two-phase transient flow problems into a type of lumped-parameter systems. With experimental confirmation, the authors showed that the mean void fraction, *i.e.*, the volumetric ratio of vapor to the total fluid of the two-

phase region in a heat exchanger remains relatively unchanged. This suggests that it will stay invariant, regardless of how the refrigerant distributes throughout the heat exchanger and how the length of two-phase region changes [31]. With this assumption, this method allows the two-phase section to be modeled with lumped parameters. In this way, the model can be much more simplified than the discretized model. Based on the first law of thermodynamics, the dynamics of the length of the two-phase section (the movement of the interface between different regions) can be determined.

X. He. used the moving interface and lumped parameter modeling method in [32]. Based on several assumptions such as assuming the heat exchanger is a long, thin, and horizontal tube, the author developed the complete evaporator and condenser nonlinear dynamic model with more than five states for each of them and then derived the entire system model by considering the boundary conditions of all the components. However, in his research, only the linearized model was partially verified. Recently, A. Alleyne and his teammates have improved the model derived by X. He. For instance, B. Li in [36] built a model for startup and shutdown periods by considering different distributions of the refrigerant inside the heat exchangers. The auxiliary components such as the accumulator and receiver were modeled in [34]. Parameter identification algorithms for A/C-R system modeling have also been improved in [37]. Furthermore, some special architecture of vapor compression cycle system that was modeled in [38] and further validated the models experimentally [39-41], and it showed overall improvements over the previous models. More importantly, literature [42] considered the fins' effects by introducing several other parameters such as "fraction of the refrigerant-to-structure surface area on fins and refrigerant-side fin efficiency", which makes the model more complex with 9 states in evaporator alone. In all the models above, there are more than ten states representing the complexity of the model which makes it difficult to guarantee the real-time running of controllers developed based on these models. That is why X. He [43] developed a simple model of the whole system by assuming the identical temperature of heat exchanger wall and reduced the number of states to five. Unfortunately, the simplified model has not been validated experimentally.

The drawbacks of the models existing in literature are elaborated as follows. Firstly, the complete models with more than ten states are too complex to be adopted for developing controllers. Secondly, the simple model does not include fins' effects when modeling heat exchangers, which brings discrepancies to the model. As a result, this study is intended to further improve the accuracy of the model in [42] by incorporating the fins in the model of heat exchangers in a new way without adding

the complexity of the model. Thus, a simplified control-oriented dynamic model of the A/C-R system is developed, where only six states are used instead of more than ten reported in the literature. In order to keep the accuracy of this simplified model comparable to high order models, the fins' effects are considered and lumped into two equivalent parameters. In addition, the effects of the superheat section of in the condenser are also included into the model by studying the experimental data instead of the model used in [43]. This model is simulated and experimentally validated under several scenarios. The results show that this model is simple and accurate enough to be used in real-time control systems.

2.2.2 The Control Strategies of A/C-R Systems

Currently, many kinds of control strategies have been developed for A/C-R systems. At the beginning, the On/off controller, as the most conventional controller, is implemented and widely used. However, its drawbacks mentioned bellow hinder further development, resulting in other kinds of control strategies to emerge. In addition, recently, as the anti-idling technologies and electric vehicles become more and more popular, the electrification technology of the A/C-R system in the vehicle will separate the compressor from the engine such that the compressor is able to actively change its speed instead of passively following the engine speed. The electrification together with employment of continuous variable components in the A/C-R system makes the development of more efficient controllers possible. These control strategies include the capacity control, intelligent control and advanced control strategies, which have become promising alternatives.

2.2.2.1 Conventional Control Strategies

Besides on/off control, the single input single output (SISO), and multiple SISO control strategies belong to the conventional control strategies. They are often referred to as the capacity control, which usually employs PID control techniques by modulating different component parameters like electric motor speed, the speed of fans, or the flow rate of the refrigerant to meet the desired temperature or other control objectives [32, 44].

On/off Control

Due to its simplicity and relative ease of implementation, the on/off approach is a dominant control strategy used in A/C-R systems. It can keep the temperature within a certain range via switching the whole system on or off. Nevertheless, its limitations include: 1), the inability to regulate the temperature oscillation amplitudes upon changing conditions, such as ambient temperature, and

varying food temperature requirements; 2), an excessive temperature swing may make the food deteriorate or may make people feel uneasy; 3), It is suitable for thermostats because of its slow dynamic, but not for the supply air-fan control; 4), Compressor activations can lead to excessive power consumption, and mechanical components wear over time [27]; 5), Most importantly, efficiency is not considered. That is why Alberto *et al.* [45] and B. Li *et al.* [46] improved the conventional on/off controller by adding adaptive or optimization algorithms to make it more efficient. However, such nature of the on/off controller makes greater enhancement difficult.

Capacity Control

Recently, A/C-R systems have incorporated capacity controllers to enhance energy efficiency and performance. This kind of input & output-based control is easily realized by PID controllers. A relevant example is superheat-expansion valve control. Usually, the superheat is controlled by adjusting the valve opening degree to regulate the refrigerant mass flow. Due to various advantages of implementation and design, these input-output controllers have been traditionally used in A/C-R systems. Thus, multiple SISO control loops, like the superheat-expansion valve loop, have been identified, and PID controllers have been used to a great extent. This leads to cross-coupling problems, and it is hard to find and tune the controller parameters due to the nonlinear and MIMO nature of A/C-R systems. As a result, a complicated decoupling procedure is usually required to achieve better control performance.

2.2.2.2 Intelligent Control Strategies

Artificial intelligent (AI) control approaches such as artificial neural network (ANN) control, fuzzy logic control, and expert system, etc., have been developed to deal with nonlinearities or uncertainties in A/C-R processes. ANN has a strong modeling capability for nonlinearities, while fuzzy logic can deal with uncertainties in a straightforward manner. Besides being used directly as controllers based on their own formulation characteristics, ANN, fuzzy logic, etc., also perform the roles of A/C-R models, computing methods, and approximations of other control algorithms. In some cases, these AI control approaches are combined with the A/C-R system control [44]. However, their drawbacks include overtraining, extrapolation, network optimization, and their lack of optimality, all of which impede their development [47].

2.2.2.3 Advanced Control Strategies

Advanced control strategies utilized in A/C-R systems include decoupling control, optimal control (e.g. MPC), nonlinear robust control (e.g. SMC), adaptive control, and so on. B. Koo *et al*. [48] presented a second-order *SMC* for the SISO refrigeration system, which regulates the refrigerant relative length in the evaporator, actually the superheat, by manipulating the compressor speed. This controller can also effectively alleviate chattering phenomenon but does not directly deal with power consumption. R. Shah, *et al*. [49] presented a multivariable adaptive controller. The idea behind is that this controller is able to identify different linear models for a nonlinear system over the domain of operating conditions, so it can be easily used for the complete vapor compression cycle control. This is a kind of nonlinearity compensation for a general dynamic system. There are also other kinds of nonlinearity compensation controls like robust control and Gain Scheduling control [32, 49]. *L. Larsen* proposed two kinds of optimization control methods [50]: set-point optimizing control and dynamic optimizing control. The objective of the former is to derive a general applicable set-point optimization method for refrigeration systems that can drive the set points towards optimal energy efficiency; whereas, the latter is to analyze the phenomenon of synchronization and derive a method for desynchronizing the operation of the distributed controllers.

In all of these advanced control methods, the MPC is a more successful and promising control algorithm based on studies of model identification, optimized algorithm, control structure analysis, parameter tuning, relevant stability and robustness. Therefore, the MPC is gradually becoming a major control method for A/C-R systems. The main value of the MPC is its ability to control multivariable systems under various constraints, especially slow dynamic plants, in an optimal way. It can simultaneously control more than one objective to achieve multi-objective and multivariable control.

A Takagi-Sugeno fuzzy model was utilized to represent the highly nonlinear HVAC system in temperature predictive control. In order to reduce the computational effort of the non-convex optimization problem, a combination of a branch-and-bound search technique was used [51]. Authors in [52] proposed a hierarchical multiple MPC for the temperature control of the HVAC system based on a Takagi–Sugeno fuzzy model. Literature [53] has applied a neuro-predictive controller for the temperature control of automotive air conditioning systems. However, the conclusions are tenuous without any supporting experimental work. A MPC was designed in [54] for a multi-evaporator vapor compression cooling cycle. A decentralized control structure was employed where the global MPC

was to find the set points of the required cooling as well as evaporator pressures and local PI controllers were used for set-point tracking. By properly controlling evaporator pressures and superheat, energy efficiency can be improved. A neuro-fuzzy network based offline optimization was utilized [55] to approximate the input-output relationship of a robust MPC, and validated it on an air-handling unit for the temperature control to increase the computational efficiency of a nonlinear robust MPC. Jain & Alleyne incorporated an exergy-based objective function into a nonlinear MPC to improve the coefficient of performance (COP) of a vapor-compressor cycle operation [56]. Due to the nonlinear objective function, the *fmincon* command in MATLAB that was used for the simulation and real-time implementation is not feasible in practice due to its high computational time. An economic MPC in [57] was proposed to reduce costs for building HVAC systems. In each time interval, a min-max optimization technique is used and transferred to a linear programming problem instead of solving the optimization problem directly; this technique minimizes electricity costs and finds the optimal input for the next step. In his thesis [58], Gustavsson adopted a complex nonlinear model of a vapor compressor system derived by [32], linearized it and subsequently designed a MPC to control the evaporator pressure and superheat by manipulating the compressor speed and electronic expansion valve. The purpose of this MPC was to improve the energy efficiency of the overall plant. In order to show its performance in real situations, several scenarios were simulated by using the linearized mode, but this was done without any experimental validation. In addition, the effects of model inaccuracy on the controller were not studied. An MPC was designed for a commercial multi-zone refrigeration system to minimize the total energy consumption. This MPC employed a fast convex quadratic programming solver to solve a sequential convex optimization problem so as to handle the non-convexity of the objective function. In order to limit the size of the optimization problem in each step, a sample time of 15 *mins* was chosen for predictions of the next 24 hours [59]. A low-complexity MPC was developed for building cooling systems with thermal energy storage. In order to improve the computational efficiency, a periodic moving window blocking strategy is utilized [57]. A time-varying periodic robust invariant set discussed in [60] was used as the terminal constraint to guarantee the robustness under the time-varying uncertain cooling demand. The running time for each step was about 20mins, which satisfies the sample time of 1h chosen for the MPC for prediction of the next 24 hours. A learning-based MPC was proposed in [61] to minimize the energy consumption of an air conditioner while it maintains a comfortable temperature at the same time. A statistical method and a mathematical model for the temperature dynamics of a room were used to learn about the time-varying heating load caused by occupants and equipment. Based on the

information learned from the heating load, this MPC will determine the state (on/off) of the air conditioner. Ultimately, it is still a two position controller for the air conditioner, but it is more intelligent. M. Elliott *et al.* improved their study discussed in [54]. A multi-evaporator vapor compression system was still the research target and the global MPC was used to find the required cooling and pressure setpoints for each zone. The local MPCs and PIDs for each evaporator were used to track these set points by manipulating the valve position and evaporator fan speed. Energy efficiency was guaranteed by choosing the proper pressures and superheats instead of directly integrating the system's inputs into the objective functions of the MPC [62]. Literature [63] conducted a comprehensive literature review on the theory and applications of controllers. In particular, they focused on the MPC in the HVAC systems of buildings, and they elaborated upon the factors that influence the performance of the MPC such as controller structure, process type, optimization algorithms, plant model, prediction horizon, control horizon, constraints, and an objective function. An adaptive MPC for a reefer container was proposed in [64]. Model parameters, states as well as the ambient temperature information for the next 24 hours were identified online. This long prediction period required a relatively long time interval of 1 hour to reduce the optimization problem size at each time step so as to guarantee the real-time application. Since the MPC is recalculated once every hour, the cooling provided by the refrigeration system could be incorrect for up to one hour. This MPC is not suitable for reefer containers in delivery trucks with small thermal inertia since such trucks unload their goods regularly resulting in some extra heating load in the container, which can ruin the quality of the goods. Due to the small thermal inertia and subsequent fast thermal dynamics, the 1 hour time interval is too large to be used.

2.2.3 Summary

Studies of the modeling and control strategies applied in A/C-R systems are summarized as follows: firstly, the conventional on/off controller cannot meet the requirements of the high control performance and energy efficiency. However, due to its robustness and ease of application, it still can be improved by adding auto-tuning algorithms or applied together with other control strategies; secondly, because of the highly nonlinear, MIMO and coupling nature of the A/C-R system, more advanced PID control methods are needed to improve control system performance such as speed, accuracy, and stability. This kind of method is usually combined with other intelligent control algorithms. To make full use of PID control advantages in multiple SISO A/C-R system controls and simplify the design and operation procedure of the control strategies, advanced control such as

decoupling can be used. In addition, due to the robustness and the capability to deal with the highly nonlinear plant, the SMC can be applied to the A/C-R system. However, the current studies on SMC for A/C-R system application are only limited in SISO control; last but not the least, in order to solve multi-objective problems in A/C-R systems mentioned above, the advanced control such as the MPC could be a best choice. A more accurate model of the A/C-R system, especially the physical-principle based model should be developed, and the real-time implementation problem should be solved.

2.3 Power Management Control Strategies in Hybrid Electric Vehicles

A leading challenge for designing hybrid vehicles is the coordination of multiple energy sources, converters, and, in the case of an HEV, power flow control for both the mechanical and the electric path. This requires an appropriate control or a PMS [65], which aims to satisfy the driver's demand for drivability while pursue the maximum drivetrain efficiency, fuel economy, and minimum emissions and costs. Nevertheless, some of these objectives, such as emission reduction and efficiency maximization, are contending parameters. Thus, a good control strategy should be developed to satisfy a tradeoff between them. Recently, achieving smooth gear shifting and minimizing excessive driveline vibrations, known as drivability, are included in the powertrain control strategy [65, 66]. The existing power management strategies have been categorized into rule-based and optimization-based according to survey papers [67~73]. A summary of the reported power management strategies is shown in Figure 2.5. It should be noted that these strategies are not mutually exclusive and can be used alone or in combinations [74].

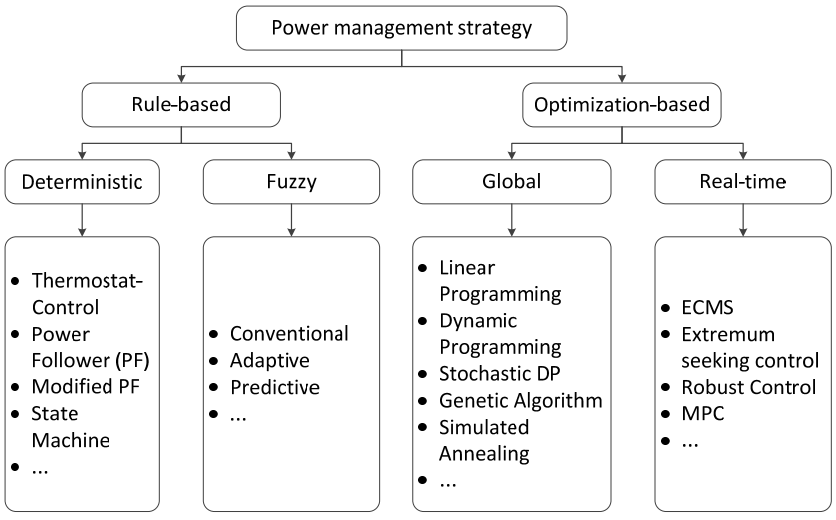

Figure 2.5 Power management strategies currently used in literature

2.3.1 Rule-Based Control Strategies

The rules are designed based on heuristics, intuition, and human expertise without *a prior* knowledge of a predefined cycle. The main feature involved in rule-based strategies is the effectiveness in the real-time supervisory control of power flow in a hybrid powertrain. If the rules are set properly, these strategies can result in a good efficiency in terms of fuel economy and emissions. However, due to the complexity and the non-linearity of the hybrid powertrain, determining accurate rules or thresholds is neither explicit nor straightforward, and experts in most cases fail to define these thresholds and rules with enough accuracy [75]. This is the leading factor that contributes to improving the rule-based strategies.

2.3.1.1 Deterministic Rule-based Methods

The deterministic rule-based controllers operate on a set of rules that have been defined and implemented prior to actual operation, in which some constraints and thresholds are set to try to achieve the optimal solution.

Power follower Control Strategy (PFCS)

In this strategy, the engine is the primary source of power, and the EM is used to assist the engine when needed while sustaining a charge in the batteries. As a popular strategy for power management in a hybrid powertrain, the main disadvantage of this method is that the efficiency of the whole powertrain is not optimized, and improvement in emissions is not directly taken into account. Nevertheless, the control strategies of the Toyota Prius and Honda Insight are developed based on the PFCS [65].

Modified power follower strategy

In order to improve PFCS, an adaptive version was proposed in [76]. The main goal of this approach is to optimize both energy usage and emissions by the introduction of a cost function representing overall fuel consumption and emissions at all candidate-operating points. The control strategy uses a time-averaged speed to find instantaneous energy use and emission targets. The detailed rules for the proposed control strategy are described in [65].

State machine-based strategy

A state machine-based strategy has been utilized in for a parallel HEV [77]. The state machine dictates the operating mode of the vehicle such as ENGINE (engine propelling the vehicle), BOOST

(engine and motor, both propelling the vehicle), CHARGING (engine propelling the vehicle and charging the battery), etc. The transition between operating modes is decided based on a change in driver demand, a change in vehicle operating condition, or a system or subsystem fault. Implementation of a vehicle controller through state machines facilitates fault resilient supervisory control of the whole system. Nevertheless, optimal performance of the vehicle such as fuel economy is not guaranteed. Therefore, this approach brings no extra value to conventional deterministic rule-based methods. Consequently, it seems that switching to fuzzy rule-based methods is a wise decision, as explained in the next section [65].

2.3.1.2 Fuzzy Rule-based Methods

Due to decision-making, robustness, and adaption properties, fuzzy logic control also referred to as intelligent PMS, is a promising candidate to implement into a multi-domain, nonlinear, and time-varying hybrid powertrain system. In fact, instead of using deterministic rules, which require accurately determining constraints and thresholds, the fuzzy logic can make a decision by itself to some extent. As a result, the fuzzy logic controller is an extension of the conventional rule-based controller. Because of the development of artificial intelligence, the intelligent power management strategies have also been experiencing improvement [78-82].

2.3.2 Optimization-Based Control Strategies

The optimization-based control strategy is the other main category. On one hand, a global optimum solution can be obtained by performing the optimization algorithm over a known driving cycle. In fact, the global optimal solution is non-casual in that it finds the minimum fuel consumption using knowledge of future and past power demands. Obviously, this approach cannot be used directly for real-time power management; however, it might be a benchmark of designing rules for online implementations or comparisons for evaluating the quality of other control strategies.

On the other hand, by definition of an instantaneous cost function, a real-time optimization-based control strategy can be found. Such a function has to depend only on the system variables at the current time. The instantaneous cost function should include an equivalent fuel consumption to guarantee the self-sustainability of the electrical path. Thus, the solution of such a problem is not globally optimal, but can be used for real-time implementation. Recently, achieving smooth gear shifting and minimizing excessive driveline vibrations, known as drivability, are included into real-time minimization-based control strategies [65, 83].

Dynamic Programming

Dynamic programming (DP) is a numerical technique that can be applied to any problem that requires decisions to be made in stages with the objective of finding a minimal penalty decision pathway [84]. Thus, if the drive cycle is given, the DP can be applicable to power management and find the global optimum solution. However, the conventional DP takes a significant amount time to perform and requires the drive information as *a priori*, so it cannot be used as the real-time control strategy. It can be used as a benchmark to evaluate other kinds of control strategies. Moreover, because stochastic DP has the ability to optimize a power split map for a probabilistic distribution of drive cycles, rather than a single cycle, Stochastic DP is another way to implement in a real-time controller [85].

Genetic Algorithm

Genetic algorithm (GA) is a probabilistic global search and optimization method that is analogous to natural biological evolution. GA performs on a population of individuals (potential solutions), each of which is an encoding string (chromosome), containing the decision variables (genes) by three operators: selection, crossover, and mutation [86-88]. GA is pretty suitable for complex nonlinear optimization problems since it represents an intelligent exploitation of a random search in the solution space rather than a conventional gradient-based procedure. Due to computational costs and offline optimization, it does not provide the necessary view to the designer of the powertrain like an analytical approach, but can be used to size the powertrain components [65].

Simulated Annealing Algorithm

Simulated annealing (SA) is a random-search technique which adopts an analogy between the way in which a metal cools and freezes into a minimum energy crystalline structure (the annealing process) and the search for a minimum in a more general system. It can deal with highly nonlinear problems effectively [89, 90]. It has the same functionality and application as the GA algorithm. The main drawback of the aforementioned global optimization approaches is too time-consuming to be applied in real time.

Equivalent consumption minimization strategy (ECMS)

The introduction of ECMS provides a way for the utilization of optimal control theory for real-time power management in hybrid vehicles. As an optimization-based method, it determines the optimal power split at each time instant rather than over a time horizon [91, 92]. Thus, no future driving

information needs to be known as *a priori*. An appropriate equivalence factor can help ECMS achieve near-optimal fuel economy [93]. However, tuning the equivalence factor is non-trivial, and there is no guarantee that ECMS is able to produce a globally optimal performance. ECMS can adjust the equivalence factor in order to achieve better fuel economy via adaptive ECMS if the future driving information can be identified beforehand [94, 95].

Model predictive control

In recent years, different MPCs (conventional, adaptive and robust) have been widely utilized in automotive industry [96~101] because of their ability to deal with multivariable constrained problems and their potential for real-time application as a receding horizon control strategy.

Literature [102] assessed two finite-horizon stochastic dynamic programming (DP) algorithms with different levels of access to the drive route from a GPS combined with a traffic flow information system. The discrete time Markov chain technique was employed to model vehicle's states in each of strategy. The results were compared with those of a prescient MPC with a complete known drive route to demonstrate that a predictive controller is possible to be designed by using information received from the vehicle navigation system and traffic-flow-information. A stochastic MPC was designed in [103] for a series HEV, where the future power demand from the driver was modeled as a Markov chain. Its performance was compared with that of a prescient MPC with fully known power demand and a frozen-time MPC using a constant power demand in the prediction horizon. The authors showed that the proposed MPC provided a fuel economy similar to the prescient MPC. In order to alleviate the computational efforts of the MPC algorithm, a fast MPC was designed in [104] by using a new fast Karush-Kuhn-Tucker solving approach based on a totally known drive cycle. The authors in [105] integrated the engine transient characteristics into the MPC-based PMS for enhancing the overall fuel economy, as the engines experience frequent transient operations in HEV applications. The MPC strategy was then evaluated with the assumption that the drive cycle was known to show a superior equivalent fuel efficiency could be achieved. In [106, 107] DP with a neural network (NN) based machine learning was used for predicting driving environments. The simulation by Powertrain Systems Analysis Toolkit (PSAT) showed that the trained NN is effective in predicting roadway type and traffic congestion levels, predicting driving trends. This machine learning algorithm can be combined with MPC for real-time applications. An MPC-based PMS was presented in [108], where both nonlinear MPC and linear time variant MPC were designed and tested over several standard drive cycles. The simulation results were compared with those from an

available controller in PSAT to show a noticeable improvement in fuel economy. In the design process of MPCs, the drive demand torque was assumed to be exponentially decreasing over the prediction horizon. Literature [109] developed an MPC which does not require the time-ordered prediction of the driving condition but a prediction of their distribution under a constant costate assumption. A drive cycle prediction algorithm was designed for the optimization–based PMS development in [110]. Using the data received from an onboard GPS, CAN bus, and inertial measurement unit (IMU) under numerous repeated vehicle operations, the features of each velocity profile were extracted and stored in a database. In a real-time application, the database was searched for the prediction of the velocity profile based on the current vehicle location. The results showed that the proposed PMS with the prediction algorithm can obtain an extra 5% fuel saving, which is pretty close to that of the prescient MPC.

In [111], a modified k-nearest neighbor regressor was utilized to generate weighted samples of the upcoming drive cycle by feature matching the current state to historical states and sequentially an MPC was developed based on the obtained information. The driver behavior was modeled as a Markov chain based on the several standard cycles [112]. Then a shortest path stochastic DP was designed and implemented in a test vehicle to evaluate the performance. The results presented that the fuel economy was improved with less engine on/off events. As an improvement in the process of real-time implementation, a stochastic MPC was proposed in [113]. This stochastic MPC can handle larger state dimension than stochastic DP. A Markov chain that represents the power requested was learned to enhance the prediction capabilities of MPC. Due to the ability to learn the pattern of the driver behavior, the method shows a similar performance as the prescient MPC. A drive cycle estimation algorithm was presented in [114] based on the NN technique for service vehicles driving along the same route. An MPC was designed for a parallel HEV with a hybrid ESS, consisting of a supercapacitor and a battery [115]. The proposed MPC together with a DP and a rule-based strategy were evaluated under typical drive cycles. Dynamic traffic feedback data were used in the development of MPC for a power-split HEV [116]. By using real-time traffic data, the battery state of charge (SoC) trajectory was generated and employed as the final-state constraint. The results showed that a better fuel economy could be achieved by using the traffic flow data. A stochastic MPC was proposed for a parallel HEV particularly running in a hilly region with light traffic in [117]. This PMS considered the road grade and maintains the SoC inside its boundary to avoid degrading the energy efficiency. A finite-horizon Markov decision process was modeled in MPC, which was compared with an ECMS and DP to demonstrate its fuel economy. In [118], a driving-behavior-aware

stochastic MPC was developed for plug-in hybrid electric buses, where the K-means was used to classify driving behaviors, and the Markov chains were utilized to model the driver behavior. A reinforcement learning-based adaptive power management was presented for a hybrid electric tracked the vehicle in [119]. Different approaches for predicting the vehicle velocity were discussed in [120], such as the exponentially varying, stochastic, and the NN-based approach. The sensitivity to tuning parameters was also analyzed. In addition, the prediction precision, computational cost, and the resultant vehicle fuel economy were compared.

Based on available future drive information, the existing MPCs in the current literature can be classified into the types as shown in Figure 2.6. The frozen-time MPC adopts the constant vehicle velocity or torque in the prediction horizon and it is used as a worst baseline to compare with. The exponential varying based MPC uses a simple exponential varying expression to represent the future information. The inaccurate prediction impedes its application. The stochastic MPC employs the Markov chain technique to model the driver's future behavior. The prediction accuracy depends on the tuning parameters. The NN, fuzzy logic, and machine learning methods are adopted in the AI based MPC, which requires lots of training to guarantee its prediction accuracy. Like the frozen-time MPC, the prescient MPC in current literature acts as a benchmark to evaluate the developed. However, as the development of intelligent transportation systems (ITSs) and related telematics techniques, the future vehicle trajectory can be measured or planned somehow in advance and utilized in real-time PMSs [121].

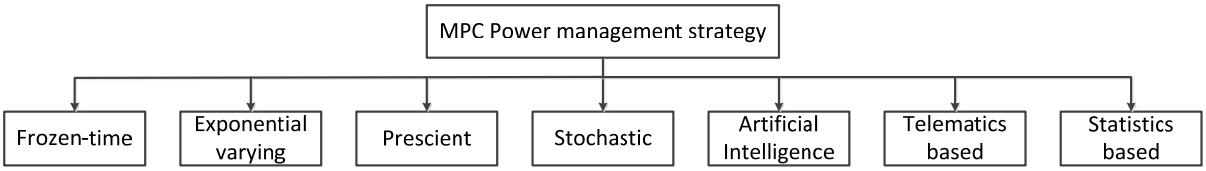

Figure 2.6 MPC-based PMS types

2.3.3 Summary

Owing to the complexity of hybrid powertrains, the PMS plays a crucial role in the performance of the hybrid vehicle [65]. From the above analysis, many power management strategies are introduced and used in theoretical research or in practice according to their advantages/disadvantages. The rule-based strategies are capable of real-time applications but are not optimal; whereas, optimization-based ones are able to produce suboptimal or even optimal solutions but usually suffer from real-time implementations. This is because optimization algorithms are computationally expensive and require

partial or entire future information, such as the vehicle speed. This problem can be alleviated to some extent by using real-time optimization methods or the recent advances in ITSs, onboard global positioning systems (GPSs), geographical information systems (GISs), and advanced traffic flow modeling techniques [122].

Chapter 3
Modeling of the A/C-R System and RAPS

In this chapter, the configuration and model of RAPS are presented followed by the model of the A/C-R system. The models are essential to developing advanced controllers to reduce the power consumption of such systems. Generally, the RAPS is composed of an ESS, a transmission (according to the power that auxiliary devices need), a generator, and inverters as shown in Figure 1.1 RAPS should be compact, modular, and easy-to-install to reduce the installation time and costs without modifying the original powertrain too much.

3.1 Potential Configurations of RAPS

Many prerequisites should be considered before the configuration of RAPS is determined because RAPS as an additional system is integrated into the original conventional vehicle. These prerequisites include the position of the engine in the chassis, drive and transmission types, auxiliary power demand, PTO method and so on. In this study, vehicles with pre-positioned engine and rear-wheel-drive powertrain are studied for the configurations of RAPS.

3.1.1 Power Takeoff via Serpentine Belt

As known, the serpentine belt is a single, continuous belt utilized to drive multiple peripheral devices in an engine, such as an alternator, power steering pump, water pump, air conditioning compressor, air pump, etc. the alternator can be properly controlled to charge the ESS when the SoC is too low. Meanwhile, it can also recover a part of kinetic energy of the vehicle and engine when braking. The configuration schematic is shown in Figure 3.1 (a). Because of the power limit of the alternator and serpentine belts, this configuration can be employed in light service vehicles, such as small food delivery vans used mostly in city cores. The power demands of auxiliary devices in such vehicles are relatively low.

3.1.2 Power Takeoff from PTOs

Figure 3.1 (b) displays another configuration that a PTO is utilized to take power from the engine or recapture kinetic energy when the vehicle brakes. The PTO can be placed along with the gearbox or even the middle of the shaft [123]. The RAPS with this configuration is able to take much power to meet the large auxiliary power demands of the heavy service vehicle.

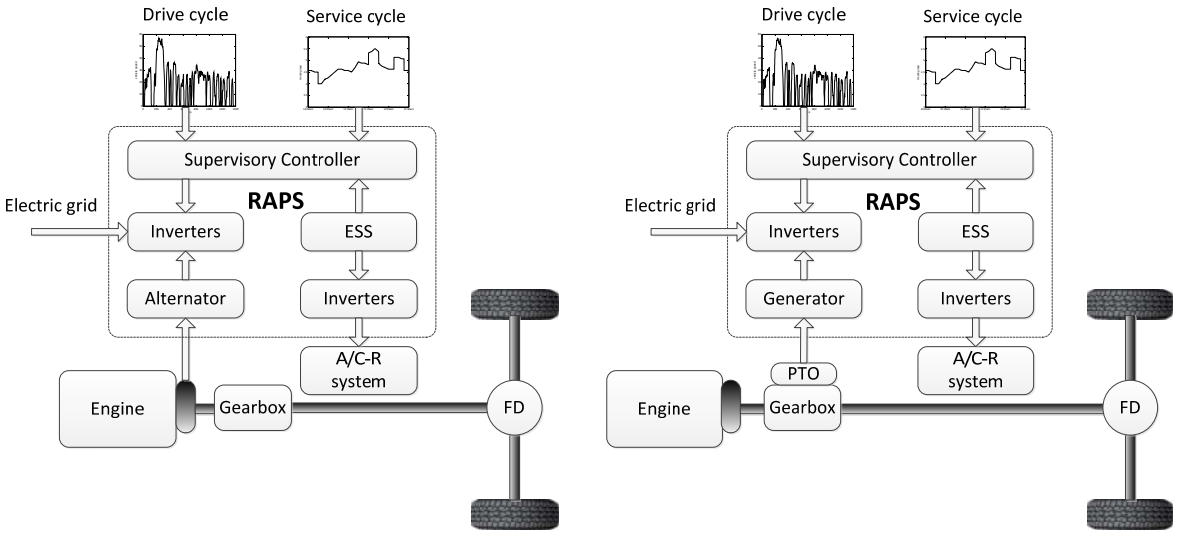

(a) **(b)**

Figure 3.1 RAPS configuration for light (a) and heavy (b) service vehicles

3.2 Modeling of the Powertrain System

For vehicle mass identification and power management controller development, the model based on the backward modeling approach of the longitudinal vehicle dynamics is adequate. As shown in Figure 3.2, the main components are modeled in this section.

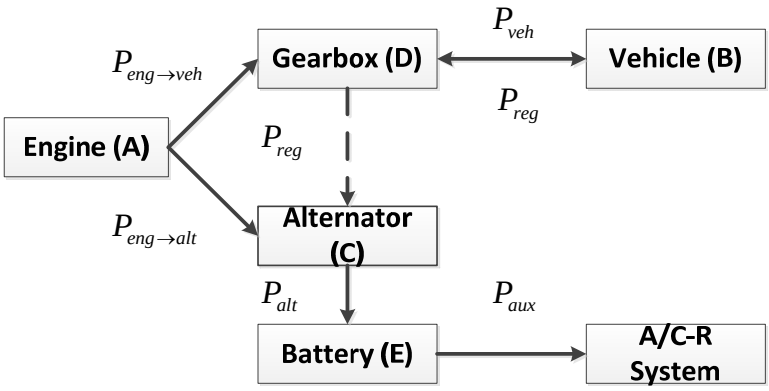

Figure 3.2 Schematic of the RAPS with light service vehicle

3.2.1 Longitudinal Dynamics of Vehicle

The vehicle power should meet the acceleration/deceleration while overcoming the gravity force, resistance forces and aerodynamic forces:

$$P_{veh} = \left(Ma + F_a + F_g + F_r \right) V_{veh} \tag{3.1}$$

where, M is the vehicle total mass (*i.e.* curb mass plus cargo mass), V_{veh} refers to the vehicle speed; a indicates the vehicle acceleration; F_a denotes aerodynamics resistance; F_g means grade resistance; F_r represents the tire rolling resistance. By substituting the corresponding expression of each term, can be rewritten as:

$$P_{veh} = \left(Ma + \frac{1}{2}\rho C_D A_f V_{veh}^2 + Mg\sin\alpha + C_r Mg\cos\alpha \right) V_{veh} \tag{3.2}$$

where, ρ is the mass density of the air, C_D is the coefficient of aerodynamic resistance, A_f is the frontal area of the vehicle, g is the gravitational acceleration, α is the road grade angle, and C_r is the coefficient of rolling resistance.

3.2.2 Engine

The Willan's line modeling approach [124] is utilized for engine modeling thanks to its scalability features. In Figure 3.2, the engine power is split into two portions. One portion is used to move the vehicle and the other to the alternator as follows:

$$P_{eng} = P_{eng\to veh} + P_{eng\to alt} = \omega_{eng} T_{eng} \tag{3.3}$$

where, $P_{eng\to veh}$ and $P_{eng\to alt}$ are powers going to the vehicle and alternator, respectively; ω_{eng} and T_{eng} are the engine's angular velocity and torque, which should not be smaller than the values when the engine is idling as long as the engine is on. The power going to the vehicle can be determined backwardly by

$$P_{eng\to veh} = P_{veh}\left(\frac{1 + sign\left(P_{veh}\right)}{2} \right) \left(\eta_{tran}\right)^{-sign\left(P_{veh}\right)} \tag{3.4}$$

In this equation, η_{tran} refers to the powertrain efficiency. Willan's line method calculates the engine efficiency based on the mean effective pressure (p_{ME}), which describes the engine's ability to produce mechanical work, and fuel available mean effective pressure (p_{MF}), which is the maximum mean effective pressure produced by an engine with 100% efficiency utilizing a unit fuel. In the steady-state running condition of the engine:

$$p_{ME} = \frac{N\pi}{V_{ED}} T_{eng} \tag{3.5}$$

where, N is the number of engine strokes; V_{ED} represents the displacement. Applying the concepts of thermodynamic efficiency and internal losses (p_{ME}) is estimated by,

$$p_{ME} = e_{eng}\, p_{MF} - p_L \tag{3.6}$$

$$p_L = p_{LG} + p_{LF} \tag{3.7}$$

where, p_{MF} is the thermodynamic properties of the engine related to the mean effective pressure, and p_L is the engine losses due to gas exchange (p_{LG}) and friction (p_{LF}). p_{LF} is estimated by

$$p_{LF} = k_1\left(k_2 + k_3\left(S\omega_{eng}\right)^2\right)PI\sqrt{k_4/B} \tag{3.8}$$

In this equation, B is the cylinder bore; PI is the maximum boost pressure and k parameters can be identified by the test data. The efficiency η_{eng} and fuel mass flow $\dot{m}_F$ is defined as:

$$\eta_{eng} = p_{ME} / p_{MF} \tag{3.9}$$

$$\dot{m}_F = P_{eng} / \left(H_L \eta_{eng}\right) \tag{3.10}$$

where, H_L represents fuel's lower heating value.

3.2.3 Alternator

The output electrical power P_{alt} is calculated as,

$$P_{alt} = P_{reg} + P_{eng\to alt} \tag{3.11}$$

$$P_{reg} = \eta_{alt}\eta_{reg}P_{veh}\left(\frac{1-sign\left(P_{veh}\right)}{2}\right)\left(\eta_{tran}\right)^{-sign\left(P_{veh}\right)} \tag{3.12}$$

where, P_{reg} is the regenerative braking power; $P_{eng\to alt}$ indicates the only input of the system; η_{reg} refers to the regenerative braking efficiency; η_{tran} means the efficiency of the and η_{alt} is the efficiency of the alternator, which can be obtained by the experimental data.

3.2.4 Battery

As shown in Figure 3.2, the battery is charged by an alternator and discharged by the A/C-R system. The dynamic of the SoC can be defined by,

$$\frac{dSOC}{dt} = \frac{\Delta P_{batt}}{V_{OC}C_{batt}} \tag{3.13}$$

$$\Delta P_{batt} = P_{alt}\eta_{char} - P_{aux}/\eta_{dis} \tag{3.14}$$

where, V_{OC} shows the open circuit voltage and C_{batt} means the nominal capacity of the battery; η_{char} and η_{dis} are the charging and discharging efficiency of the battery, respectively.

3.3 Modeling of A/C-R Systems

In this section, a new control-based model of A/C-R system is presented, which is different from the existing model. Nowadays, in order to keep passengers comfortable or food fresh, A/C-R systems are widely used in transportation systems and are the main auxiliary loads for service vehicles. In addition, they are widely employed in various places such as supermarkets, buildings, industries, etc.[36]. These systems all work the same way in principle, which utilize a vapor compression cycle to transfer heat. The purpose of the vapor compression cycle process is basically to remove heat from a cold reservoir (*e.g.*, a cold storage room) and transfer it to a hot reservoir - normally the surroundings.

An A/C-R system or a vapor compression cycle generally consists of four main components as shown in Figure 3.3, where the evaporator and condenser are divided into several sections under normal working conditions. There are two sections, i.e., two-phase and superheated sections in the evaporator and three sections, i.e., superheated, two-phase, and subcooling sections in the condenser. The valve is used to uphold the pressures of the two heat exchangers, while the compressor sends the refrigerant from low-pressure heat exchanger to high-pressure heat exchanger. The refrigerant flows through the aforementioned components, alternating its state according to Figure 3.4.

The working principle of the A/C-R system is briefly described below. The refrigerant before entering the evaporator is characterized by low pressure, low temperature and two-phase state. In the evaporator, it will absorb heat from the specific space and change into vapor phase after exiting from the evaporator. The vapor refrigerant is compressed by the compressor and turned into high-pressure and high-temperature vapor. It will then be sent to the condenser where the removal of its heat results in a high-pressure and low-temperature liquid phase. Finally, after going through the expansion valve, the pressure will drop to the evaporator pressure and the liquid refrigerant will be changed into the two-phase state. The same cycle will repeat again.

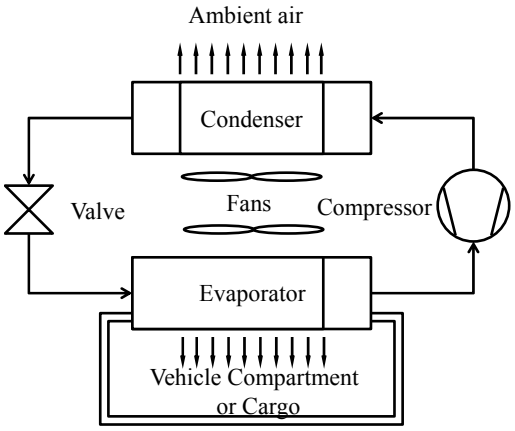

Figure 3.3 Schematic diagram of A/C-R system

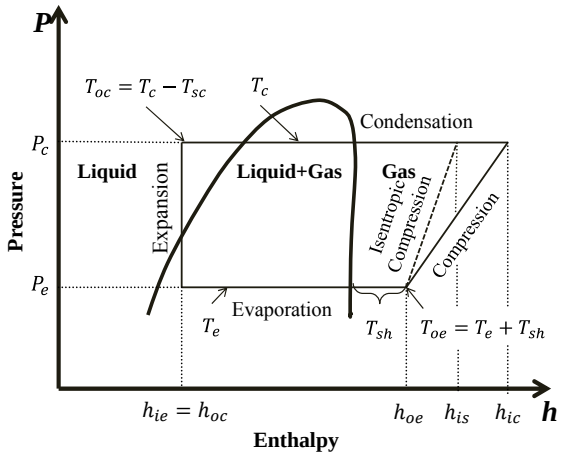

Figure 3.4 Vapor compression cycle in a $h-\log(p)$ diagram [36]

As is well known, the dynamics of the valve and compressor is so fast with respect to the cooling process that they can be treated by some empirical equations obtained from test data. However, for the two heat exchangers, evaporator, and condenser, due to their complex nature, the moving boundary and lumped parameter modeling methods will be employed to develop their control-based dynamic model. In the vapor compression system modeled and experimentally validated in this work, the expansion valve is a thermostatic expansion valve, which adjusts its opening degree according to the refrigerant temperature (superheat temperature) at the outlet of the evaporator. The evaporator is a fin-tube type and the condenser is a microchannel type as shown in Figure 3.5 and Figure 3.6. The refrigerant used is R134a [125]. This section only elaborates the main dynamic equations. For the complete version nonlinear and linearized model for MPC development, please refer to Appendix A.

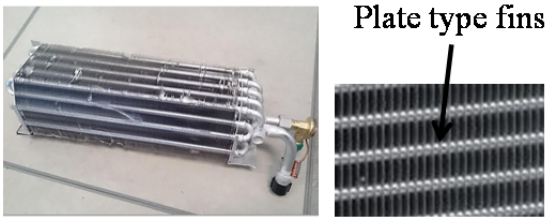

Figure 3.5 Fin-tube evaporator with plate fins

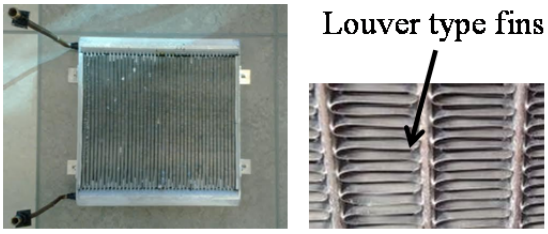

Figure 3.6 Microchannel condenser with louver fins

3.3.1 Evaporator

Before presenting the model, the modeling assumptions [32] will be provided:

1. The heat exchangers are regarded as long, thin, horizontal tubes.

2. The refrigerant is assumed as a one-dimensional fluid flow passing through the heat exchanger.
3. The axial conduction of refrigerant is neglected.
4. The pressure along the whole heat exchanger tube can be assumed to be constant. Thus, the equation for momentum conservation is negligible.

By applying the above assumptions, the partial differential equations for the refrigerant mass and energy [49] can be simplified to one-dimensional PDEs shown as:

$$\frac{\partial\left(\rho A_{cs}\right)}{\partial t}+\frac{\partial \dot{m}}{\partial z}=0 \tag{3.15}$$

$$\frac{\partial\left(\rho A_{cs} h-A_{cs} P\right)}{\partial t}+\frac{\partial\left(\dot{m} h\right)}{\partial z}=p_i \alpha_i\left(T_w-T_r\right) \tag{3.16}$$

$$\left(C_p \rho A\right)_w \frac{\partial T_w}{\partial t}=p_i \alpha_i\left(T_r-T_w\right)+p_o \alpha_o\left(T_a-T_w\right) \tag{3.17}$$

Equation (3.15) represents the mass conservation of refrigerant going through the heat exchanger, while the following two equations describe the conservation of the energy exchanged between the refrigerant and the tube wall as well as the wall and ambient media. To perform the integrations along the whole heat exchanger tube, Leibniz's equation is utilized:

$$\int_{z_1(t)}^{z_2(t)} \frac{\partial f\left(z,t\right)}{\partial t} dz=\frac{d}{dt}\left[\int_{z_1(t)}^{z_2(t)} f\left(z,t\right) dz\right]-f\left(z_2\left(t\right),t\right)\frac{dz_2\left(t\right)}{dt}+f\left(z_1\left(t\right),t\right)\frac{dz_1\left(t\right)}{dt} \tag{3.18}$$

where, z is the spatial coordinate. The limits of this integration depend on how to divide the whole exchanger wall depending on the current working conditions. As a heat exchanger, the evaporator takes away heat from a cooler area to a warmer area; meanwhile, the refrigerant absorbs the heat and transfers from the two-phase state into the gas state. As Figure 3.3 indicated, the evaporator is simply divided into two zones - two-phase (liquid and gas) section and superheat section - when it is properly working. For other division methods please refer to [36]. Because of the objective of this study is to save energy while attaining a good temperature performance, it is reasonable to assume that only the properly working period is considered.

Since the ability to absorb heat for liquid is much better than that of gas, the evaporator should accumulate as much two-phase refrigerant as possible to enhance the heat transfer efficiency; however, the liquid should be completely changed into gas before entering the compressor in order to protect the compressor from any damage. As such, the superheat zone was utilized to ensure the refrigerant totally evaporates before exiting the evaporator. From an efficiency perspective, the superheat section should be as small as possible to approach its ideal state (zero).

3.3.1.1 Dynamic Model

As two sections are assumed in the evaporator, by introducing the time independent mean void fraction $(\bar{\gamma})$, two zones can be lumped into two nodes as indicated in Figure 3.7. Mass and energy conservation equations for each node can be derived by Equation (3.15) to Equation (3.18) [32, 34],

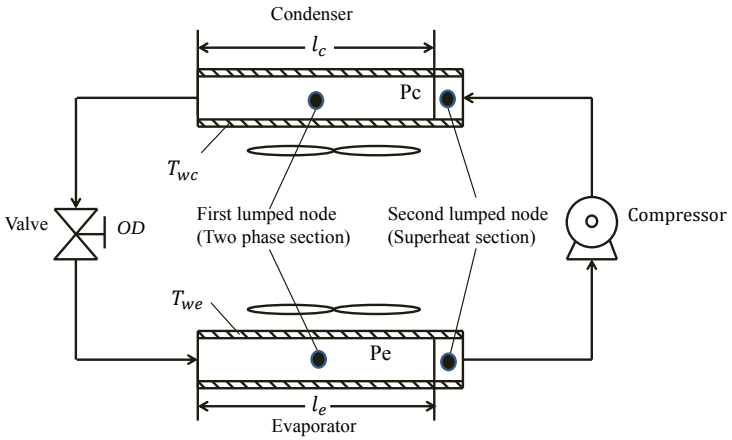

Figure 3.7 Two-zone mode of evaporator and condenser

For the first node (two-phase zone), the mass and energy equations of refrigerant are as follows:

$$\left(\frac{d\rho_l}{dP_e}(1-\bar{\gamma})+\frac{d\rho_g}{dP_e}\bar{\gamma}\right)A_{cs}l_e\frac{dP_e}{dt}+\left(\rho_l-\rho_g\right)(1-\bar{\gamma})A_{cs}\frac{dl_e}{dt}=\dot{m}_{in}-\dot{m}_{\text{int}} \tag{3.19}$$

$$\left(\frac{d\left(\rho_l h_l\right)}{dP_e}(1-\bar{\gamma})+\frac{d\left(\rho_g h_g\right)}{dP_e}\bar{\gamma}-1\right)A_{cs}l_e\frac{dP_e}{dt}+\left(\rho_l h_l-\rho_g h_g\right)\left((1-\bar{\gamma})A_{cs}\frac{dl_e}{dt}\right)=$$
$$\dot{m}_{in}h_{in}-\dot{m}_{\text{int}}h_{\text{int}}+\alpha_{i1}A_i\left(\frac{l_e}{L_e}\right)\left(T_{w1}-T_{r1}\right) \tag{3.20}$$

Regarding the second node (superheat zone), the mass and energy conservation equation are presented in the following two equations:

$$\left[\left(\left.\frac{\partial\rho_2}{\partial P_e}\right|_{h_2}\right)+\frac{1}{2}\left(\left.\frac{\partial\rho_2}{\partial h_2}\right|_{P_e}\right)\left(\frac{dh_g}{dP_e}\right)\right]A_{cs}L_2\frac{dP_e}{dt}+\frac{1}{2}\left(\left.\frac{\partial\rho_2}{\partial h_2}\right|_{P_e}\right)A_{cs}L_2\frac{d\dot{h}_{out}}{dt}+\left(\rho_g-\rho_2\right)A_{cs}\frac{dl_e}{dt}$$
$$=\dot{m}_{\text{int}}-\dot{m}_{out} \tag{3.21}$$

$$\left[\left(\left(\left.\frac{\partial\rho_2}{\partial P_e}\right|_{h_2}\right)+\frac{1}{2}\left(\left.\frac{\partial\rho_2}{\partial h_2}\right|_{P_e}\right)\left(\frac{dh_g}{dP_e}\right)\right)h_2+\frac{1}{2}\left(\frac{dh_2}{dP_e}\right)\rho_2-1\right]A_{cs}L_2\frac{dP_e}{dt}+\frac{1}{2}\left[\left(\left.\frac{\partial\rho_2}{\partial h_2}\right|_{P_e}\right)h_2+\rho_2\right]A_{cs}L$$
$$+\left(\rho_g h_g-\rho_2 h_2\right)A_{cs}\frac{dl_e}{dt}=\dot{m}_{\text{int}}h_{\text{int}}-\dot{m}_{out}h_{out}+\alpha_{i2}A_i\frac{L_2}{L_e}\left(T_{w2}-T_{r2}\right) \tag{3.22}$$

For the heat exchanger tube wall in each node, there should be an energy conservation equation between the heat absorbed from the ambient air and rejected to the refrigerant. The energy conservation processes for both nodes can be represented by,

$$\left(C_p\rho V\right)_w\frac{dT_{w1}}{dt}=\alpha_{i1}A_i\left(T_{r1}-T_{w1}\right)+\alpha_o A_o\left(T_{w1}-T_{r1}\right) \tag{3.23}$$

$$\left(C_p\rho V\right)_w\left[\frac{dT_{w2}}{dt}-\left(\frac{T_{w2}-T_{w1}}{L_2}\right)\frac{dL_1}{dt}\right]=\alpha_{i2}A_i\left(T_{r2}-T_{w2}\right)+\alpha_o A_o\left(T_a-T_{w2}\right) \tag{3.24}$$

The above six equations constitute the two-zone mode evaporator model with the input vector u and state vector x defined by:

$$u=\left[\dot{m}_{\text{int}}\quad \dot{m}_{out}\quad h_{in}\quad T_{ain}\quad \dot{m}_a\right]^T \tag{3.25}$$

$$x=\left[l_e\quad P_e\quad h_{out}\quad T_{w1}\quad T_{w2}\right]^T \tag{3.26}$$

Some important outputs with several important parameters are shown in the following equations:

$$y=\left[l_e\quad P_e\quad h_{out}\quad T_{w1}\quad T_{w2}\quad T_{ao}\quad T_{ro}\quad T_{sh}\quad m_e\right]^T \tag{3.27}$$

$$T_a=T_{ai}\mu+T_{ao}\left(1-\mu\right) \tag{3.28}$$

$$\rho_1=\rho_g\overline{\gamma}+\rho_l\left(1-\overline{\gamma}\right) \tag{3.29}$$

$$\dot{m}_{air}C_{p\_air}\left(T_{ai}-T_{ao}\right)=\alpha_o A_o\sum_1^n\frac{L_i}{L_e}\left(T_a-T_{wi}\right) \tag{3.30}$$

$$T_a=\left(\frac{1}{1-\mu}\left(\frac{\dot{m}_{air}C_{p\_air}}{\alpha_o A_o}\right)T_{ai}+\left[\frac{L_1T_{w1}}{L_e}+\frac{L_2T_{w2}}{L_e}\right]\right)\Bigg/\left(\frac{1}{1-\mu}\left(\frac{\dot{m}_{air}C_{p\_air}}{\alpha_o A_o}\right)+1\right) \tag{3.31}$$

After rearranging the above equations, a more compact form shown in Appendix can be obtained:

$$G\left(x,u\right)\dot{x}=f\left(x,u\right) \tag{3.32}$$

$$y=h\left(x,u\right) \tag{3.33}$$

3.3.1.2 Simplified Model

The condenser model can be derived by using the same methods. It can be seen that the complete model of the whole cycle with more than ten states are too complex to be used to develop controllers. All the heat exchanger models in the literature are based on a long, thin, one-dimensional tube assumption. They do not consider the fins' effects or consider them in a complicated way [42] when modeling the heat convection between the tube wall and the refrigerant inside. However, from Figure 3.5 and Figure 3.6, it can be seen that there are many fins (plate type or louver shape type) around the tube walls. Usually, the fins and tubes are made from the same material. If it is not considered, the heat conduction throughout the fins would introduce inaccuracy to the model.

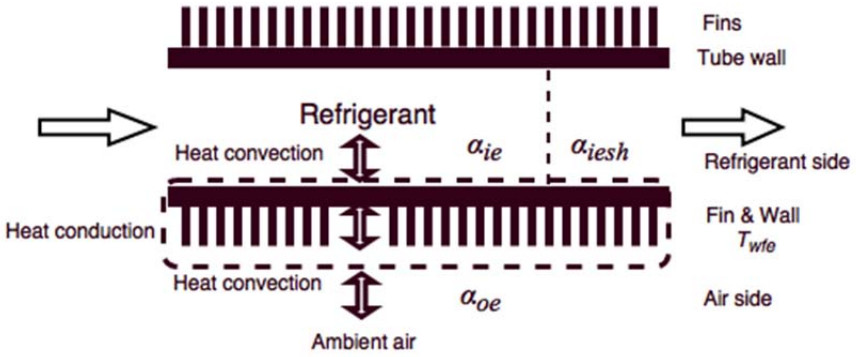

Figure 3.8 Schematic of evaporator with equivalent parameters

Unlike the thin tube wall where no temperature gradient is assumed, the fins are long, and a one-dimensional temperature gradient exists along the length of the fins. This gradient is dependent on the structure of the fins and difficult to simulate. However, from the perspective of energy conservation, the energy transferred from the refrigerant to the tube wall and fins is identical to the energy taken away by the air and the energy kept on the wall and fins due to their thermal inertia. In this way, the wall and fins could be lumped together shown in dotted box of Figure 3.8. Thus, it is reasonable to utilize an equivalent temperature T_{wfe} to represent the temperature of wall and fins. The other equivalent parameter used is the refrigerant-side heat transfer coefficient. In the evaporator, α_{ie} and α_{iesh} are provided to represent the coefficients for the two-phase section and the superheat section respectively. After applying these equivalent parameters and by introducing another assumption that the tube wall temperatures in different sections are the same, the simplified nonlinear dynamic model of the evaporator can be written as [32, 43]:

$$h_{lge}\rho_{le}\left(1-\bar{\gamma}_e\right)A_e\frac{dl_e}{dt}=\dot{m}_v\left(h_{ge}-h_{ie}\right)-\alpha_{ie}\pi D_{ie}l_e\left(T_{wfe}-T_{re}\right) \tag{3.34}$$

$$A_eL_e\frac{d\rho_{ge}}{dP_e}\frac{dP_e}{dt}=\dot{m}_v\frac{h_{ie}-h_{le}}{h_{lge}}-\dot{m}_{comp}+\frac{\alpha_{ie}\pi D_{ie}l_e\left(T_{wfe}-T_{re}\right)}{h_{lge}} \tag{3.35}$$

$$\left(C_pm\right)_{wfe}\frac{dT_{wfe}}{dt}=\alpha_{oe}A_{oe}\left(T_{ae}-T_{wfe}\right)-\alpha_{ie}\pi D_{ie}l_e\left(T_{wfe}-T_{re}\right)-\alpha_{iesh}\pi D_{ie}(L_e-l_e)\left(T_{wfe}-T_{re}\right) \tag{3.36}$$

$$\dot{Q}_{cool}=\dot{m}_{e\_air}C_{air}\left(T_{setpo\,\mathrm{int}}-T_{ae}\right)=\alpha_{oe}A_{oe}\left(T_{ae}-T_{wfe}\right) \tag{3.37}$$

$$\dot{m}_{e\_air}=k_eN_{evap} \tag{3.38}$$

$$\alpha_{oe}=\alpha_{oe0}\left(\dot{m}_{e\_air}/\dot{m}_{e\_air0}\right)^m \tag{3.39}$$

$$T_{ae}=\left(\frac{1}{1-\mu}\frac{\dot{m}_{e\_air}C_{air}}{\alpha_{oe}A_{oe}}T_{setpo\,\mathrm{int}}+T_{wfe}\right)\Bigg/\left(\frac{1}{1-\mu}\frac{\dot{m}_{e\_air}C_{air}}{\alpha_{oe}A_{oe}}+1\right) \tag{3.40}$$

$$\dot{W}_{evap}=k_{evap}N_{evap}{}^3 \tag{3.41}$$

where, the three states refer to the length (l_e) of the two-phase section, the pressure (P_e) of the evaporator, and the equivalent temperature (T_{wfe}) of tube wall & fins. Equation (3.34) simulates the energy transfer from the refrigerant to the heat exchanger tube wall & fins of the two-phase section. The first term on the right-hand side of this equation shows the energy change after the refrigerant goes through the two-phase section; h_{ge} represents the enthalpy of the vapor refrigerant under the current pressure, or the enthalpy at the boundary of the two sections, and h_{ie} denotes the enthalpy of the refrigerant at the inlet of the evaporator. The second term describes the energy absorbed from the evaporator tube wall and fins of the two-phase section where D_{ie} means the inner diameter of the tube and T_{re} indicates the saturation temperature of the refrigerant under the current pressure. Thus, the difference between these two terms represents the energy absorbed/rejected by the two-phase section or the energy needed to evaporate the liquid refrigerant in the two-phase section. Based on this energy change, the two-phase length change can be obtained by using the left-hand side term where h_{lge} means the latent enthalpy; ρ_{le} refers to the liquid refrigerant density; $(1-\bar{\gamma}_e)$ shows the liquid volumetric fraction of the two-phase section, and A_e represents the sectional area of the tube [39]. All the enthalpies $\left(h_{ge},h_{ie},h_{\mathrm{lg}e}\right)$, densities/density variation with respect to pressure $\left(\rho_{le},\rho_{ge},\rho_{ie},d\rho_{ge}/dP\right)$ and temperature (T_{re}) of the refrigerant can be obtained by lookup tables built

according to thermodynamic properties [125] of the used refrigerant; whereas, the heat transfer coefficients are identified by experimental data and shown in Table 4.1.

Equation (3.35) denotes the vapor refrigerant change rate throughout the evaporator tube. The first term on the right-hand side of this equation refers to the vapor mass at the inlet of the evaporator. As is known, the refrigerant will become a two-phase refrigerant after going through the expansion valve liquid. Based on the enthalpy (h_{ie}) of refrigerant, liquid enthalpy (h_{le}), and latent enthalpy $\left(h_{lge}\right)$ the liquid percentage at the inlet of the evaporator can be found. The second term represents the mass flow rate leaving evaporator; whereas, the third term is the vapor refrigerant changed from the liquid. The left-hand side is the vapor mass change rate inside the evaporator. The pressure change rate can be found via the density change rate by using the chain rule. L_e means the total length of the evaporator tube wall, and ρ_{ge} indicates the density of the vapor refrigerant under the current evaporator pressure (P_e).

Equation (3.36) reflects the heat conduction of the whole heat transfer process. The first term on the right-hand side refers to the total energy transferred to the tube wall & fins from the ambient air, and α_{oe} denotes the heat transfer coefficient, which can be found by Colburn J-factor correlation; A_{oe} represents the total outside area of the tube wall as well as fins; T_{ae} means the mean air temperature. The last two terms refer to the energy transferred from the tube wall & fins to the refrigerant in the two-phase section and the superheated section, respectively; whereas, α_{iesh} refers to the heat transfer coefficient in superheat section. The left-hand side shows the change of the temperature of the tube wall & fins because the mass m and C_p are the total mass and specific heat of the tube wall & fins.

Since the equivalent wall and fins temperature are defined based on energy conservation, it is not the temperature of the wall or fins, so it could not be measured directly. After lumping the fins and the wall together, Pierre's correlation [32] for calculating refrigerant-side heat transfer coefficient is no longer suitable. However, these equivalent parameters could be identified easily by Equation (3.35, 3.36). Thus, there are only three states in the evaporator model. The cooling capacity produced by the system can be represented by (3.37). The air mass flow rate generated by the fan is approximately proportional to the fan speed (3.38). The air-side heat transfer coefficient α_{oe} is varying with the air mass flow rate $\dot{m}_{e\_air}$ as shown in (3.39) [34]. Equation (3.40) describes the temperature of the air around the evaporator. The power consumption of the evaporator fan is calculated by (3.41).

3.3.2 Condenser

As is mentioned above, the microchannel type condenser is modeled and used in the experimental work. It can be seen from Figure 3.6 that many louver-shape fins are around each tube. There are many parallel microchannels inside each tube. Under normal working conditions, the refrigerant distribution is more complex than that of the evaporator.

The condenser can be divided into three sections; however, in order to simplify the model for the purpose of the real-time application, the study of the experimental data suggests that the subcooling section could be neglected due to the much lower subcooling temperature (about $2^{\circ}C$) as compared to the superheat temperature (about $50^{\circ}C$). Another reason is that the energy rejected to generate this lower subcooling temperature is also relatively small. Besides that, the small energy error caused can be compensated by the equivalent heat transfer coefficient of the two-phase section. To make up for this subcooling section from a temperature aspect, the refrigerant temperature at the outlet of the condenser could be found by experimental data. Using the above assumptions, the condenser equations can be obtained in a similar manner to those of the evaporator.

It is known that the total mass m_{total} of the refrigerant inside the cycle is constant without considering the leakage. The mass of refrigerant outside of the two heat exchangers is defined as m_{pipe}. Therefore, the difference between these two masses represents the mass inside the evaporator and the condenser, which can be shown by [43],

$$\begin{aligned} m_{total} - m_{pipe} &= A_e\left[\rho_{le} l_e\left(1-\overline{\gamma}_e\right) + \rho_{ge} l_e \overline{\gamma}_e + \rho_{she}\left(L_e - l_e\right)\right] \\ &+ A_c\left[\rho_{lc} l_c\left(1-\overline{\gamma}_c\right) + \rho_{gc} l_c \overline{\gamma}_c + \rho_{shc}\left(L_c - l_c\right)\right] \end{aligned} \tag{3.42}$$

The first term of the right-hand side refers to the refrigerant mass of both vapor and liquid inside the evaporator, the second term to that inside the condenser; whereas, l_c and $\overline{\gamma}_c$ are the length and mean void fraction of the two-phase section of the condenser. Therefore, from Equations (3.34) and (3.42), the two-phase length of the condenser can be found. As a result, there are only two states, pressure $\left(P_c\right)$ and equivalent temperature $\left(T_{wfc}\right)$ with which the condenser equations similar to the evaporator can be written as [43]:

$$A_c L_c \frac{d\rho_{gc}}{dP_c}\frac{dP_c}{dt} = \dot{m}_{comp} - \frac{\alpha_{ic}\pi D_{ic} l_c\left(T_{rc} - T_{wfc}\right)}{h_{lgc}} \tag{3.43}$$

$$\left(C_p m\right)_{wfc}\frac{dT_{wfc}}{dt}=\alpha_{oc}\left(N_{cond}\right)A_{oc}\left(T_{ac}-T_{wfc}\right)-\alpha_{ic}\pi D_{ic}l_c\left(T_{wfc}-T_{rc}\right)$$
$$-\alpha_{icsh}\pi D_{ic}\left(L_c-l_c\right)\left(T_{wfc}-\left(T_{rc}+T_{ic}\right)/2\right) \tag{3.44}$$

$$\dot{Q}_{heat}=\dot{m}_v\left(h_{ie}-h_{oc}\right)=\dot{Q}_{cool}+\dot{W}_{comp}\left(1-f_q\right) \tag{3.45}$$

$$\dot{m}_{c\_air}=k_c N_{cond} \tag{3.46}$$

$$\alpha_{oc}=\alpha_{oc0}\left(\dot{m}_{c\_air}/\dot{m}_{c\_air0}\right)^m \tag{3.47}$$

$$T_{ac}=\left(\frac{1}{1-\mu}\frac{\dot{m}_{c\_air}C_{air}}{\alpha_{oc}A_{oc}}T_{amb}+T_{wfe}\right)\Bigg/\left(\frac{1}{1-\mu}\frac{\dot{m}_{c\_air}C_{air}}{\alpha_{oc}A_{oc}}+1\right) \tag{3.48}$$

$$\dot{W}_{cond}=k_{cond}N_{cond}{}^3 \tag{3.49}$$

3.3.3 Compressor

The mass flow of refrigerant through the compressor $\dot{m}_{comp}$, where the volumetric displacement is V_d, the pump speed N_{comp}, the volumetric efficiency is η_{vol} and also the refrigerant density ρ_{ref}:

$$\dot{m}_{comp}=N_{comp}V_d\eta_{vol}\rho_{ref}\left(P_e\right) \tag{3.50}$$

the enthalpy at the outlet of compressor is represented by h_{oc}; h_{ic} is the enthalpy at the inlet of compressor; $h_{is}\left(P_e,P_c\right)$ refers to the isentropic enthalpy during the compression process, which can be found by thermodynamic property of the refrigerant; η_a is adiabatic efficiency, which can be obtained by polynomial correlations $\eta_a=f_a(N_{comp},P_c-P_e)$ with respect to the speed of compressor and two pressures [37].

$$h_{oc}=\eta_a\left(h_{is}\left(P_e,P_c\right)-h_{ic}\left(P_e\right)\right)+h_{ic}\left(P_e\right) \tag{3.51}$$

The power consumption [50] in the compressor $\dot{W}_{comp}$, assuming a constant heat loss coefficient f_q is:

$$\dot{W}_{comp}=\frac{1}{1-f_q}\dot{m}_{comp}\left(h_{oc}-h_{ic}\right) \tag{3.52}$$

3.3.4 Expansion Valve

The expansion valve is assumed to be isenthalpic *i.e.* the enthalpy at the inlet of the valve is identical to that at the outlet [37]. The other important parameter is the refrigerant mass flow rate $\dot{m}_v$ through the expansion valve that is modeled by

$$\dot{m}_v = C_v A_v \sqrt{\rho_v \left(P_c - P_e \right)} \tag{3.53}$$

where, P_c and P_e are the pressures of condenser and evaporator; ρ_v is the refrigerant density at the inlet of the valve; C_v represents the discharge coefficient mapped as a polynomial correlation $\left(C_v = f_C(P_c - P_e)\right)$ of the pressure difference between evaporator and condenser; A_v refers to the area of the valve opening mapped as a polynomial correlation $\left(A_v = f_A(P_{sat} - P_e)\right)$ of the pressure difference between evaporator and the saturation pressure of the evaporator outlet temperature. These correlations can be obtained by experimental data. The remaining parameters such as density can be obtained by the thermodynamic properties [125] of the refrigerant built in lookup tables.

3.3.5 Other Components

In the vapor compression cycle, the four main components are connected by several pipes of different sizes. Usually, the pipes are assumed to be adiabatic, and the pressure loss is neglected because of the short length. The refrigerant mass inside the pipe is m_{pipe}, and it is estimated by the length and inner diameter of each piece of pipe. Using the pressure inside the pipe, the density is found. The state of refrigerant in each pipe is assumed to be uniform except for the one between the expansion valve and evaporator, where the refrigerant is in a two-phase state. The vapor percentage can be approximated by $\left(h_{ie} - h_{le}\right) / h_{lge}$ as explained in the evaporator model. In this proposal, the refrigerant R134a is used. According to its test data, several lookup tables are created in order to calculate the state values and their derivatives of the refrigerant.

3.3.6 The Cargo Space Model

For any A/C-R system, there is one or more objective space to cool or warm. For example, for the cargo of a refrigerated vehicle, the temperature dynamic model is built based on the heat transfer theory (heat convection and conduction), and the following assumptions are made [36]:

1) The air temperature in the cargo space is uniform;
2) The temperatures for interior and exterior surface of the cargo wall are uniform;

3) One-dimensional heat conduction through the cargo wall is assumed.

The whole heat transfer process can be divided into three parts: the ambient air to the exterior surface of the wall, then to the interior surface, and finally to the air into the cargo space. The heat balance process of the cargo is represented by Figure 3.9:

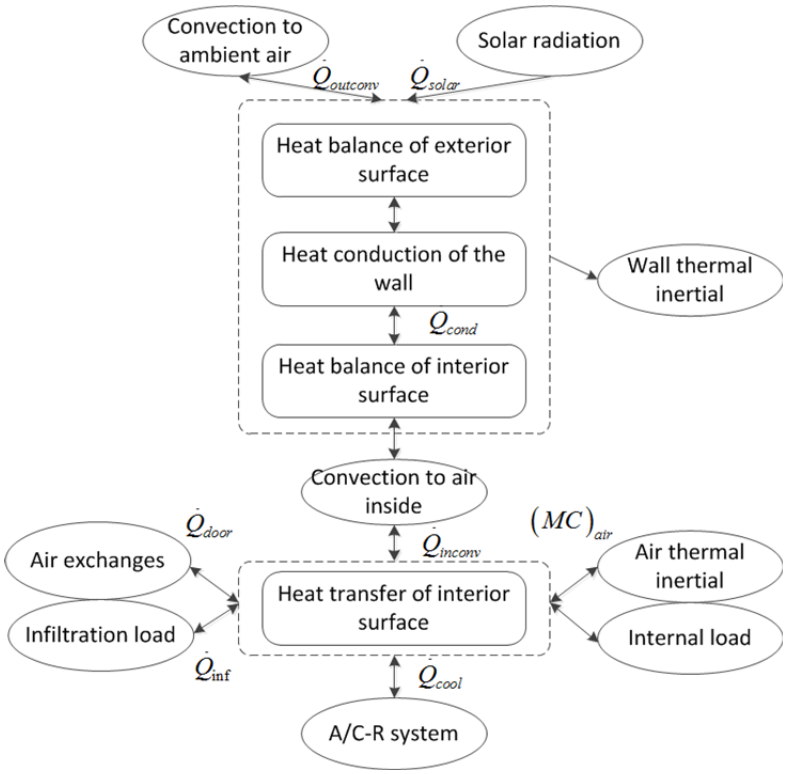

Figure 3.9 Schematic of heat transfer processes in the cargo space model [36]

In this figure, $\dot{Q}_{solar}$ is the solar heating load, $\dot{Q}_{inconv}$ and $\dot{Q}_{outconv}$ represent the convective heat transfer from the interior surface and the exterior surface of the cargo to the inside or outside air; $\dot{Q}_{cond}$ is the conduction heat transfer from the exterior surface to the interior surface of the wall; $\dot{Q}_{door}$ and $\dot{Q}_{\inf}$ are the load due to opening the door and infiltration load, respectively. Three states (exterior surface temperature, interior surface temperature and cargo space temperature) are employed to represent the heat transfer in the whole process. However, for the sake of simplicity, only the last process is considered in this study. For the detailed information, please refer to [41]. The dynamic response of the cargo temperature is simulated by:

$$\frac{dT_{cargo}}{dt} = \frac{\dot{Q}_{inconv} + \dot{Q}_{inf} + \dot{Q}_{door} - \dot{Q}_{vcc}}{(MC)_{air}} \tag{3.54}$$

In the simulation and experimental work, the first two parameters will be treated together and identified by test data as the heating load from outside. As an extra heating load or a disturbance $\dot{Q}_{door}$ will be added by to experiment process by a heater. The thermal inertia, $(MC)_{air}$, of the air inside the whole cargo space.

3.3.7 MATLAB/Simulink Model

Based on the above equations, the Simulink model of the A/C-R system is built. In this model, the accumulator and receiver are not included and the pipe loss is also neglected. In order to simplify the model representation, the "go to" and "from" blocks are used to connect the four main components. It is easy to build the compressor and electric expansion valve according to their equations in the last section.

However, for the modeling of heat exchangers, several steps should be followed in order to get the correct results. Firstly, it is important to calculate or estimate the suitable initial conditions after obtaining the physical parameter values and operating conditions. This is because, as previously mentioned, the initial conditions should be in the model feasible region to ensure the model runs correctly. Then, calculate $f(x,u)$ and $G(x,u)$ based on the initial conditions and lookup table outputs. Finally, integrate the derivatives of the model states and replace the initial conditions with the newly obtained state values [32, 36, 39, and 40]. The whole model structure for a heat exchanger is depicted in Figure 3.10,

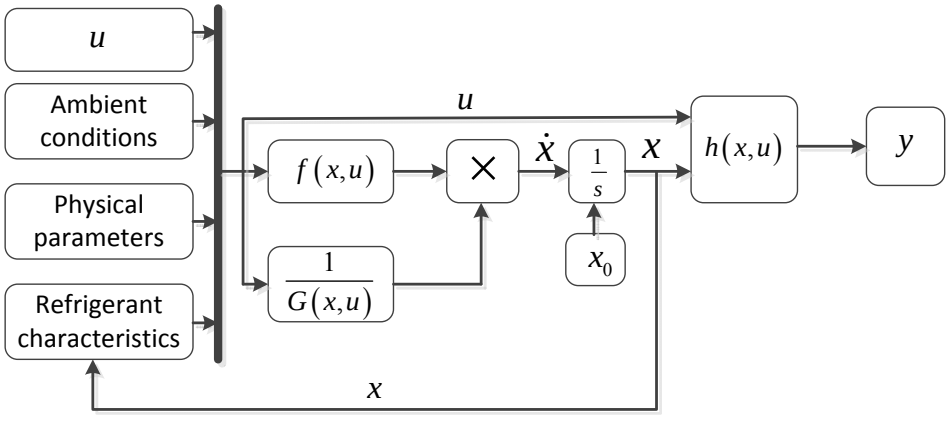

Figure 3.10 Heat exchanger model structure diagram

The schematic of Simulink model of the A/C-R system is depicted in Figure 3.11,

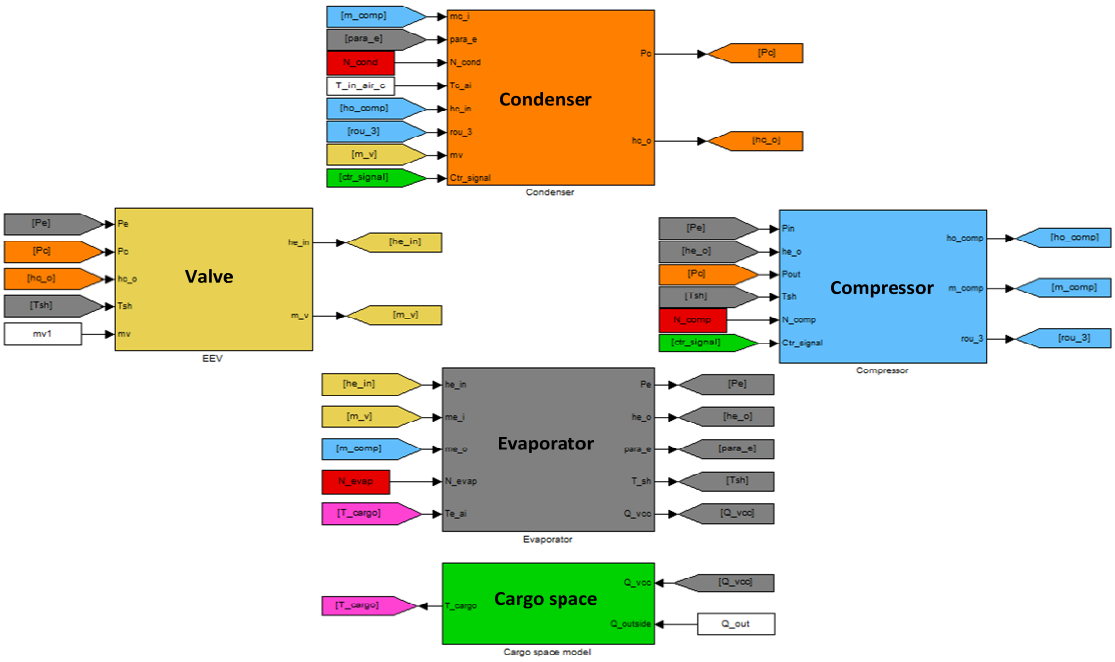

Figure 3.11 Simulink model of A/C-R system with the cargo space

3.4 Summary

In this chapter, the model of the RAPS was developed and a new and simplified version of A/C-R system model was also proposed for the controller studies that will be discussed in Chapter 5. The models were implemented in MATLAB environment for simulations. In the following Chapters the models were evaluated and verified by experimental studies.

Chapter 4
Experimental Studies and Model Validation

In this chapter, the experimental system of an automotive A/C-R system is introduced, based on which, the model is validated comprehensively. In addition, the setup used to simulate the RAPS is briefly introduced, which will be utilized for testing the performance of the developed power management controllers in the future study.

4.1 Experimental A/C-R System

In order to validate the model and verify the performance of controllers, an automotive A/C-R system at Simon Fraser University is used. From the schematic of the experimental system in Figure 4.1, it can be seen that two independent environmental chambers are connected with the evaporator and condenser units by pipes. The evaporator-side chamber acts as the cargo and its temperature will be a controlled parameter while the temperature at the inlet of the condenser can be controlled and used as operating conditions when the experiments are conducted.

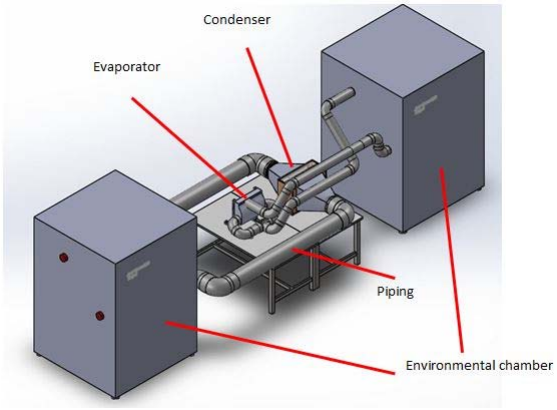

Figure 4.1 Schematic of the A/C-R system

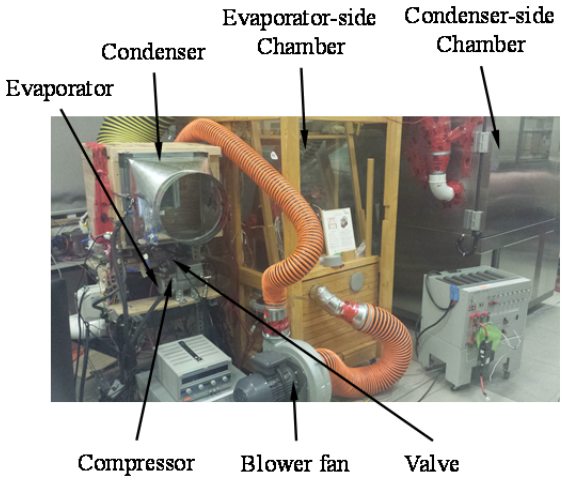

Figure 4.2 Experimental A/C-R system

The experimental setup is shown in Figure 4.2, where the four main components of the whole system and the two chambers are labeled. Figure 4.3 shows one of the environmental chambers. The Micro Motion 2400S transmitter with 0.5% accuracy from Emerson Electric Co. is utilized to log the refrigerant mass flow rate, and it is located between the condenser and the thermostatic expansion valve presented in Figure 4.4. The T-type thermocouples and pressure transducers model PX309

manufactured by OMEGA with 0.25% accuracy shown in Figure 4.5. Figure 4.6 describes T-type thermocouples and the wind sensor model MD0550 from Modern Device. Pressure sensors, thermocouples, and flow meter are installed in different locations indicated in Figure 4.7 for the measurements. Also, The Data Acquisition (DAQ) system is used to collect data from the thermocouples, pressure transducers, DC power supply, and flow meters, and this data is sent to a computer. LABVIEW is employed to obtain all the measured data from equipment and save it in an EXCEL file.

Figure 4.3 Chamber

Figure 4.4 Refrigerant mass flow meter

Figure 4.5 Thermocouple &pressure transducer

Figure 4.6 Air temperature & velocity sensors

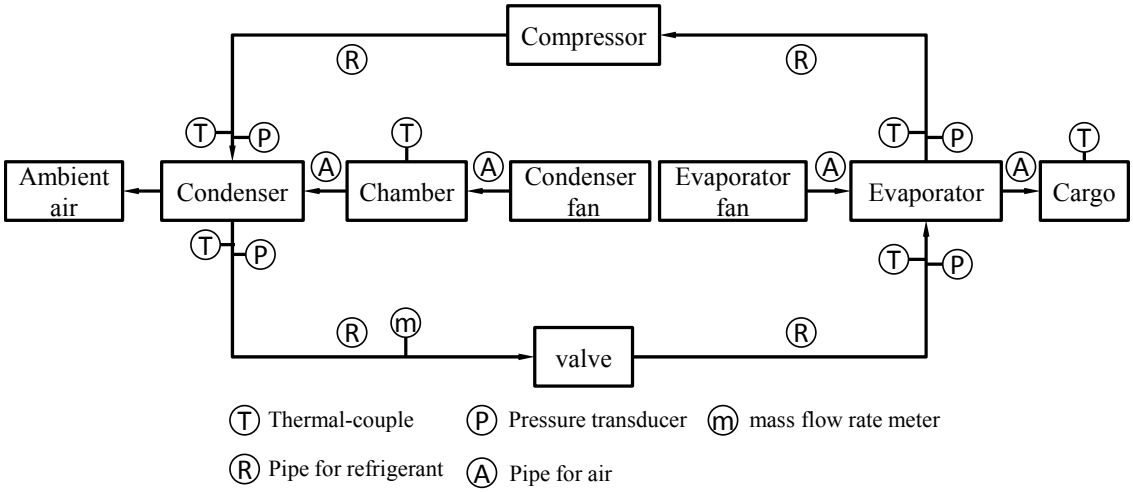

Figure 4.7 Schematic of the whole experimental system

The two fans of the evaporator and condenser are controlled by two VFDs such that the speed could be represented by frequency. While the compressor only has three different speeds, an NI relay module (NI9485) is used to switch between the three discrete speeds.

4.2 Validation

4.2.1 Parameter Estimation

In the vapor compression cycle model, there are three kinds of parameters: physical parameters, empirical parameters, and identified parameters.

4.2.1.1 Physical Parameters

The physical parameters such as the dimensions of pipes, lengths, inner and outer diameters, interior and exterior areas of heat exchangers can be easily measured or obtained from the manufacturers.

4.2.1.2 Empirical Parameters

Empirical parameters can be estimated by empirical equations obtained from experimental data. Most of these parameters vary with working conditions. Therefore, each parameter should be calculated on-line to update its value. For each parameter, several correlations may exist. In the following section, the mean void fraction and the air-side heat transfer coefficient will be discussed in more detail.

The Mean Void Fraction $\overline{\gamma}$

The mean void fraction $\left(\overline{\gamma}\right)$ is defined as the ratio of vapor volume to total volume in the two-phase region and has been employed to describe the characteristics of two-phase flows [37]. Wedekind *et al.* mentioned that the mean void fraction can be assumed invariant during transient processes [35]. However, recently this parameter is assumed to be changed with the fluid quality, and it is defined as the ratio of vapor mass to total mass entering the heat exchangers and calculated by [36, 40].

$$\overline{\gamma} = \frac{1}{\beta} + \frac{1}{x_2 - x_1}\left[\frac{\alpha}{\beta}\ln\left(\frac{\beta x_1 + \alpha}{\beta x_2 + \alpha}\right)\right] \tag{4.1}$$

$$\text{with, } \alpha = \left(\frac{\rho_g}{\rho_l}\right)S \text{ and } \beta = 1 - \alpha$$

where, S is the slip ratio defined as the ratio of vapor velocity and liquid velocity in two-phase sections and identified by test data. x_1 and x_2 are the fluid quality at the inlet and outlet of the two-phase section, respectively.

Air-side Heat Transfer Coefficient α_o

The air-side heat transfer coefficient is related to the energy transferred from the heat exchanger tube wall & fins. But, for different kinds of fins, there are different empirical correlations. In this study, the Colburn j factor is used, which gives a way of relating Reynolds number of airflow through a heat exchanger with experimentally determined heat transfer characteristics of the heat exchanger [34, 38]. The air-side heat transfer coefficient can be found from j factor by using,

$$j = StPr^{2/3} \tag{4.2}$$

where, Colburn j factor is related to Reynolds number and the physical structure of the heat exchanger. For the fin-tube type evaporator, please refer to [126], and for the micro-channel condenser, refer to [127]. Prandtl's number Pr is calculated at air temperature; Stanton number St [34] is related to air-side heat transfer coefficient and defined by:

$$St = \alpha_o \big/ \left(GC_p\right) \tag{4.3}$$

where, G refers to the air mass flux across the heat exchanger and C_p is the thermal conductivity of air at air temperature. By reconstructing the above two equations, the heat transfer coefficient becomes,

$$\alpha_o = jGC_p \big/ Pr^{2/3} \tag{4.4}$$

Mean Air Temperature around Heat Exchangers T_a

This parameter can be assumed as the mean temperature of the air temperature at the inlet and outlet of the heat exchanger [34]. Taking the evaporator as an example, in order to find the air temperature at the outlet of the heat exchanger, T_{ae} should be calculated beforehand by:

$$T_{ae} = \left(2\left(\frac{\dot{m}_{air\_e}C_{p,air}}{\alpha_{oe}A_{oe}}\right)T_{e\_air\_in} + T_{wfe}\right) \Bigg/ \left(2\left(\frac{\dot{m}_{air\_e}C_{p\_air}}{\alpha_{oe}A_{oe}}\right)+1\right) \tag{4.5}$$

where, $\dot{m}_{air\_e}$ refers to the air mass flow rate going through the evaporator while C_{p_air} means the specific heat of the air. In this process, $\dot{m}_{air\_e}$ is proportional to the evaporator fan control signal N_{evap}. This proportional coefficient can be identified by using experimental data. T_{ac} at the condenser side can be calculated in a similar manner. $T_{e\_air\_in}$ is the air temperature at the inlet of the evaporator and measured by thermal couples.

4.2.1.3 Identified Parameters

Identified parameters, such as the equivalent refrigerant-side heat transfer coefficients and the equivalent temperature of wall & fins, refer to those that are obtained by experimental data. Regarding the steady state test for parameter identification, the system is fed by three inputs and the two temperatures shown in the known parameters column of Table 4.1. After running for about 30 minutes, the system approaches the steady state. The data of temperatures, pressures, and refrigerant mass flow are collected by using the sensors mentioned in experiments and model validation section. The parameters and states in the identified parameter column are identified off-line by using the least square method based on the collected data.

Table 4.1 The known and identified parameters at one steady state

Known parameters	***Values***	***Identified parameters***	***Values***
$N_{comp}\,(rpm)$	4500	$l_e\,(m)$	2.0137
$N_{evap}\,(Hz)$	41.3	$l_c\,(m)$	0.2528
$N_{cond}\,(Hz)$	52.5	$T_{wfe}\,(^{\circ}C)$	3.84
$T_{e\_air\_in}\,(^{\circ}C)$	20	$T_{wfc}\,(^{\circ}C)$	33.9
$T_{c\_air\_in}\,(^{\circ}C)$	27	$\alpha_{ie}\,(kw/(m^2K))$	0.68
$P_e\,(bar)$	2.23	$\alpha_{ic}\,(kw/(m^2K))$	1.9
$P_c\,(bar)$	8.95	$\alpha_{iesh}\,(kw/(m^2K))$	0.045
$T_{sh}\,(^{\circ}C)$	2.74	$\alpha_{icsh}\,(kw/(m^2K))$	0.13

The known parameters include the inputs of the system, the working conditions as well as the measurements; whereas, the identified parameters consist of immeasurable states and refrigerant-side heat transfer coefficients. Here, the equivalent two-phase heat transfer coefficient, α_{ie}, for evaporator is elaborated. From Table 4.1, this parameter for evaporator is $0.68\,kw/(m^2K)$; whereas, the reported value in the literature is usually between 1 and $5\,kw/(m^2K)$. That is because after considering the fins' effects, the identified equivalent temperature of the tube wall & fins T_{wfe} becomes higher than the temperature of the exact tube wall at the evaporator side. The temperature difference $(T_{wfc}-T_{rc})$ from the refrigerant saturation temperature at the current pressure is larger too. In order to balance the

transferred energy of the two-phase section $\alpha_{ie}\pi D_i l_e \left(T_{wfc} - T_{rc}\right)$, the equivalent heat transfer coefficient must be smaller than that estimated by Pierre's empirical correlation [40]. As a result, this coefficient is called the equivalent coefficient, and the same thing happens for its counterpart of the condenser.

4.2.2 Comparison Results

Using the experimental setup, different experiments are conducted, where some are used for parameter identifications and the rest for model validation. For the simulation work, the initial conditions and unknown parameters are identified off-line by one set of experimental data as stated in parameter identification section, and the model is evaluated using the other unseen data. In the following, several other sets of data are used to validate the model by comparing the experimental and simulation results in three different scenarios.

In the first scenario, the speeds of the condenser fan and the compressor change while the speed of the evaporator fan remains unchanged during the 5500-seconds simulation as seen in Figure 4.8. Figure 4.9 shows the air temperature at the outlet of condenser and evaporator while the inlet temperatures are measured and fed to the model. The air temperature at the outlet agrees with test data but with a little discrepancy, which is probably caused by using the constant refrigerant-side heat transfer coefficient. For the sake of more accurate, in the future, this coefficient should be identified on-line.

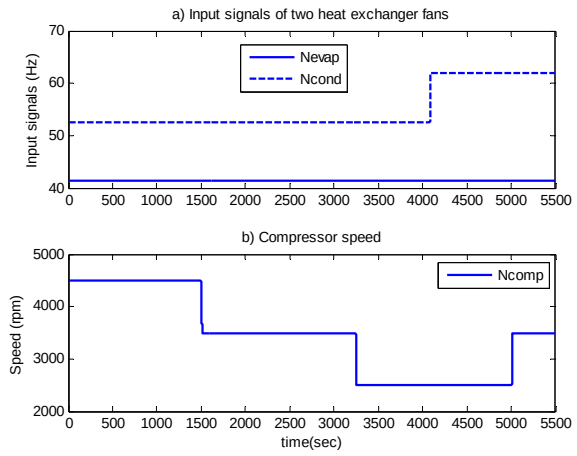

Figure 4.8 Inputs of the system

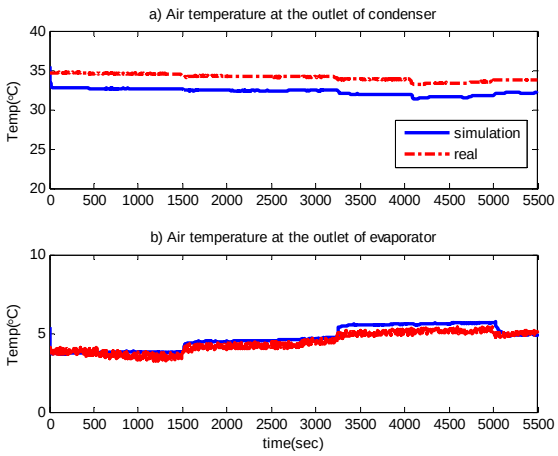

Figure 4.9 Air temperature at the outlet of two heat exchangers

In order to keep the superheat to a certain degree, the expansion valve has to turn down or turn up. As a result, the real temperature at the outlet of evaporator always oscillates. Given that the thermostatic valve model is identified by steady state data, it is difficult to simulate this oscillation, but this phenomenon could be overcome by the use of dynamic test data in the future. Thus, the simulation result is located in almost the middle of the test data; whereas, the temperature at the inlet has a great match between simulation results and test data presented in Figure 4.10. Figure 4.11, the simulation results of the refrigerant temperature at the condenser side also fit the test data. Figure 4.12 describes good agreements between actual evaporator and condenser pressures and model prediction.

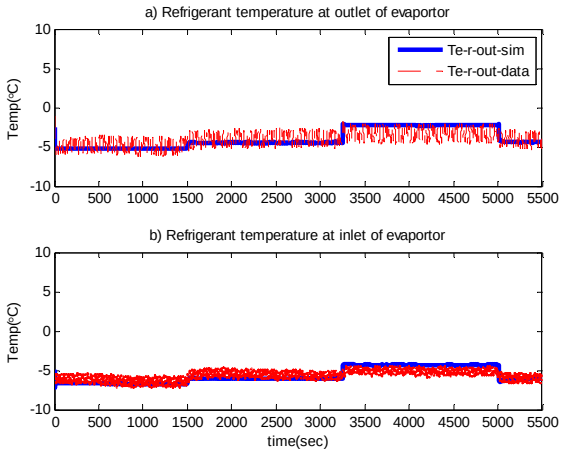

Figure 4.10 Refrigerant temperature at inlet and outlet of evaporator

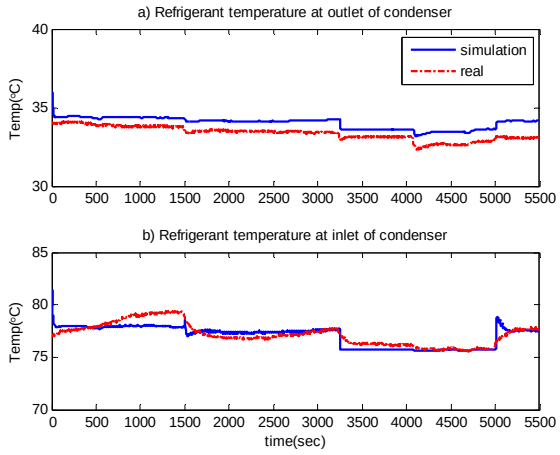

Figure 4.11 Refrigerant temperature at inlet and outlet of condenser

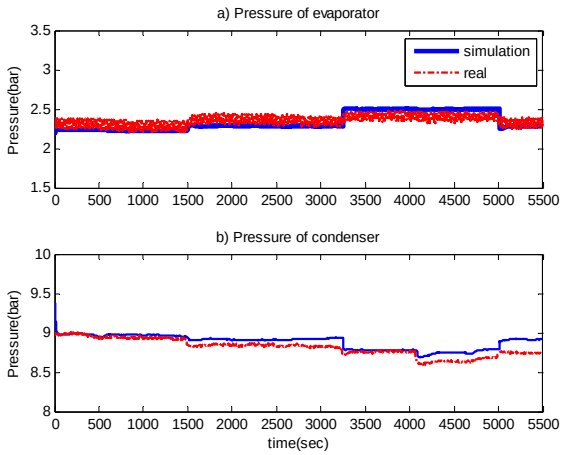

Figure 4.12 Pressures of evaporator and condenser

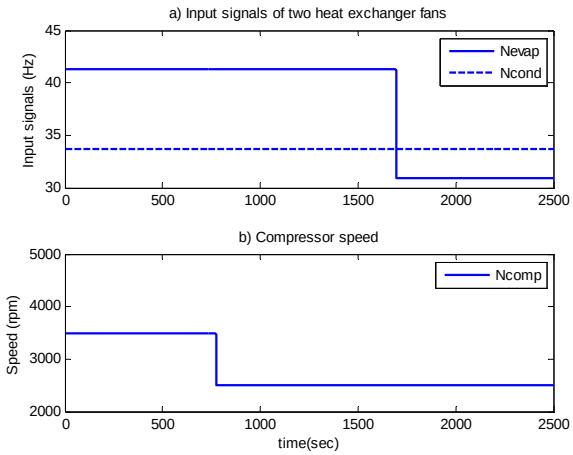

Figure 4.13 Inputs of the system

In the second scenario, the speeds of the evaporator fan and the compressor are varied and the speed of condenser fan is invariant indicated in Figure 4.13. From Figure 4.14 to Figure 4.17, conclusions similar to those from the first scenario can be drawn during the 2500-second simulation.

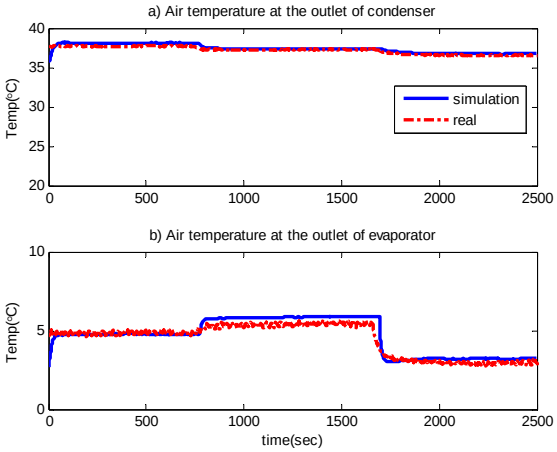

Figure 4.14 Air temperature at the outlet of two heat exchangers

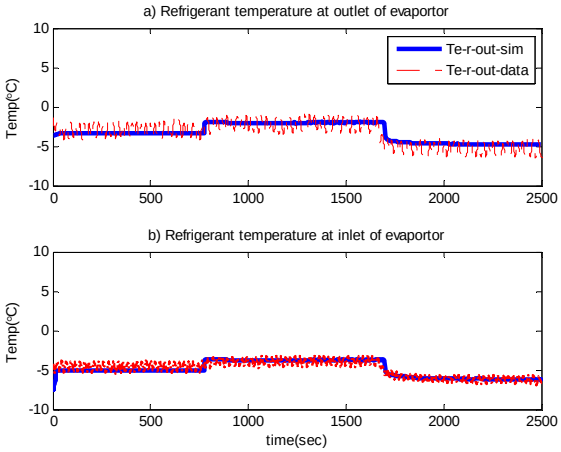

Figure 4.15 Refrigerant temperature at inlet and outlet of evaporator

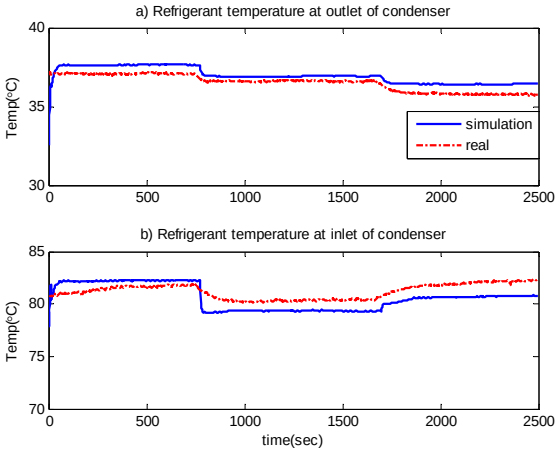

Figure 4.16 Refrigerant temperature at inlet and outlet of condenser

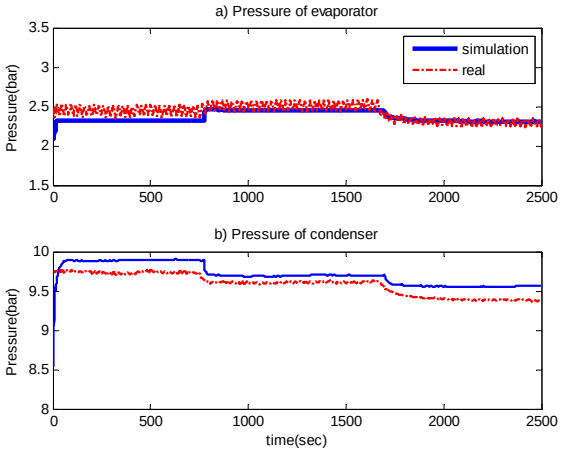

Figure 4.17 Pressures of evaporator and condenser

In the last scenario, the input pattern is more complex; at the 560th second, three inputs were changed as depicted in Figure 4.18. However, from Figure 4.19 to Figure 4.22, it can be seen that the simulation results also fit the test data. However, due to the high nonlinear nature of the system, any system parameter can be affected by each of the three inputs. Taking the evaporator pressure in Figure 4.22 for example, it can be seen that it is influenced by both N_{evap} and N_{comp}. The pressure

increases as N_{comp} decreases and decreases N_{evap} as decreases. That is why at the 560th second, the evaporator pressure does not change very much. While in Figure 4.20, the refrigerant temperatures are closely related to the evaporator pressure. The temperature at the inlet of the evaporator is the saturation temperature under the evaporator pressure, and the temperature at the outlet of the temperature is the sum of the saturation temperature and the superheat temperature. That is why they remain fairly constant when inputs are changed.

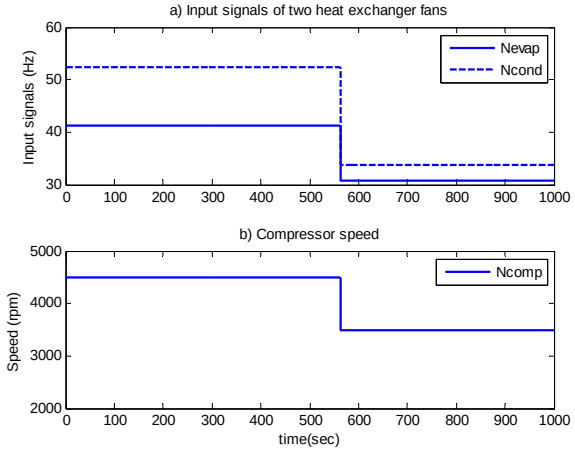

Figure 4.18 Inputs of the system

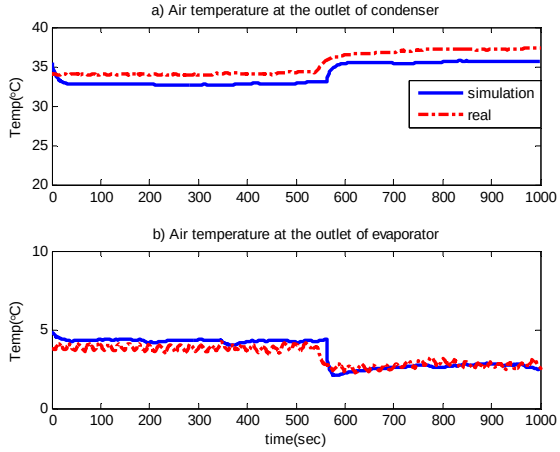

Figure 4.19 Air temperature at the outlet of two heat exchangers

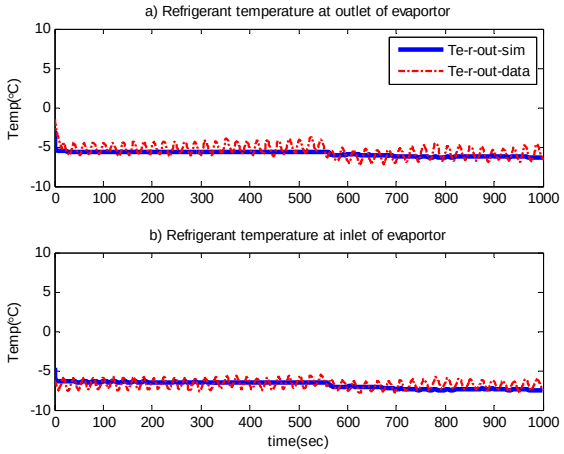

Figure 4.20 Refrigerant temperature at inlet and outlet of evaporator

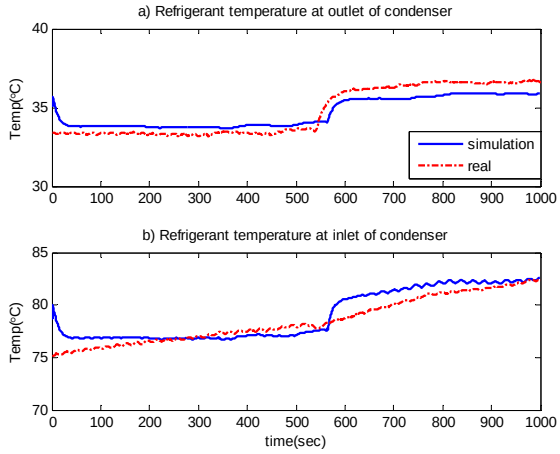

Figure 4.21 Refrigerant temperature at inlet and outlet of condenser

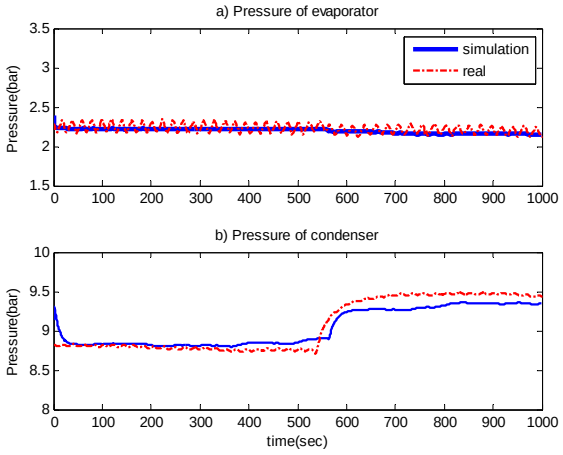

Figure 4.22 Pressures of evaporator and condenser

The comparison results are given in the form of the mean absolute percentage error (MPAE) in Table 4.2. The value is the average of the three scenarios. From the results, it can be seen that the model prediction is accurate and can be used in MPC development.

Table 4.2 The MPAE between simulation and test data

Parameters	***MAPE*** (%)
Evaporator pressure	2.77
Condenser pressure	1.06
Refrigerant temp at outlet of Condenser	1.66
Refrigerant temp at inlet of Condenser	0.96
Refrigerant temp at outlet of evaporator	8.66
Refrigerant temp at inlet of evaporator	8.43
Air temp at outlet of evaporator	8.69
Air temp at outlet of condenser	3.27

4.3 Experimental Powertrain System

As illustrated in Figure 4.23, the HIL setup includes one input AC dynamometer motor for simulating vehicle engine and two identical output AC dynamometers for simulating drive and service loads. The input and output dynamometers, which are from Mustang Dynamometers, include +-0.1% accuracy torque meters, magnetic speed sensors, and Compact Logix controller. The input dynamometer (A) is connected to the output dynamometer (B) via a 6-speed manual transmission (Eaton Fuller FS-5306A.), which can be automatically shifted by a designed pneumatic system based on shifting

strategy. The other output dynamometer (C) is connected to a PTO (E, Muncie CS6), which is attached to the gearbox (D) and utilized to transfer power from the engine to the auxiliary devices. The PTO is engaged or disengaged by a pneumatic system. A portion of the power generated by the input dynamometer is transferred through the transmission to one of the output dynamometers that simulates drive load. The remaining goes to the second dynamometer that simulates the auxiliary load through the PTO. The alternator (F) is connected to a battery (G) and the input dynamometer by a serpentine belt, where the battery is discharged by a controllable heater used to simulate the auxiliary device illustrated in Figure 4.24.

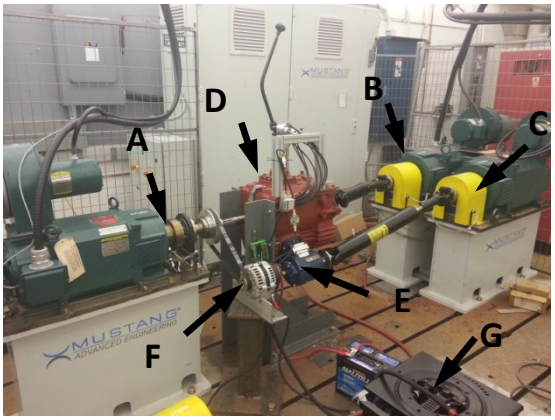

Figure 4.23 HIL setup

Figure 4.24 The controllable heater

4.4 Summary

This chapter elaborated both experimental systems for the A/C-R system as well as the powertrain system. The models are comprehensively validated experimentally. The validation results of the A/C-R system are presented; whereas, the results for the powertrain validation are provided in the thesis of my teammates [128].

Chapter 5
Development of A/C-R Controllers and Analysis

This chapter presents the development process of several A/C-R system controllers including an on/off controller, a PI controller, a set-point optimizer with an SMC and a linear MPC, as well as their results and comparison analysis [129] [130]. The objective is to find the most promising controller in terms of both the controlled temperature performance and energy saving.

5.1 Controller Development

5.1.1 On/off Controller

The on/off controller is most commonly used in A/C-R systems. However, as mentioned in Chapter 2, the drawbacks hinder its future development. Thus, the on/off controller developed in this section is used as a basis to compare to other proposed controllers. In this study, only the constant compressor speed during the on mode is considered. The controller is driven by the error signal between the measured temperature and the temperature set point in the specific space [36], and the idea is that it is actually utilizing a simple logic:

1) If the current cargo space temperature is higher than the upper band, the compressor will be turned on.
2) If the current cargo space temperature is lower than the lower band, the compressor will be shut down.
3) If the current cargo space temperature is between the upper and lower band, compressor state will keep unchanged.

The schematic of the whole system with the on/off controller is displayed in Figure 5.1,

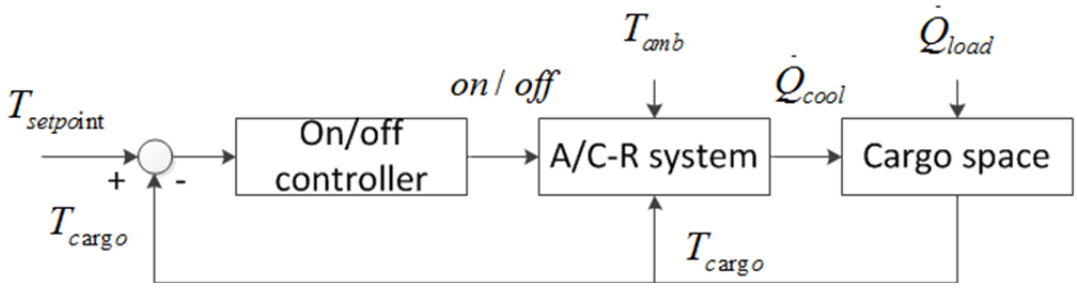

Figure 5.1 Diagram of the on/off controller

The controller is modeled by using the state machine in MATLAB/Simulink in accordance with the logic rules above. After comparing the actual cargo temperature and its reference, the on/off control signal is delivered to the A/C-R system to switch on or off the whole system.

5.1.2 PI Controller

This controller is also commonly used in the A/C-R system with the variable-speed components, because of its simplicity and better performance than the On/off controller if properly being tuned. As known, generally, the A/C-R system is controlled to quickly reach and maintain the desired temperature. Meanwhile, it should maximize the coefficient of performance (COP) while guarantee properly operating (*e.g.* avoid the vapor-phase refrigerant entering the compressor). The COP, a ratio between the cooling or heating capacity taken away and the whole power consumption, is usually used to indicate the energy efficiency of the A/C-R system. Therefore, employing two PI controllers to control the cargo temperature and superheat respectively is the first choice for A/C-R control engineers [131]. In this method, one controller is for the cargo temperature control by manipulating the compressor pump speed, while the other one is for the superheat control by adjusting the electric expansion valve opening in order to enhance the system COP and prevent liquid refrigerant enters the compressor. Due to the features of the studied A/C-R system that the compressor with discrete speeds and thermostatic expansion valve are used, the existing PI controller cannot be utilized. Therefore, an updated version of PI controller is developed. A simple logic rule shown in Equation (5.1) will be applied for compressor speed control instead of using a PI controller. The cargo temperature is controlled by a PI controller to manipulate the evaporator fan speed.

$$\begin{cases} N_{comp} = 4500 & if \quad e > 1 \\ N_{comp} = 3500 & elseif \quad 0.5 < e \le 1 \\ N_{comp} = 2500 & else \end{cases} \tag{5.1}$$

The structure of the whole model is described in Figure 5.2. The outputs of the controller are compressor pump speed $\left(N_{comp}\right)$ and $\left(N_{evap}\right)$, and they serve as two inputs for the A/C-R block; whereas, the other one input, condenser fan speed $\left(N_{cond}\right)$ is kept unchanged at their initial values.

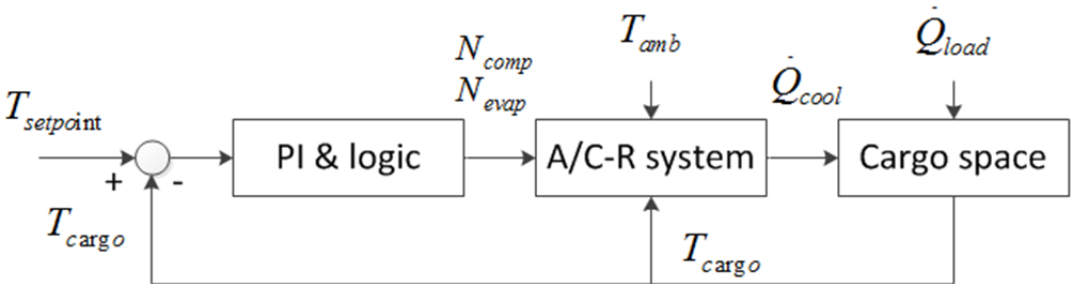

Figure 5.2 PI controller model structure diagram

5.1.3 Set-point Controller

Due to the drawbacks of the on/off controller and the conventional PI controller, such as with large temperature oscillations and energy-consuming, an energy-saving controller is proposed in this section.

The idea behind the proposed controller is that the steady state of the A/C-R system is mainly related to the temperature set point of the cargo $\left(T_{setpoint}\right)$, the ambient temperature $\left(T_{amb}\right)$ and the total heating load applied onto the cargo $\left(\dot{Q}_{load}\right)$. That means the A/C-R system will stay at a steady state after settling down unless the above parameters change. However, these parameters represent working conditions and change in a very low frequency. The preliminary study of the steady state model demonstrates that the correlation of the total power consumption with respect to the condenser and evaporator pressure is a convex function shown in Figure 5.3.

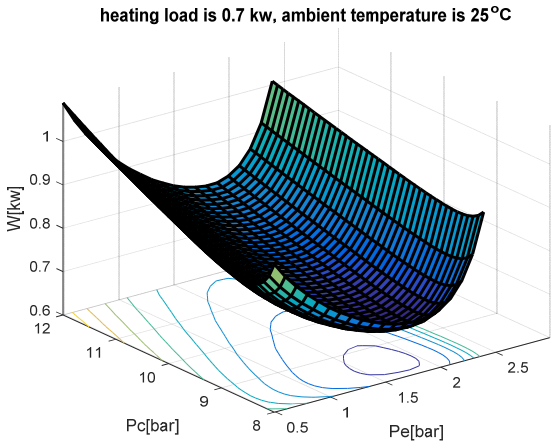

Figure 5.3 A/C-R system power consumption with respect to two pressures

Therefore, the condenser and evaporator pressure can be obtained according to the steady state model and sent to controllers as the set points, where the system consumes the minimum energy. Together with the pressure set points, there are totally three set points and three control inputs in the system. Intuitively, three individual classic controllers, such as PI controller, can be employed to track the obtained set points. The sensitivity analysis based on some preliminary simulations suggests that the evaporator pressure (P_e), the condenser pressure (P_c), and the cargo temperature (T_{cargo}) are main changed with respect to and N_{comp}, N_{cond} as well as N_{evap}, respectively.

However, due to the MIMO and highly nonlinear nature of the A/C-R system, the classic controllers cannot bring better results than the on/off controller in terms of both control performance and energy consumption. Therefore, as the main control objective, the cargo temperature set point will be tracked by an SMC due to its robustness and applicability in nonlinear systems. For the sake of simplicity, a PI controller is still used for condenser pressure tracking. Due to the existence of a discrete input in the real experimental system, a simple logic rule shown in (5.1) will be applied for compressor speed control instead of using a PI controller, where, e is the error of the real temperature and its set point.

Two reasons support that the temperature error is used as the index to switch the compressor speed instead of the pressure error as mentioned above. First of all, as the main power consumption component in the A/C-R system, the compressor speed is roughly proportional to its power consumption. In order to save energy at the maximum, the compressor should run at its lowest possible speed under the condition that the cargo temperature should reach its set point. That is why the compressor speed decreases with the temperature error. This will be also demonstrated by the experimental test data in next section. Then, in case the set-point optimizer fails to find the optimal pressure set point under some extreme conditions, the controller is still working as long as the temperature sensor is working well. Finally, the whole controller structure is shown in Figure 5.4.

As aforementioned, the optimizer as the supervisory controller is to find the set points of two pressures based on the varying working conditions, which is the outer loop and works in low frequency (e.g.in hours); whereas the inner loop controller is composed of a PI controller, a rule-based controller, and an SMC. The optimizer can also be implemented as a lookup table to find pressure set points based on the working condition changes and the steady state model. The detailed developing process is discussed in Figure 5.5 and explained as follows: two pressures (P_e, P_c) as the

optimization variables firstly are sent to some predefined lookup tables to find all the thermodynamic parameters of the refrigerant, such as the temperatures, entropies, and enthalpies. All the steady-state values of the states are calculated based on Equation (3.34) ~ (3.36) and Equation (3.42) ~ (3.44). Together with the working conditions $\left(T_{setpoint}, \dot{Q}_{load}, T_{amb}\right)$ and the related equations, the total power consumption of the A/C-R system can be obtained. Thus, under each working condition, the whole process can be repeated until the minimum power consumption and the corresponding pressures are calculated. Finally, the optimal pressures and the working conditions are built into two 3D lookup tables for determining the pressure set points, which will be sent to the local controllers for set-point tracking.

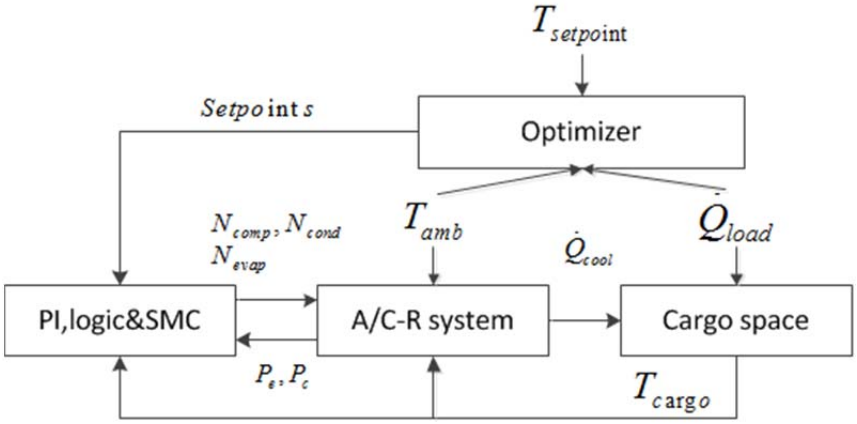

Figure 5.4 Diagram of A/C-R system with set-point controller

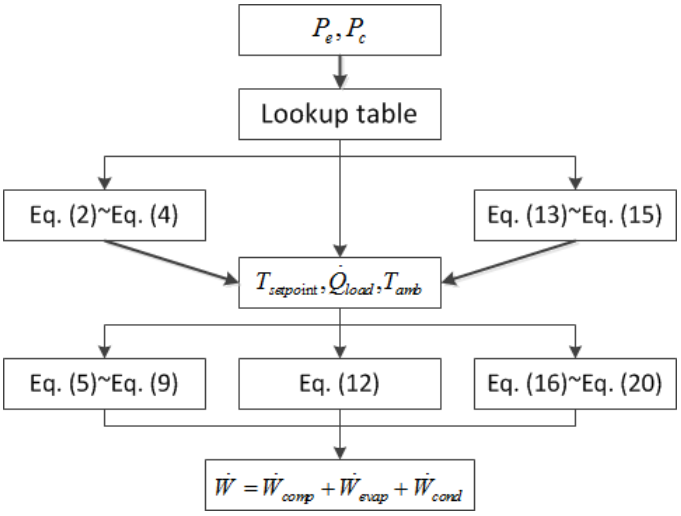

Figure 5.5 The optimizer developing process

In the SMC, the saturation function is used instead of the sign one to get rid of the chattering phenomenon [132]. The sliding surface S and control input N_{evap} are derived by the algorithm [133] according to Equation (3.37) and (3.54):

$$S = \lambda\left(T_{setpoint} - T_{c\arg o}\right) \tag{5.2}$$

$$N_{evap} = \frac{\dot{m}_{e\_air0}}{k_e}\left\{\frac{sat\left(S/\phi\right)k\rho_{air}VC_{p\_air} + \dot{Q}_{load}}{k_e\alpha_{oe0}A_{oe}\left(T_{ae} - T_{wfe}\right)}\right\}^{(1-m)} \tag{5.3}$$

5.1.4 Nonlinear MPC

Due to the high nonlinearity and MIMO nature of the A/C-R system, the conventional controllers cannot obtain the optimal performance. As a result, the advanced nonlinear MPC (NMPC) will be developed in this section, which is an optimal control method and suitable for MIMO system. The basic idea of the MPC is that it utilizes the dynamic model to predict the future behavior of the plant and decides the optimal system inputs based on a given objective function. The nonlinear model is considered as the predictive model and can be discretized and formulated in the following form:

$$\begin{aligned} x(k+1) &= f\left(x(k), u(k)\right) \\ y(k) &= g\left(x(k), u(k)\right) \end{aligned} \tag{5.4}$$

where, f and g are known and generally nonlinear mapping. $x \in R^n$ and $u \in R^m$ are the state vector and input vector. Each of these vectors can be subjected to linear or nonlinear constraints X and U. With this predictive model, the future states $x(k)$ and outputs trajectories $y(k), k = 0,1,2\cdots N_p - 1$ can be predicted based on the current state vector $x(0)$ measured or observed at the current time t_0 and any given control sequence $u(0), u(1), \cdots u(N_c - 1)$ with the control horizon length $N_c \geq 2$ The horizon length of the predictive states and outputs can be N_p, a larger value than N_c. However, in this study they are assumed the same and denoted by N.

MPC is usually used to solve the tracking problems (regulation can be considered as the special case of tracking problems, where the reference signals are zeros). This means that if the current outputs (or states) are far away from the reference $y_{ref}(k)$ then the MPC algorithm can drive the system towards the reference and if the current outputs are already close enough to the reference signals then the algorithm will keep it there. As a result, a cost function should be introduced to demonstrate how far the current outputs are away from their references. Generally, this function, not

only penalizing the deviation of the outputs from the reference but also the input effort, is formulated in a quadratic form:

$$l\left(y(k),u(k)\right)=\frac{1}{2}\left(y(k)-y_{ref}(k)\right)^{T}Q\left(y(k)-y_{ref}(k)\right)+\frac{1}{2}u^{T}(k)Ru(k) \tag{5.5}$$

where, Q and R are weight matrices, the former one is semi-positive definite diagonal matrix while the later one is a positive definite diagonal matrix. The optimal problem can be formulated as follows:

$$\min_{u(\cdot)} J\left(x(0),u(\cdot)\right)=\min_{u(\cdot)}\sum_{k=0}^{N-1}l\left(y(k),u(k)\right) \tag{5.6}$$

with respect to all the admissible control sequence $u(\cdot)$, which is denoted by $u(0),u(1),\cdots u(N_c-1)$ and the current state vector $x(0)$. The admissible control sequence means that the control sequence should belong to its constraint U and the state trajectory calculated by this control sequence should belong to its own constraint X. After this constrained optimal problem is solved, the optimal control sequence will be $u^*(0),u^*(1),\cdots u^*(N_c-1)$. Only the first element $u^*(0)$ is applied to the system and the whole procedure is repeated with new measurements or observation $x(k)$. This whole procedure is depicted in Figure 5.5.

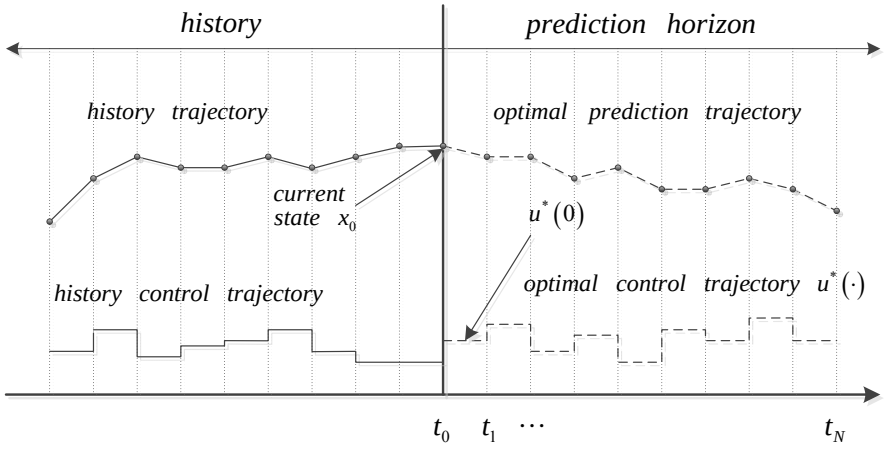

Figure 5.6 Illustration of the MPC scheme [134]

The nonlinear optimization problem at each time instant is solved by command "*fmincon*" in the MATLAB function library. This function is a general function for finding the minima of a constrained function, which includes many types of constraints, such as linear, nonlinear, terminal cost and terminal constraints.

5.1.5 Linear MPC

As an optimal control method, the MPC originated in the chemistry industry's control techniques. It is characterized by its slow dynamics, which provides enough time for optimization calculations [69]. As is known, the A/C-R system is a highly nonlinear MIMO system with slow dynamics making it suitable for MPC application. In general, three parts are included in an MPC: a predictive model that aims to predict future behavior of the process, a receding horizon optimization algorithm that will solve an explicit optimization problem formulated into several future sampling periods, and feedback correction to keep the controlled variables at the set points and enhance the robustness of the A/C-R control system [134].

Using a highly complex nonlinear model for the development of a model predictive controller, the computational efficiency will be extremely low, so its real-time implementation will become expensive or even unrealistic for industrial applications. To solve this problem, a linear MPC will be developed in this paper. After linearizing and discretizing the nonlinear model provided in the Appendix A, a finite horizon optimization problem [135] is formulated at each time interval. The objective function is shown below,

$$J\left(x_0,u_0\right)= \; e\left(N\right)^T Pe\left(N\right)+\sum_{k=0}^{N-1}\left[e\left(k\right)^T Qe\left(k\right)+u\left(k\right)^T Ru\left(k\right)+\Delta u\left(k\right)^T S\Delta u\left(k\right)\right]$$

s.t.

$$\begin{aligned} x_{min} \le x\left(k\right) \le x_{max}, \quad k=0,\ldots N-1 \\ u_{min} \le u\left(k\right) \le u_{max}, \quad k=0,\ldots N-1 \\ \Delta u_{min} \le \Delta u\left(k\right) \le \Delta u_{max}, \quad k=0,\ldots N-1 \end{aligned} \tag{5.7}$$

where, e is the tracking error of the temperature; the first term on the right-hand side is the terminal cost; the second term is stage cost; the third term represents control effort cost and the last term is control input rate costs. $P,Q,R,$ and S are weights to balance each term. The objective function is transferred into a quadratic form with respect to the increment of control inputs. As the prediction horizon length is N, the deviation trajectory of future states will be obtained by the discrete-time model:

$$\underbrace{\begin{bmatrix}\Delta x(1)\\ \Delta x(2)\\ \vdots\\ \Delta x(N)\end{bmatrix}}_{\Delta\bar{X}}=\underbrace{\begin{bmatrix}A\\ A^2\\ \vdots\\ A^N\end{bmatrix}}_{S^{\Delta x}}\Delta x(0)+\underbrace{\begin{bmatrix}B & 0 & \dots & 0\\ AB & B & \dots & 0\\ \vdots & \vdots & \ddots & 0\\ A^{N-1}B & A^{N-2}B & \dots & B\end{bmatrix}}_{S^{\Delta u}}\underbrace{\begin{bmatrix}\Delta u(0)\\ \Delta u(1)\\ \vdots\\ \Delta u(N-1)\end{bmatrix}}_{\Delta\bar{U}} \tag{5.8}$$

Then, the deviation of the future outputs can be rewritten into a compact form by:

$$\underbrace{\begin{bmatrix}\Delta y(1)\\ \Delta y(2)\\ \vdots\\ \Delta y(N)\end{bmatrix}}_{\Delta\bar{Y}}=\underbrace{\begin{bmatrix}C & 0 & 0 & 0\\ 0 & C & 0 & 0\\ 0 & 0 & \ddots & 0\\ 0 & 0 & 0 & C\end{bmatrix}}_{C^{\Delta x}}\Delta\bar{X} \tag{5.9}$$

The convex quadratic objective function only with respect to the increment of inputs will be obtained by inserting Equation (5.8) into the original objective function shown in Equation (5.7) and neglecting the constant term:

$$J(x_0,u_0)=\frac{1}{2}\Delta\bar{U}^T H\Delta\bar{U}+\Delta\bar{U}^T g$$

$$H=2\left(C^{\Delta X}S^{\Delta U}\right)^T\bar{Q}\left(C^{\Delta X}S^{\Delta U}\right)+\bar{R}+\bar{S},\quad g=2\left(C^{\Delta x}S^{\Delta u}\right)^T\bar{Q}\left(C^{\Delta x}S^{\Delta u}-\bar{Y}_{ref}\right)$$

s.t. (5.10)

$$\Delta\bar{U}\geq max\left(\Delta\bar{U}_{min}(U),\Delta\bar{U}_{min}(\Delta\bar{U}),\Delta\bar{U}_{min}(X)\right)$$

$$\Delta\bar{U}\leq min\left(\Delta\bar{U}_{max}(U),\Delta\bar{U}_{max}(\Delta\bar{U}),\Delta\bar{U}_{max}(X)\right)$$

where the Hessian matrix (H) is symmetric and positive or semi-positive definite and g is the gradient vector. $\bar{Q},\bar{R},\bar{S}$ and $\bar{Y}_{ref}$ should be reformulated according to the prediction horizon length N based on Q,R,S and Y_{ref}. The updated constraints of the increment of the control can be found by the reformulation of Equation (5.8) and the constraints shown in Equation (5.7). For example, the constraints of the states can be applied to $\Delta\bar{U}$ as $\Delta\bar{U}_{max}(X)$ by Equation (5.8). Since the optimal result is the small variation $\Delta\bar{U}$, the real optimal $\bar{U}$ can be obtained by adding the initial input U_0. The first element of the optimal solution will be applied to the real system. This linear MPC is implemented into MATLAB/SIMULINK and LabVIEW for simulation and experiment, respectively. The detailed structure of the MPC in the Control & Simulation Loop in LABVIEW is depicted in Figure 5.7. First, the thermodynamic properties, such as density, enthalpy, and entropy, of the refrigerant under the current working conditions are obtained online by feeding the fresh measurements into lookup tables followed by parameter and state identification, where some

unknown parameters and states are identified online. Then, all the known information is sent to the MPC algorithm, whose output is a quadratic problem (QP), shown in Equation (5.10). A QP open source solver [136] which is originally written in C, is also integrated into the Control & Simulation Loop in LABVIEW and solves the QP at each time interval. The outputs will be delivered to the evaporator and condenser fans as well as the compressor pump via some other NI DAQs control modules to regulate their speeds. If the three control inputs are continuously varying in their ranges, the MPC is the continuous one. Due to the discrete constraint of the compressor speed (*i.e.* low, medium and high speed), the discrete MPC (designed for the system with discrete input values) is designed as shown in Figure 5.8, where three continuous MPC (designed for the system with continuous input values) are employed and solved simultaneously at each time interval. Each of these works at one compressor speed to find the optimum solutions for the other two inputs and the cost values. Then, the three cost values are compared to determine the minimum value, and their three corresponding inputs are used as the optimal solutions.

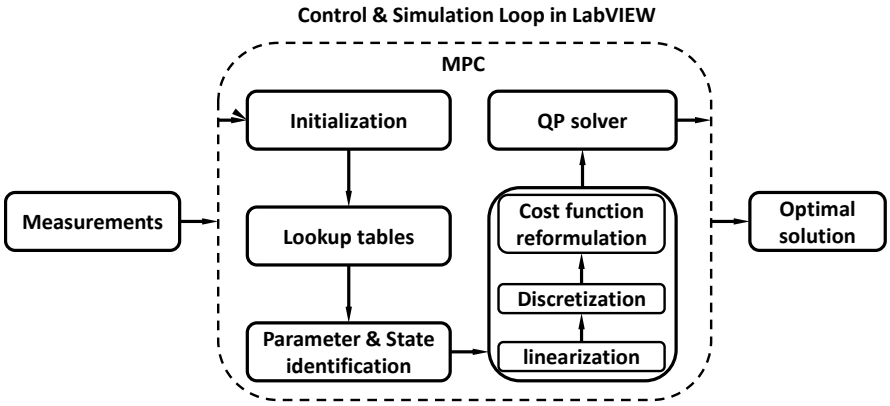

Figure 5.7 MPC structure in LabVIEW

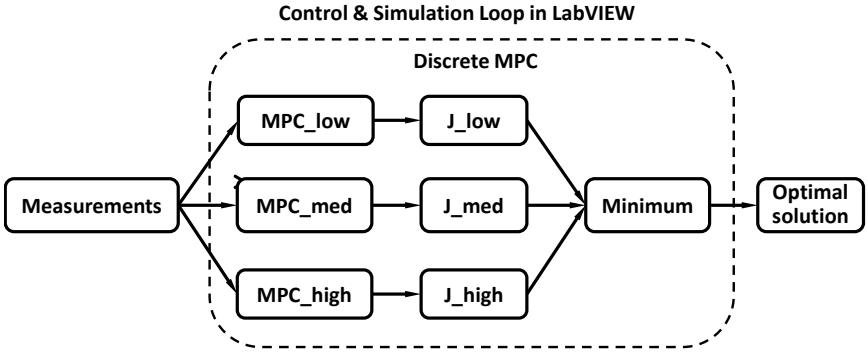

Figure 5.8 Discrete MPC structure in LabVIEW

5.2 Real Performance Comparison

Due to the nonlinear and MIMO nature of the A/C-R system, it is difficult to tune the conventional PI controller in order to obtain the good performance. Besides, the development process of the PI controller is almost similar as that of the set-point controller but without considering the energy saving aspect. Therefore, some preliminary simulation results show that PI is worse than the set-point controller. In addition, the nonlinear MPC takes about 100 times computational time than the real time to obtain the optimal solution, and thus it cannot be run in the real system. Therefore, the on/off, set-point controller and linear MPC are implemented into the real experimental system to test and compare their performance in terms of both controlled temperature performance and energy consumption.

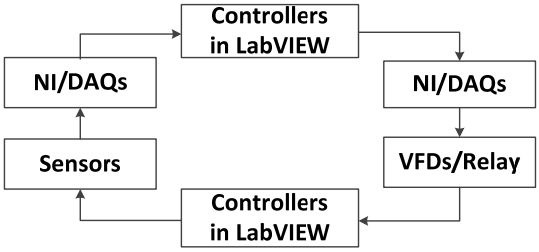

Figure 5.9 Diagram of experimental system with controllers

To study the A/C-R energy consumption at different ambient temperatures, the condenser is connected to an environmental chamber whose temperature is controlled. Three different temperatures $\left[20^{\circ}C;25^{\circ}C;30^{\circ}C\right]$ are chosen for the experiments. The cargo used in the experiments is a $2m^3$ wooden chamber shown in Figure 4.2. 15 thermocouples are employed to measure the temperature at different locations. In the experiments, an average temperature of 7 thermocouples closer to the air inlet of the condenser was used as the controlled temperature. Three different temperatures $\left[16^{\circ}C;17^{\circ}C;18^{\circ}C\right]$ are chosen as the temperature set points of the air inside the cargo. Table 5.1 shows the operating conditions and system constraints for experiments.

Table 5.1 Operating conditions and constraints of inputs and states

$T_{amb}\left(^{\circ}C\right)$	$T_{cargo\_init}\left(^{\circ}C\right)$	$T_{setpoint}\left(^{\circ}C\right)$	$\dot{Q}_{door}\left(kW\right)$	$N_{evap}\left(Hz\right)$	$N_{cond}\left(Hz\right)$	$N_{comp}\left(rpm\right)$	$P_e\left(bar\right)$	$P_c\left(bar\right)$
$\begin{bmatrix}20\\25\\30\end{bmatrix}$	22.5	$\begin{bmatrix}16\\17\\18\end{bmatrix}$	0.15	$\left[0\sim40\right]$	$\left[0\sim40\right]$	$\begin{bmatrix}2500\\3500\\4500\end{bmatrix}$	$\left[1\sim7\right]$	$\left[1\sim17\right]$

Experimental scenarios are provided in Table 5.2, and three cases with different cargo temperature set point and ambient temperature are studied and compared.

Table 5.2 Experimental cases

Case1		Case2		Case3	
T_{amb} $(^{\circ}C)$	$T_{setpoint}$ $(^{\circ}C)$	T_{amb} $(^{\circ}C)$	$T_{setpoint}$ $(^{\circ}C)$	T_{amb} $(^{\circ}C)$	$T_{setpoint}$ $(^{\circ}C)$
25	16	25	17	30	17

5.2.1 On/off Controller

The hysteresis band is an important parameter in the on/off controller, which should be determined before running the simulation. It decides the temperature oscillation and switching frequency of the whole cycle and subsequently, the wear condition of the compressor. If the threshold is too large, the temperature variation amplitude is too large. Otherwise, the system will be switched on and off too frequently. Therefore, for the sake of a trade-off between the two aspects, $\pm 1^{\circ}C$ is chosen as the band by the preliminary experiment study.

For the controller performance analysis, several experiments in different scenarios mentioned in Table 5.1 are performed. During the tests, an external disturbance of approximately 20% of the original heating load (the 200-second dot-line region) was applied to the chamber to simulate the disturbance caused by an opening door.

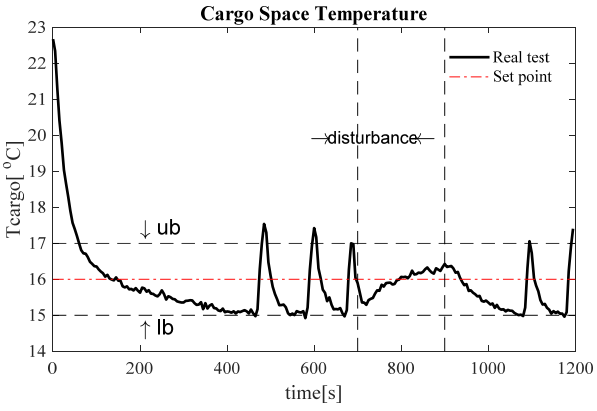

Figure 5.10 Controlled temperature under case1

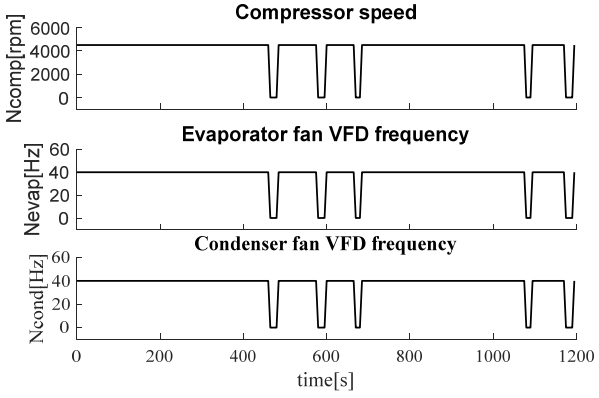

Figure 5.11 System inputs under case1

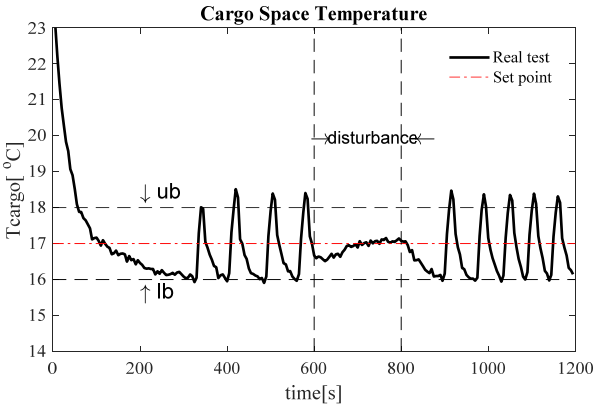

Figure 5.12 Controlled temperature under case2

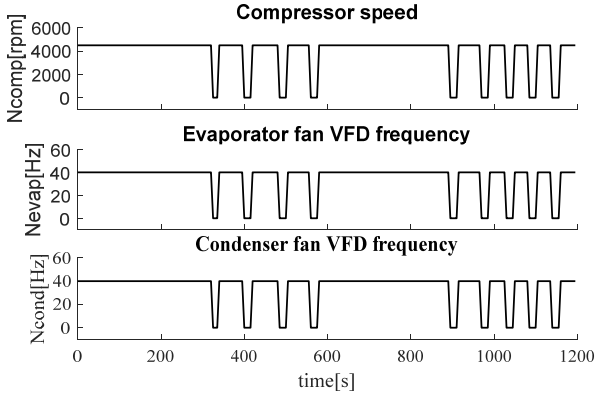

Figure 5.13 System inputs under case2

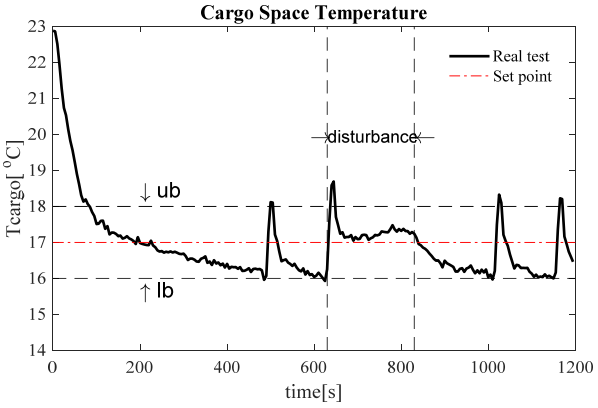

Figure 5.14 Controlled temperature under case3

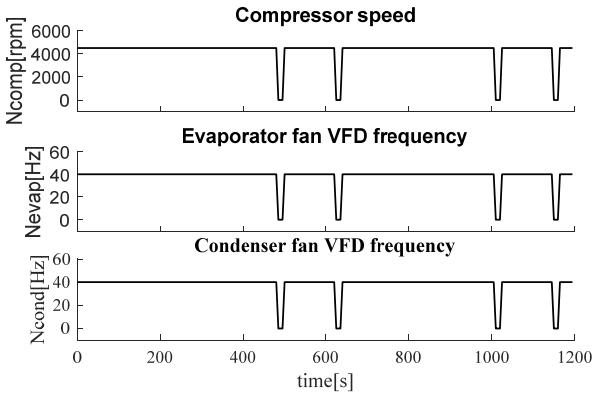

Figure 5.15 System inputs under case3

In Figure 5.10, Figure 5.12 and Figure 5.14 the temperature response under three cases is presented. The real temperature can reach the set points quickly and then fluctuate between the lower and upper bound with the system turning on and off. During the disturbed periods as indicated in dot-line regions, the compressor will be in the on mode for a longer time to balance the extra heating. The remaining figures show the system inputs during the test, which are switched between the maximum speeds to zero.

5.2.2 Set-point Controller

After some preliminary simulation tests, the controller is tuned and its parameters are finalized and provided in Table 5.3. The sampling time of this controller in the experiment is 1 s.

Table 5.3 controller gains and parameters

PI controller	*SMC*
$k_p = -1$	$\lambda = 0.01$
$k_i = -1$	$k = 0.18, \phi = 0.5$

The results obtained by the set-point controller under case 1 are presented from Figure 5.16 to Figure 5.18, which indicate that the controller can drive the temperature to its set point as quickly as the on/off controller. Due to its robustness, the SMC can maintain the temperature at the set point with much smaller oscillations than the on/off controller. Although the large disturbance around 200s exists, the controller can still keep the temperature around its set point. Figure 5.17 describes the system inputs, and Figure 5.18 shows pressure responses with respect to their set points. The set points of two pressures can be obtained according to the aforementioned method. Due to an additional heating load, the total load is changed, which affects the set point of the evaporator pressure instead of both. It should also be noted that although the compressor speed is controlled according to the cargo temperature instead of the evaporator pressure, the evaporator pressure can still approach and remain at its set point. That means the temperature trajectory is close to the optimal one in terms of power consumption. The same conclusions can be drawn from the other two cases shown in Figure 5.19~Figure 5.24.

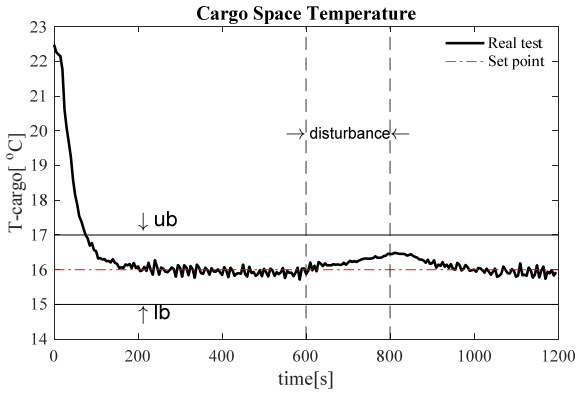

Figure 5.16 Controlled temperature under case1

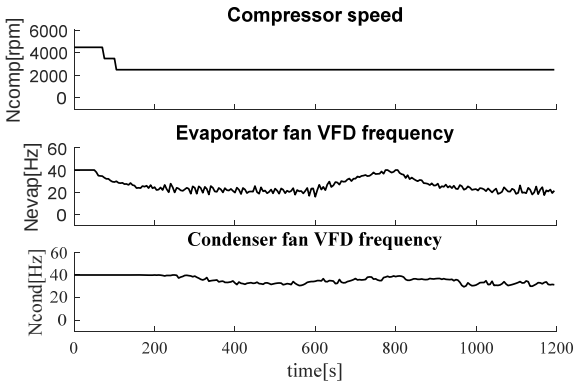

Figure 5.17 System inputs under case1

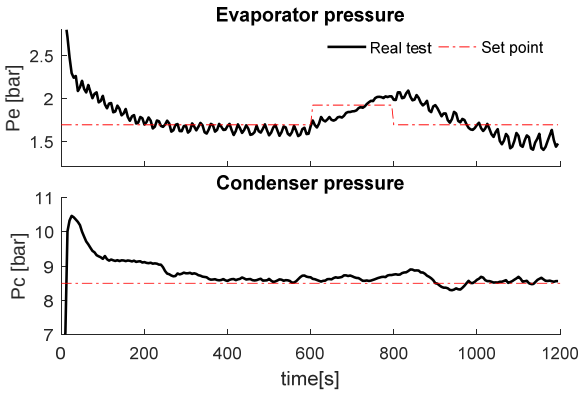

Figure 5.18 Pressures response under case1

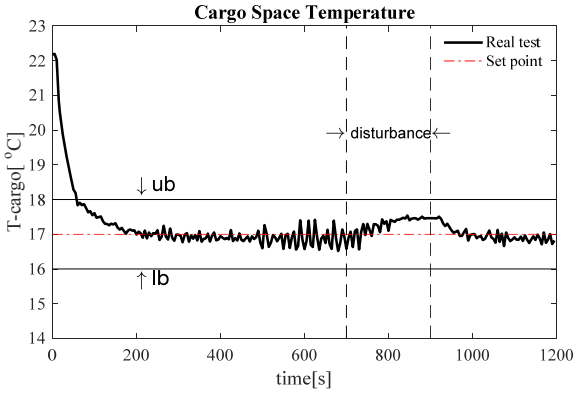

Figure 5.19 Controlled temperature under case2

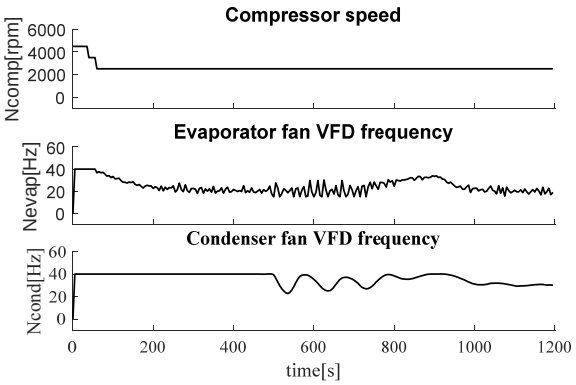

Figure 5.20 System inputs under case2

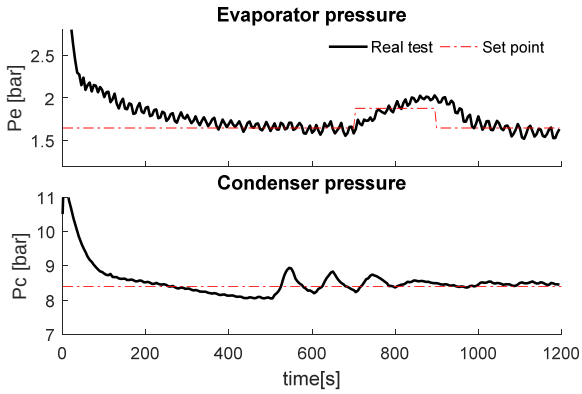

Figure 5.21 Pressures response under case2

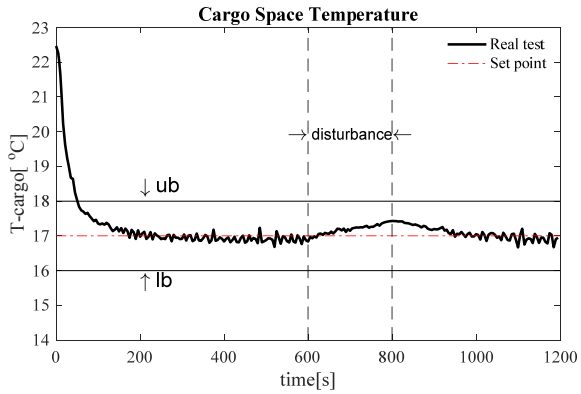

Figure 5.22 Controlled temperature under case3

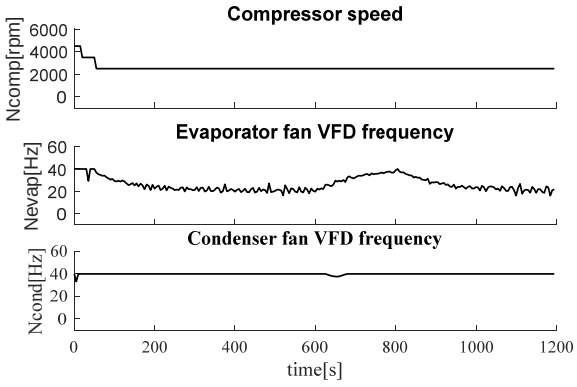

Figure 5.23 System inputs under case3

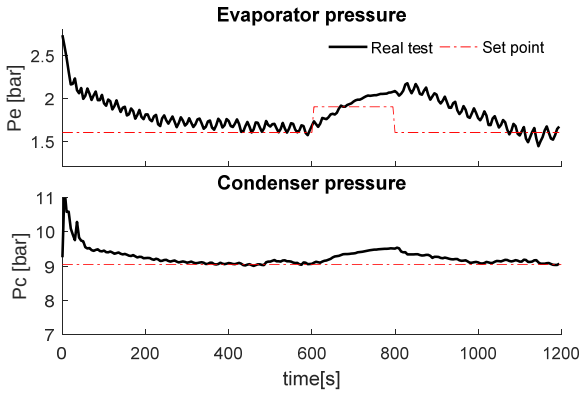

Figure 5.24 Pressures response under case2

5.2.3 Discrete Linear MPC

5.2.3.1 Controller Tuning

In this section, the controller parameters are briefly discussed and chosen. As the sample time T_s decreases, the ability to reject disturbance improves, but the computational effort increases dramatically to guarantee the real-time application. Thus, the best choice is a trade-off between robustness and computational effort based on the dynamics of the system [137]. The prediction horizon is related to the size of the quadratic optimization problem (the computational effort) and the accuracy of the prediction. A larger value leads to a better suboptimal solution with much more computational effort and increases the prediction's uncertainties. During the tuning process, N starts with a small value until further increase cannot bring obvious impact on the controller's performance. From Table 5.1, the scale factors of the three inputs and the output can be set as 2000, 40, 40 and 10, respectively. In order to ensure the value of each term in the objective function in the same scale, a larger Q is chosen. For the weight matrix R of the control effort, a larger weight is selected for the compressor speed—the most energy-consuming component; whereas, the remaining values are zeros. Usually, the larger input rate weights of S lead to more conservative control moves and produce a more robust performance [138]. By properly choosing a terminal weight from the Riccati equation, a finite-horizon MPC equivalent to an infinite-horizon linear quadratic regulator can be designed to achieve the close-loop stability of the plant [137, 138]. If the applications involve constraints, it is difficult to find such a time-varying terminal weight, and it usually needs a terminal constraint to force the plant states into a defined region at the end of horizon [138]. However, as per the tuning

guideline suggested in [139, 140], a sufficiently large value of the terminal weight can lead to a better closed-loop performance in most cases. The controller's parameters are presented in Table 5.4.

Table 5.4 MPC parameters

$T_s(s)$	N	Q	R	S	P
5	10	100000	$\begin{bmatrix} 5 & 0 & 0 \\ 0 & 0 & 0 \\ 0 & 0 & 0 \end{bmatrix}$	$\begin{bmatrix} 0 & 0 & 0 \\ 0 & 1000 & 0 \\ 0 & 0 & 1000 \end{bmatrix}$	$1000Q$

5.2.3.2 Results Presentation under Normal Conditions

Figure 5.25 to Figure 5.30 shows the results from the discrete MPC. It can be seen that it performs better than the on/off controller and similar with the set-point controller. For instance, the MPC controller can keep the temperature of the cargo in a smaller range, compared to ± 1℃ of the on/off controller. With the external disturbances up to 20% of the original heating load, the controller will optimally increase the cold air flow rate to balance the extra heating using the evaporator fan to maintain the closed-loop dynamics.

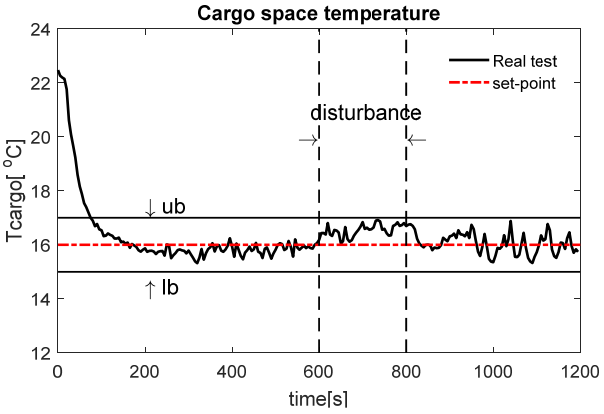

Figure 5.25 Controlled temperature under case1

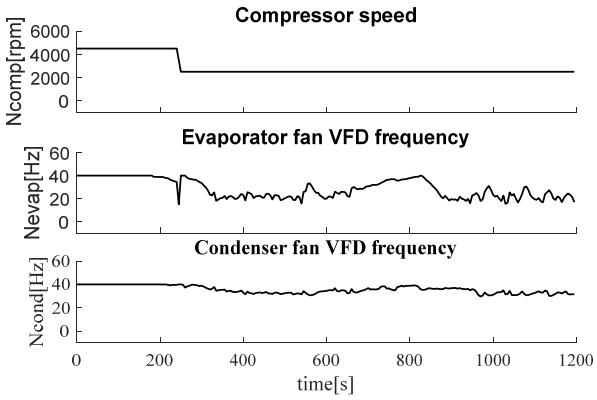

Figure 5.26 System inputs under case1

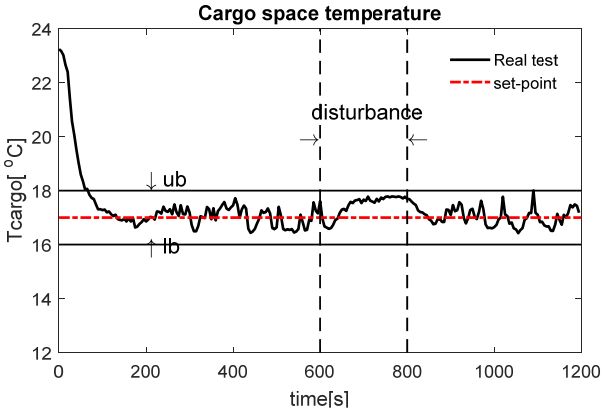

Figure 5.27 Controlled temperature under case2

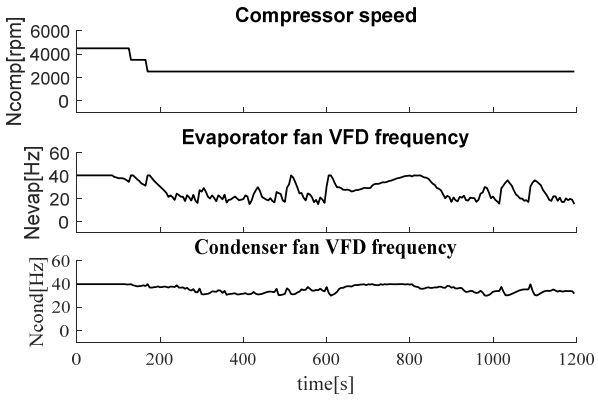

Figure 5.28 System inputs under case2

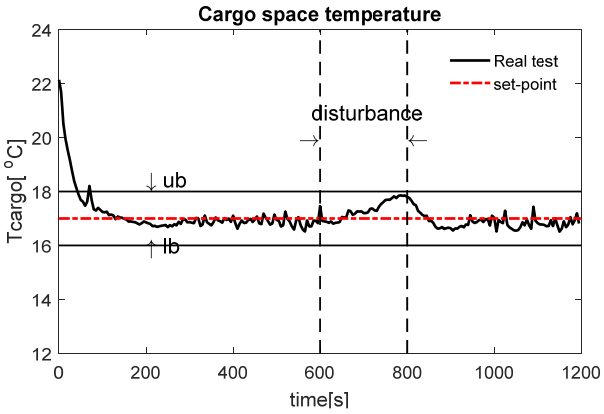

Figure 5.29 Controlled temperature under case3

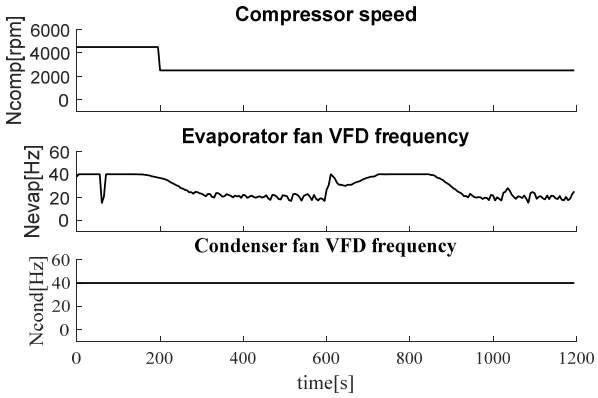

Figure 5.30 System inputs under case3

5.2.3.3 Results Presentation under Frosting Condition

As mentioned above, a large disturbance is added to the plant and the results show good performance of the proposed controller. As a common phenomenon of the A/C-R system, the frosting problem always exists [143]. When frost appears, it can cause model inaccuracies. For example, the refrigerant mass flow rate through the valve will decrease when the system is frosting, and accordingly, so do many other parameters such as pressures, temperature and superheat. In order to further demonstrate the robustness of the developed controller, the experimental results during the thermostatic expansion valve (TXV) frosting under two cases are presented. Figure 5.31 and Figure 5.32 show the TXV with and without frost.

Figure 5.31 TXV without frost

Figure 5.32 TXV with frost

In the first scenario, the ambient temperature is $25^{\circ}C$ and the temperature set point is $18^{\circ}C$; whereas, the ambient temperature is set at $30^{\circ}C$ with $16^{\circ}C$ set point in the second scenario. The temperature responses and system inputs are demonstrated in Figure 5.33 to Figure 5.36, respectively. It can be seen from the figures that the closed-loop performance of this proposed MPC is still satisfactory under both large external disturbances and frosting conditions.

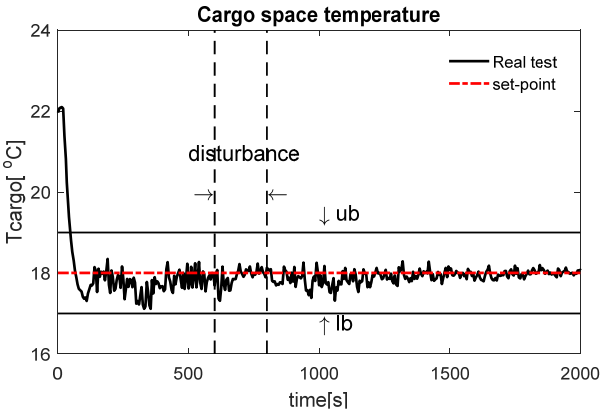

Figure 5.33 Temperature performance under the first scenario

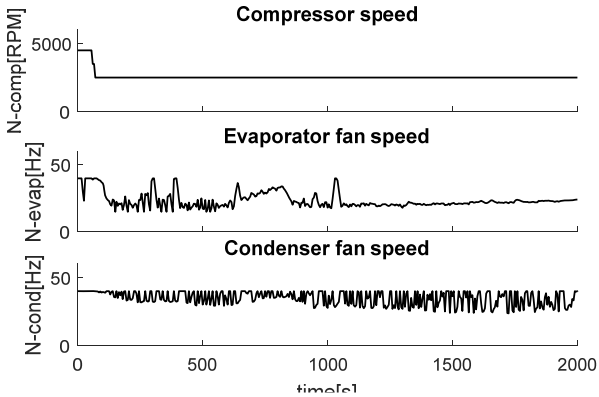

Figure 5.34 System inputs under the first scenario

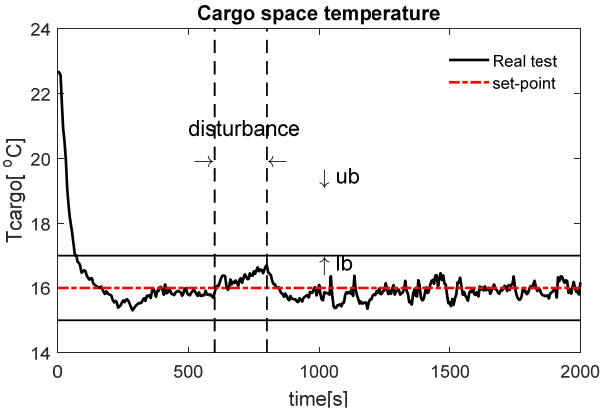

Figure 5.35 Temperature performance under second scenario

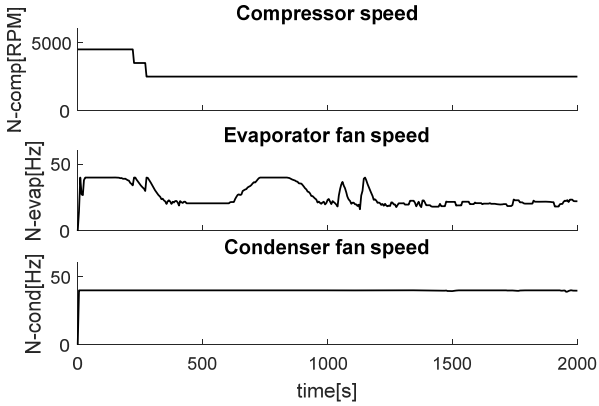

Figure 5.36 System inputs under second scenario

5.2.4 Result Comparison

The energy consumption for each controller under above cases is provided in the following table.

Table 5.5 Result comparison of controllers

	Case 1			***Case 2***			***Case 3***		
Controllers	On/off	Set-point	MPC	On/off	Set-point	MPC	On/off	Set-point	MPC
performance	Bad	good	good	bad	good	good	bad	good	good
EC	0.205	0.188	0.190	0.204	0.182	0.179	0.206	0.190	0.191
Improvement (%)	basis	8.29	7.31	basis	9.25	12.2	basis	7.76	7.28

EC: Energy consumption during 1200s experiment (kWh);

5.3 Case Study

In the previous section, the controller's performance and energy-saving benefits are studied under three specific cases, so in this section, the performance of all the controllers are simulated under a more realistic time-varying heating load condition. Table 5.6 shows the energy consumptions of the on/off controller and the discrete MPC under different heating loads. It can be seen that under higher heating load (above 0.5 kW) conditions, the discrete MPC consumes less energy than the on/off controller while for lower heating loads, the on/off controller is more efficient. Thus, it cannot be concluded that the discrete MPC is better than the on/off controller, rather than the discrete MPC could alleviate temperature fluctuations. That is why the other controllers appear in the following sections.

Table 5.6 Energy consumptions under different heating load conditions

Heating load (kW)	***Energy consumption for 1200s (kWh)***	
	On/off	***Discrete MPC***
0.8	*0.2311*	*0.2119*
0.7	*0.2162*	*0.1955*
0.6	*0.1895*	*0.1789*
0.5	*0.1671*	*0.1657*
0.4	*0.1451*	*0.1624*
0.3	*0.1179*	*0.1523*
0.2	*0.0925*	*0.1343*

5.3.1 Hybrid Controllers

By studying the energy consumptions under different heating load scenarios in Table 5.6, a direct hybrid controller could be intuitively designed by combining the discrete MPC and the on/off controller along with an identifier that could estimate the current heating load. The criterion for activating the discrete MPC is when the heating load is higher than 0.5 kW, and the on/off controller is activated in all other scenarios. Based on the experimental and simulated data, it is known that the cooling capacity produced by the system using the minimum compressor speed can balance the heating load under 0.5kW. In addition, the compressor is the most energy-consuming component in A/C-R system. As a result, the minimum compressor speed and maximum evaporator and condenser fan speeds are used in this on/off controller.

Even with these parameters, during a low heating load period, the on/off controller will switch the system frequently. In order to alleviate the effects of this phenomenon, an adaptive hybrid controller is given. The main idea is that the system starts working by using the discrete MPC until the controlled temperature settles down at its set point. Then, the MPC is still used unless the heating load is under 0.5 kW. Furthermore, the speed of the evaporator fan will be updated by:

$$N_{evap} = N_{evap-mpc} + k_{evap}\left(T_{evap-cham} - T_{setpoint}\right) \tag{5.11}$$

In this equation, $N_{evap-mpc}$ is the speed found by the discrete MPC at the switching point; k_{evap}, is a proportional coefficient and related to the switching frequency of the system when using on/off controller. When k_{evap} is zero, this hybrid controller will be the discrete MPC. Otherwise, when it is high enough, it will become the direct hybrid controller.

5.3.2 Continuous MPC

In some recent applications of the A/C-R system, the continuous variable components instead of components with several different speeds are employed. In order to study the potential of the MPC in these cases, a continuous MPC is designed based on the same model and procedures shown above. In this controller, the input of the compressor speed can continuously change from zero to its maximum speed.

5.3.3 Controllers Comparison

In order to compare the controllers discussed above, a heating load cycle is shown in Figure 5.37 is applied to the system for the simulations. This cycle is used to represent the heating load during a day

in 1200 seconds. As is well-known, the temperature at noon is higher than that in the morning and evening; as such, the heating load applied to the chamber reflects daily temperature variances. Although the heating load changes in a much lower frequency in the real situation, this cycle could also examine the robustness of the controllers.

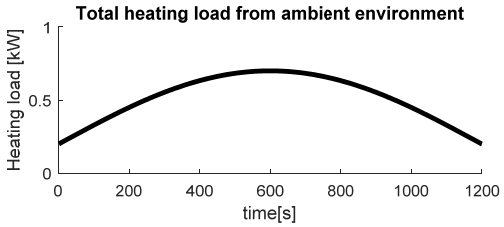

Figure 5.37 A heating load pattern

The controlled temperature behavior and total energy consumption are provided in Figure 5.38. The energy consumption will be also used as a basis of comparison for the following controllers. Figure 5.39 shows the system inputs of the on/off controller. The system stays on for a longer period of time under the large heating load condition and vice versa.

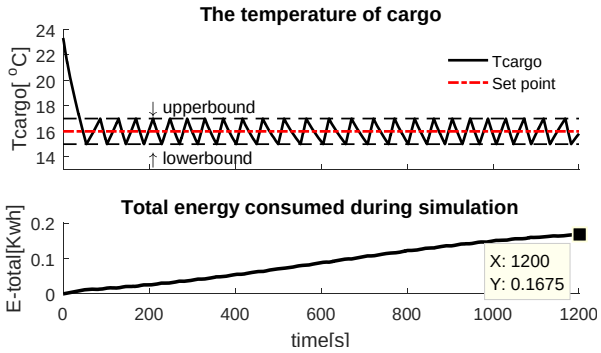

Figure 5.38 Temperature performance and energy consumption

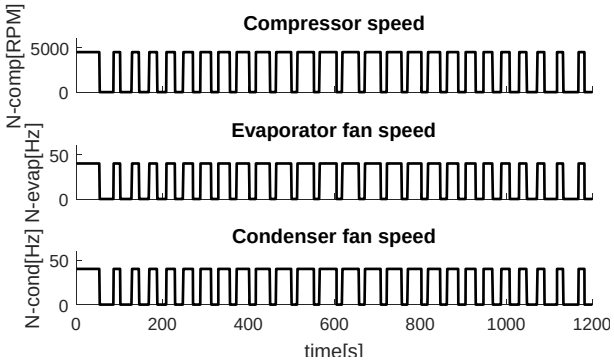

Figure 5.39 System inputs of on/off controller

The results of the discrete MPC are provided by Figure 5.40 and Figure 5.41.

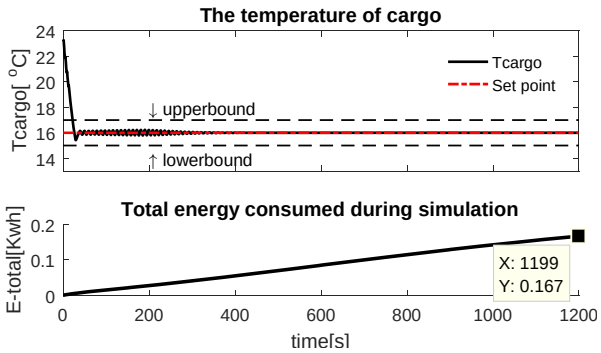

Figure 5.40 Temperature performance and energy consumption

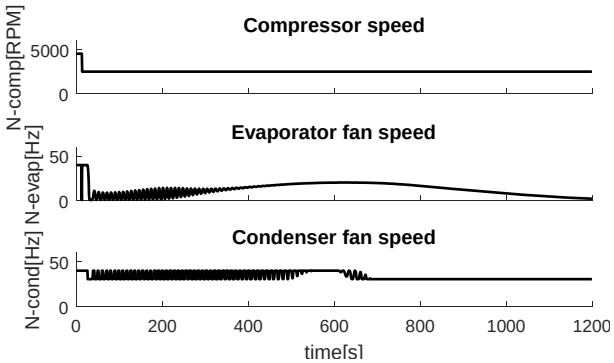

Figure 5.41 System inputs of discrete MPC

The results of the direct hybrid controller are presented in following two figures. It can be seen that the on/off controller and the discrete MPC are alternated when the heating load is 0.5 kW.

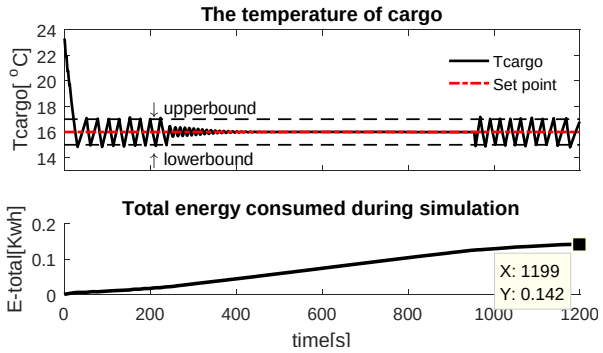

Figure 5.42 Temperature performance and energy consumption

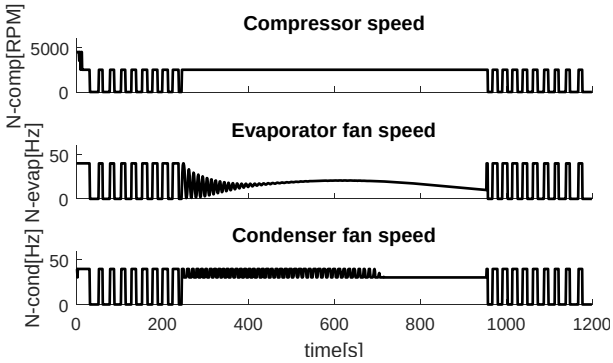

Figure 5.43 System inputs of discrete MPC

By choosing 1 as the value of k_{evap} the results of the adaptive hybrid controller are shown as follow. In comparison to the direct hybrid controller, a lower activation frequency of the system is obtained at the expense of energy consumption. As a result, a trade-off performance between energy consumption and switching frequency can be obtained by using the desired value of k_{evap} .

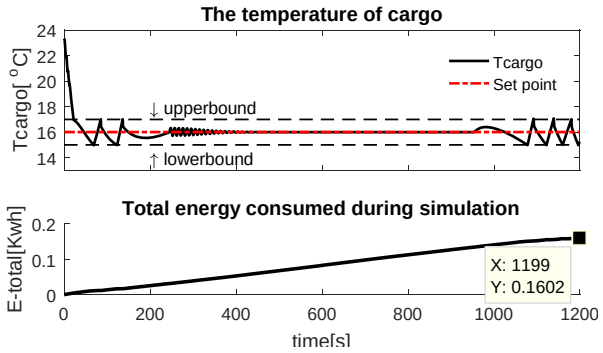

Figure 5.44 Temperature performance and energy consumption

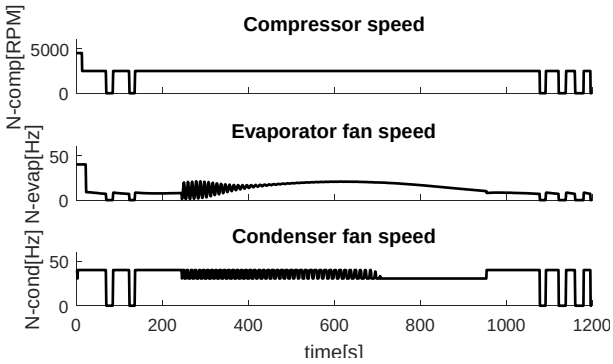

Figure 5.45 System inputs of adaptive hybrid controller

The controlled temperature performance and energy consumption of the continuous MPC are demonstrated as follows. In Figure 5.47, the compressor speed can be manipulated freely according to the changing heating load instead of alternating between several discrete values.

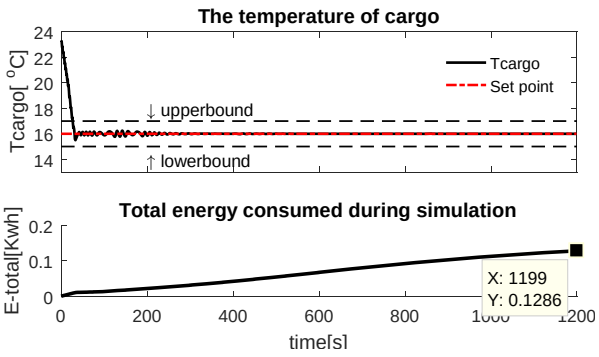

Figure 5.46 Temperature performance and energy consumption

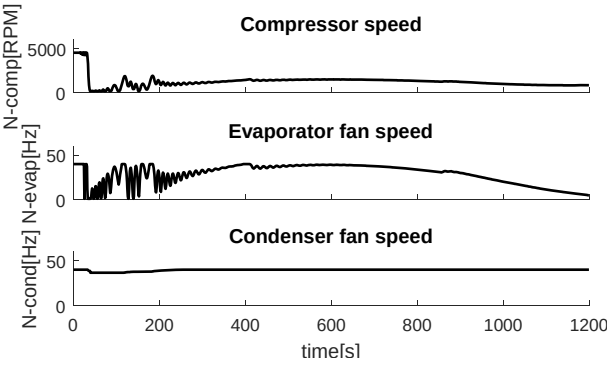

Figure 5.47 System inputs of continuous MPC

5.3.4 Results Analysis

All the above simulations are done under the same working conditions but with the new heating load cycle shown in Figure 5.37. The total energy consumption and improvements of the proposed controllers with respect to the conventional on/off controller are listed in Table 5.7.

Table 5.7 Energy consumptions of different controllers

Controllers	*Energy consumption 1200s (kWh)*	*Improvement (%)*
On/off	*0.1675*	*Basis*
Discrete MPC	*0.1670*	*0.24*
Direct hybrid	*0.1420*	*15.17*
Adaptive hybrid	*0.1602*	*4.30*
Continuous MPC	*0.1286*	*23.18*

Regarding the energy consumption, the two hybrid controllers are able to save more than both the on/off and discrete MPC. A more desired performance can be obtained by choosing a proper coefficient k_{evap} , by balancing two aspects: the switching frequency and energy consumption. Obviously, after introducing the continuous MPC to the A/C-R system with continuously variable compressors, the continuous MPC helps the A/C-R system with a continuously variable compressor save 23% energy because all the inputs can work coordinately to achieve the energy-saving objective.

5.4 Summary

This chapter was aimed at developing the most energy-saving controllers for automotive A/C-R systems. Before developing the controllers, a simplified control-based model was developed and

validated. Based on this model, all the controllers were built and simulated under the same working conditions.

The comparison of experimental results showed that the set-point controller and the discrete MPC could satisfy the objectives of the A/C-R system. Due to the high nonlinear and MIMO nature of the system, the *PI* controller in the set-point controller may deteriorate its performance when working conditions would change fast. However, it is computationally costless and could be easy to implement. The discrete MPC is an optimal controller, mostly suitable for complex, multivariable, and nonlinear plants. The energy consumption term was included in the objective function when this discrete MPC was designed, which was also applicable to the real system. All of these attributes differentiate this study from others in the literature. Therefore, the MPC is a promising controller for A/C-R systems with continuously variable components, and the hybrid MPCs can be the best choices for A/C-R systems with discrete variable components.

Chapter 6
Power Management Control Systems for RAPS

In this chapter, several power management controllers are designed for RAPS with different levels of access to the future drive cycles. In these controllers, a regenerative braking controller is also developed to ensure maximum energy recovery during vehicle braking.

6.1 Regenerative Braking Controller Development

Regenerative braking, as an important characteristic of HEVs and EVs, refers to a process in which the kinetic energy of the vehicle can be converted by a motor/generator into electrical energy when vehicle braking. The recovered energy can be used immediately or stored in the vehicle's batteries or supercapacitors until needed. In this way, regenerative braking is able to extend the driving range to a great extent, about 8-25% [144] by recovering otherwise wasted energy, which is more obvious in stop-and-go-featured urban driving [145]. However, the amount of recaptured energy depends on many factors such as the amount of kinematic energy of the vehicle, the driver's braking demand, the friction limit provided by the road, SoC of the ESS, the charging rate and the power limit of the generator.

In practice, the regenerative braking should cooperate with the conventional friction braking in order to provide the satisfactory braking demand from the drivers. On one hand, there is a limitation to the maximum braking torque that the motor is capable of providing. On the other hand, the friction braking is necessary for a complete stop of a vehicle because the produced regenerative torque at low vehicle speeds is too small to stop a vehicle. In short, the regenerative braking and the friction braking have to co-exist in a vehicle.

6.1.1 Braking Force Allocation between Mechanical and Electric

As discussed above, in order to satisfy the driver's demand on braking requirement, it is necessary for the regenerative braking system to coexist with the friction braking system. Usually, the regenerative braking system is located at the driven axle [146] and controlled electronically, and an apparent control purpose is to capture the kinetic energy during vehicle braking as maximum as possible. No doubt this purpose shall be achieved by meeting the braking demand and without affecting the drivability of the vehicle. Therefore, it is a challenge to manage well the relationship between the friction braking and the regenerative braking. Currently, many control strategies have been developed

to make these two braking systems work properly and efficiently, and they can be classified into two categories: parallel and series braking systems.

6.1.1.1 Parallel Braking System

In a parallel braking system, the electric braking and mechanical braking take place simultaneously; whereas in the conventional friction braking system, the ratio of braking force allocation between the front and rear axle is established in advance. However, the regenerative braking system can add additional braking force to the axle which it is applied to, and this enables the regenerative braking system to be applied to a vehicle equipped only with a conventional braking system. Since the friction braking forces are distributed in a fixed way, the parallel braking system can work without a controller. The electric braking forces can be controlled according to the measurements from a pressure sensor in the hydraulic unit or a position sensor in the braking pedal. Thus, this makes the implementation of a parallel braking system relatively simple. Nevertheless, a parallel braking system has less potential for recovering energy than its counterpart [144, 147].

6.1.1.2 Series Braking System

In contrast, in a series braking system the optimal distribution between the regenerative braking and the friction braking can be realized under the assist of a controller. Braking can be applied solely by the regenerative braking system, provided that the braking needed is no more than the maximum braking torque that the electric motor is capable of producing and the road adhesion permits. Thanks to the optimal allocation of the braking forces and the possibility of having the additional degrees of freedom, series braking systems are usually able to recover more energy than parallel braking systems. In addition, their better braking blending makes drivers have an enhanced perception of the pedal feel [144].

The distribution strategy of the braking forces between the front and rear axle is vitally important and usually designed on the basis of the Ideal Braking Force Distribution (IBFD) curve. This curve indicates that the front and rear wheels will lock simultaneously when the braking forces reach the limit that the tire-ground adhesive allows. In this section, for the sake of simplicity, the IBFD curve is also utilized. The regenerative braking controller aims to maximize the recovered energy without affecting the drivability of the vehicle. Therefore, the series one is utilized, where the friction braking only assists the regenerative braking. Then the following rules are used for the regenerative braking torque to maximize the recovered energy. 1), when the required braking force is less than the friction

force supported by the road, the regenerative braking force equals the minimum value of the power compactly of the generator and the one calculated by the SoC constraints to avoid the battery being overcharged; 2), when the required one is large than the maximum friction allowed by the road, the regeneration braking force will equal to the smaller one between the maximum friction and the generator power limit; 3), in other cases, the friction one will be activated, for example, when there is a sharply braking, or the braking happens in an extremely short time, the friction braking is activated due to the recharging rate limit; and, when the braking happens in an extremely slow vehicle speed due to the generator power limit.

6.2 MPC-based PMS Development for RAPS

In this section, several new MPC-based PMSs with different level of access to the future drive cycle are designed, which are different from the existing ones in current literature.

6.2.1 Known Drive Cycles

Service vehicles, such as delivery trucks or public buses, usually have predetermined routes, thus, it is possible and beneficial to utilize an MPC strategy to improve the fuel economy of RAPS. However, the mass/load of such service vehicles is time-varying during a drive cycle. Therefore, an adaptive MPC should be designed to account for this variation. Although the drive cycle is preset, it would experience uncertainties or disturbances caused by traffic or weather conditions in real situations. To deal with this problem, a large step size prediction method is used in the adaptive MPC to enhance its robustness. The proposed adaptive MPC is compared with a prescient MPC in different scenarios to demonstrate its applicability and optimality. The proposed approach is independent of the powertrain topology such that it can be directly extended to other types of hybrid electric vehicles.

6.2.1.1 Vehicle Mass Identification

For the sake of completeness, in the following a method for estimating the vehicle mass using a Kalman filter is discussed [128]. Generally, Kalman filter is used as a state observer. However, the parameter identification problem can be formulated in the state space form. To apply the Kalman filter, the first step is to form a parametric model by the component model presented in Chapter 3 in the form of:

$$\begin{cases} z = \theta(k)\phi(k) = \left(T_{eng} - T_{eng\to alt}\right)\dfrac{N_{tf}\eta_{tran}}{R} - \dfrac{1}{2}\rho C_D A_f V_{veh}^2 \\ \theta(k) = M \\ \phi(k) = C_r g\cos\alpha + g\sin\alpha + a \end{cases} \tag{6.1}$$

where z is the process output, θ represents the actual values of the parameters, and ϕ is the regression vector. The engine torque $\left(T_{eng}\right)$, vehicle speed $\left(V_{veh}\right)$, and engine speed $\left(\omega_{eng}\right)$ are the signals available through the vehicle control area network (CAN). The torque $\left(T_{eng\to alt}\right)$ from engine to the alternator can be calculated by the system control input $\left(P_{eng\to alt}\right)$. The acceleration signal is provided by the vehicle accelerometer, and in a case that this signal is not available, it can be obtained from the vehicle speed. By comparing engine speed and vehicle speed, combined ratio of the transmission and final drive $\left(N_{tf}\right)$ can be calculated. Moreover, road grade (α) is assumed to be provided by a GPS receiver. The efficiency of driveline (η_{tran}), rolling resistance coefficient $\left(C_r\right)$, mass density of the air (ρ), coefficient of aerodynamic resistance $\left(C_D\right)$, and frontal area of the vehicle $\left(A_f\right)$ are assumed to be known and constant with respect to time. The only unknown parameters will then be the vehicle mass $\left(M\right)$, which need to be estimated. The goal of the estimation method is to find the model output $\left(\hat{z}\right)$ that best approximates the process output $\left(z\right)$. At each step, the estimation of the parameters is updated by:

$$\hat{\theta}(k) = \hat{\theta}(k-1) + K(k)e(k) \tag{6.2}$$

where, $\hat{\theta}$ represents the estimated values of the parameters, and e is the estimation error which reflects the difference between the process and the model outputs:

$$e(k) = z(k) - \hat{z}(k) \tag{6.3}$$

Also, K is the Kalman gain which is calculated by:

$$\begin{cases} K(k) = \dfrac{P(k-1)\phi(k)}{R_2 + \phi^T(k)P(k-1)\phi(k)} \\ P(k) = P(k-1) + R_1 - K(k)\phi^T(k)P(k-1) \end{cases} \tag{6.4}$$

where, $P(k)$ is the estimation error covariance; R_1 and R_2 represent the covariance matrices of the process and the measurement noise. The diagonal entries of R_1 should be chosen based on how fast

the corresponding parameter changes with respect to time. Therefore, if a parameter is known to change quickly, the corresponding entry in R_1 should be large and vice versa.

When there is no process noise (*i.e.* $R_1 = 0, R_2 = 1$), the above Kalman filter parameter identification algorithm is equivalent to the recursive lease square method. However, due to its ability to recursively calculate the parameters by combining prior knowledge, predictions from system models and noisy measurements, the Kalman filter based parameter identification algorithm is utilized in this study [148].

6.2.1.2 Model Predictive Control Strategy Development

As an optimal control method, the MPC originated in the chemistry industry's control techniques. It is characterized by slow dynamics, which provides enough time for optimization calculations [114]. As mentioned above, the RAPS with the slow battery SoC dynamics makes it suitable for an MPC application. The objective function is shown below,

$$\begin{aligned} J(x_0, u_0) &= \left(y(N) - y_{ref}\right)^T P\left(y(N) - y_{ref}\right) + \\ &\sum_{k=0}^{N-1}\left[\left(y(k) - y_{ref}\right)^T Q\left(y(k) - y_{ref}\right) + \left(\frac{u(k)}{\eta(k)}\right)^T R\left(\frac{u(k)}{\eta(k)}\right)\right] \end{aligned} \tag{6.5}$$

$s.t.$

$$y_{min} \le y(k) \le y_{max}, \quad k = 0, \ldots N-1$$

$$u_{min} \le u(k) \le u_{max}, \quad k = 0, \ldots N-1$$

where, the first term on the right-hand side is the terminal cost; the second term is the summation of the stage cost and the extra FC to charge the battery; it can guarantee the direct charging happening in high engine efficiency periods by introducing this form. P, Q and R are normalized weights to balance each term. The objective function is transferred into a quadratic form with respect to the control input. As the prediction horizon length is N, the trajectory of future states will be obtained by the discrete-time model:

$$\underbrace{\begin{bmatrix} x(k+1) \\ x(k+2) \\ \vdots \\ x(k+N) \end{bmatrix}}_{\bar{X}} = \underbrace{\begin{bmatrix} A \\ A^2 \\ \vdots \\ A^N \end{bmatrix}}_{S^x} x(k) + \underbrace{\begin{bmatrix} B_u & 0 & \dots & 0 \\ AB_u & B_u & \dots & 0 \\ \vdots & \vdots & \ddots & 0 \\ A^{N-1}Bu & A^{N-2}B_u & \dots & B_u \end{bmatrix}}_{S^u} \underbrace{\begin{bmatrix} u(k) \\ u(k+1) \\ \vdots \\ u(k+N-1) \end{bmatrix}}_{\bar{U}}$$
$$+ \underbrace{\begin{bmatrix} B_v(k) \\ B_v(k) + B_v(k+1) \\ \vdots \\ B_v(k) + B_v(k+1) + \cdots B_v(k+N-1) \end{bmatrix}}_{\bar{V}} \tag{6.6}$$

$$\underbrace{\begin{bmatrix} y(k+1) \\ y(k+2) \\ \vdots \\ y(k+N) \end{bmatrix}}_{\bar{Y}} = \underbrace{\begin{bmatrix} C & 0 & 0 & 0 \\ 0 & C & 0 & 0 \\ 0 & 0 & \ddots & 0 \\ 0 & 0 & 0 & C \end{bmatrix}}_{C^x} \bar{X}$$

The convex quadratic objective function only with respect to the input will be obtained by inserting Equation (6.6) into the original objective function shown in Equation (6.5) and neglecting the constant term:

$$J(x_0, u_0) = \frac{1}{2}\bar{U}^T H \bar{U} + \bar{U}^T g$$

$$H = 2\left(C^x S^u\right)^T \bar{Q}\left(C^x S^u\right) + \left(1/\eta\right)^T \bar{R}\left(1/\eta\right), \quad g = 2\left(C^x S^u\right)^T \bar{Q}\left(C^x S^u - \bar{Y}_{ref}\right)$$

$$s.t. \tag{6.7}$$

$$\bar{U} \geq max\left(\bar{U}_{min}(U), \bar{U}_{min}(\bar{U}), \bar{U}_{min}(X)\right)$$

$$\bar{U} \leq min\left(\bar{U}_{max}(U), \bar{U}_{max}(\bar{U}), \bar{U}_{max}(X)\right)$$

where the Hessian matrix (H) is symmetric and positive or semi-positive definite and g is the gradient vector. $\bar{Q}, \bar{R}$ and $\bar{X}_{ref}$ should be reformulated based on Q, R and X_{ref}. The updated constraints of the control can be found by the reformulation of Equation (6.6) and the constraints shown in Equation (6.5).

Figure 6.1 shows the predefined or the nominal drive cycle of a service vehicle as well as the real world drive cycle. Due to the aforementioned factors, the real drive cycle cannot exactly coincide with the predefined one but locate around it. The real drive cycle in the next future seconds is not known as a priori in real situations. The only information can be utilized is the nominal drive cycle. If the prediction step size (distance between two prediction points) is extended to a large value when

implementing the MPC strategy, on the one hand, the effects on state prediction of both drive cycles are similar, because both the positive and negative deviations around the nominal one will counteract each other's effects; on the other hand, more future information will be included into the MPC development such that the solutions will be closer to the global optimal ones without adding any extra computational costs. In order to demonstrate the benefits introduced by the proposed MPC, the prediction step size of 10 seconds is chosen. That means the states are calculated every 10 seconds by Equation (6.6), and then use the new output trajectory shown in Equation (6.8) for quadratic problem (QP) formulation.

$$\underbrace{\begin{bmatrix} y(k+10) \\ y(k+20) \\ \vdots \\ y(k+N*10) \end{bmatrix}}_{\bar{Y}} = \underbrace{\begin{bmatrix} C & 0 & 0 & 0 \\ 0 & C & 0 & 0 \\ 0 & 0 & \ddots & 0 \\ 0 & 0 & 0 & C \end{bmatrix}}_{C^x} \begin{bmatrix} x(k+10) \\ x(k+20) \\ \vdots \\ x(k+N*10) \end{bmatrix} \tag{6.8}$$

However, the first element of the optimal solutions will be applied to the system for 1 second, and then the MPC uses the fresh data to move forward.

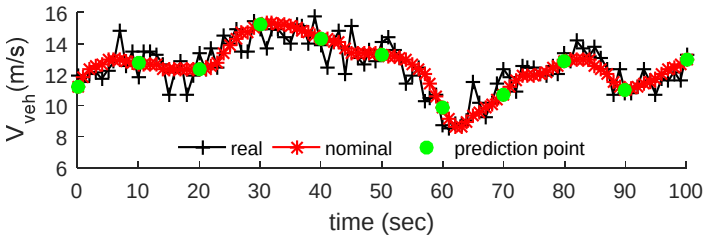

Figure 6.1 Drive cycles and prediction points of the proposed MPC

6.2.1.3 Service Cycle

The service cycle is defined as the power consumed by the auxiliary devices of the service vehicle. As the main auxiliary device, the power consumption of the A/C-R system is varying with the ambient and operating conditions of service vehicles. Figure 6.2 shows the ambient temperature and the HL applied to the cargo in a typical summer morning from 10:00 am to 12:30 pm. For simplicity, the HL is assumed to be proportional to the temperature difference.

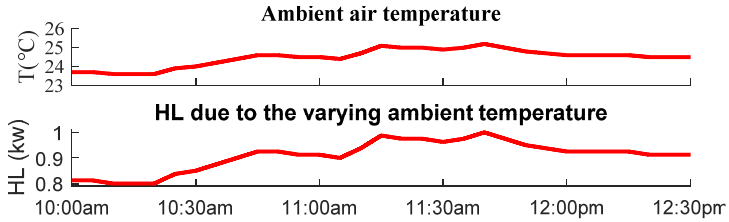

Figure 6.2 The ambient temperature and corresponding HL

In addition, some extra HL exists during the periods of loading and unloading due to door open. Note that during these periods, the goods are assumed to be moved uniformly. The extra heating is roughly assumed to be 0.1 kW as shown in Figure 6.3, where the total HL load from the outside is calculated [36]. For the sake of simplicity, the cooling capacity produced by the A/C-R system is only used to balance the total HL to maintain the desired temperature, and the ratio of cooling capacity to the power consumed by the A/C-R system is assumed to be 1.

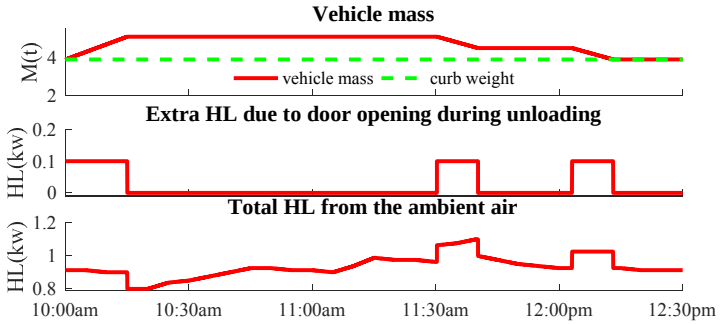

Figure 6.3 Vehicle mass, extra HL, and total HL

6.2.1.4 Drive Cycle

The nominal drive cycle is created based on the segment information provided in the first column of Table 6.1.

Table 6.1 drive cycles

Nominal		Scenario 1	Scenario 2
Segment	Duration (s)		Segment
Loading	900	Nominal + disturbance	Unloading
FTP75	1874		FTP75
HWFET	765		HWFET
FTP75	1874		UDDS
Unloading	600		Unloading
UDDS	1370		FTP75
Unloading	600		Unloading
UDDS	1017		UDDS

Switch the orders of two segments + disturbance

Two kinds of disturbances will be added onto the nominal drive cycle to simulate the real-world ones. In scenario 1, about 15% white noise is added, whereas the orders of two segments are switched to form the drive cycle in scenario 2. The drive cycles of 2.5 hours are visualized in Figure 6.4, where the middle figure shows the amplified vehicle velocity around 10:30 am.

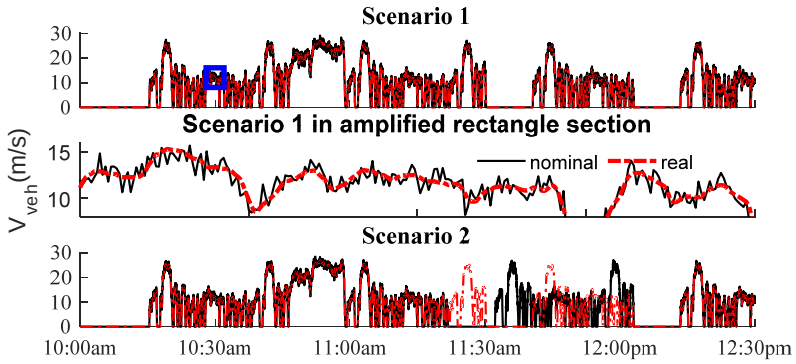

Figure 6.4 Drive cycles under two scenarios

6.2.1.5 Drive Cycle and Service Cycle Analysis

In this research, our target vehicle is GMC SAVANA 2500, whose specification can be obtained in [149]. Take the UDDS drive cycle as an instance, according to Equation (3.1), the vehicle power can be calculated and shown in Figure 6.5, where only the power for driving the vehicle and its average value are presented.

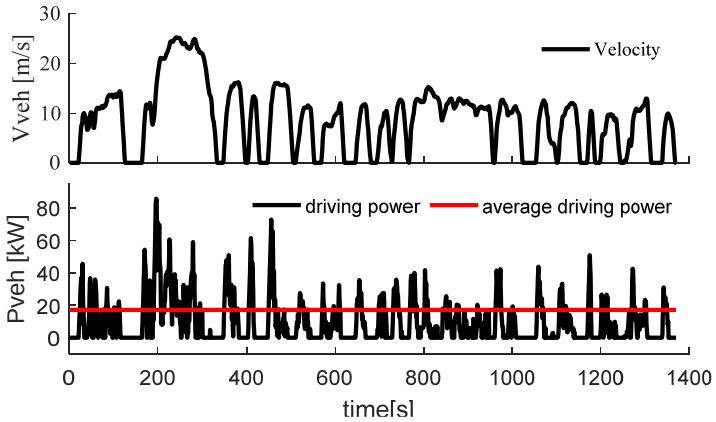

Figure 6.5 Drive cycles of UDDS and vehicle power

From Figure 6.3, it can be seen that the maximum auxiliary power is 1.1 kW. Compared to the driving power of the vehicle, the auxiliary power is relatively small. Thus, this type of vehicle refers to the light service vehicle, and the average driving power and auxiliary power are presented in Table 6.2.

Table 6.2 Driving power and auxiliary power

Drive cycle	UDDS	The proposed drive cycle
Average driving (auxiliary) power (kW)	17.15(0.9)	21.53(0.9)

6.2.1.6 MPCs Configuration and Results Analysis

After the drive cycles and service cycle are defined, the known information will be input to the MPC and used to find the optimal solution of the problems [150]. In this section, MPC^1 is the prescient one with the full knowledge of the real drive cycle, whereas MPC^2 only knows the nominal drive cycle or the measured drive cycle information in next several seconds. The parameters of the MPCs are provided in Table 6.3.

Table 6.3 MPC Parameters

Parameters	$T_s\,(\mathrm{sec})$	N	Q	P	R	y_{ref}
Value	10/1	10	$\begin{bmatrix} 0.5 & 0 \\ 0 & 1 \end{bmatrix}$	10Q	1	$\begin{bmatrix} 0.9 \\ 0 \end{bmatrix}$

In order to protect and elongate the lifespan of the battery, the SoC should not be drained and reach its limits to pursue high overall efficiency [117]. In addition, the battery will be used to power the A/C-R system and reduce idling, so the SoC should maintain a high level during the vehicle in travel. Therefore, the SoC reference 0.9 is chosen and a relatively small weight 0.5 is used to avoid it deviating from the reference too far. The prediction horizontal length N should not be too large or small to balance the prediction accuracy and optimality. A ten-time larger terminal weight is chosen to enhance the stability of the controllers. The QP is solved by an open source solver, which can solve the QP in milliseconds and guarantee its real-time applicability [136].

The results of the system input, SoC, and vehicle mass estimation are presented in the following figures. The results in both scenarios show that MPC^1 uses less power to charge the battery resulting into a less FC. Although MPC^2 uses the nominal drive cycle to predict the future response of the system, it still can have a similar performance with MPC^1 both in final SoC and FC. However, the MPC with a large step size has a better performance because a large step size can make MPC predict further, eliminate the influence of the disturbance and response much earlier to achieve more optimal performance. The Kalman filter can correctly identify the mass in both scenarios except the periods when the vehicle stops. When the vehicle starts to move, the estimator can reach the real vehicle mass quickly and accurately.

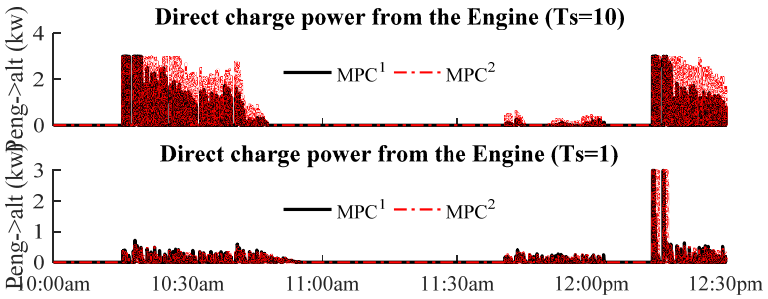

Figure 6.6 System inputs under scenario 1

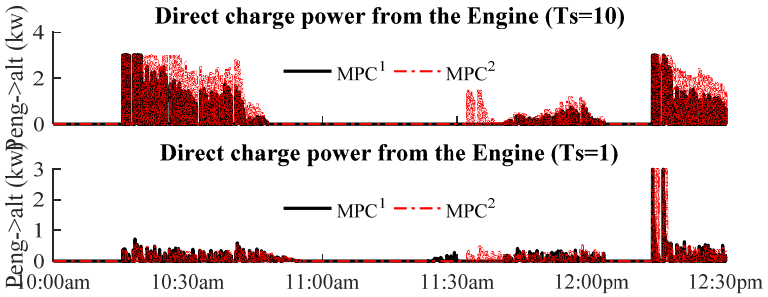

Figure 6.7 System inputs under scenario 2

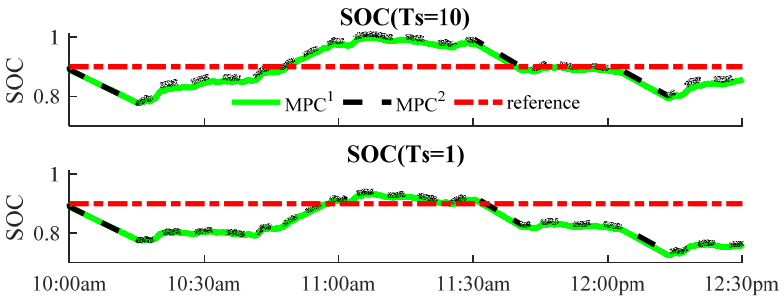

Figure 6.8 SoC responses under scenario 1

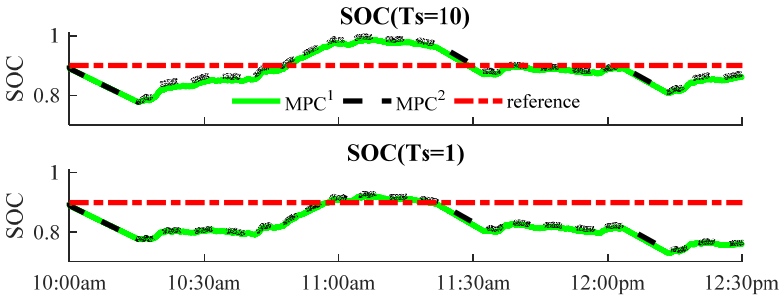

Figure 6.9 SoC responses under scenario 2

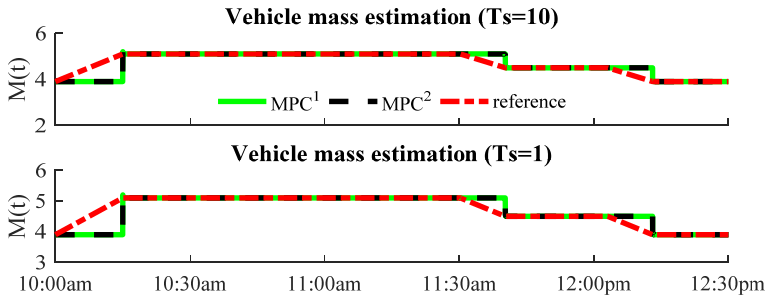

Figure 6.10 Vehicle mass estimation under scenario 1

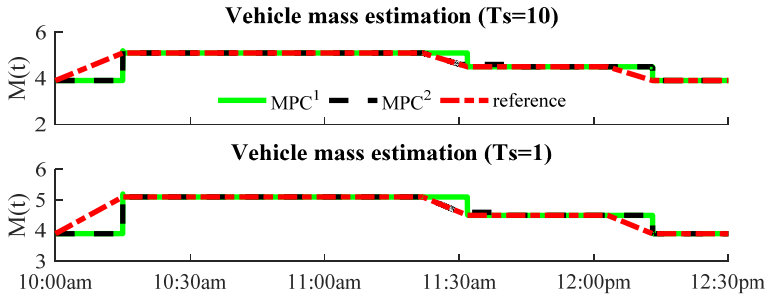

Figure 6.11 Vehicle mass estimation under scenario 2

Table 6.4 provides the results of the final SoC and the FC. In order to eliminate the effects of the deviation of the final SoCs on the FC, an SoC-correction approach [151] is used. The total FC (19.7L) of the vehicle without RAPS is provided as a basis to compare with. Meanwhile, the FC (18.14L) just used for driving vehicle instead of both vehicle and difference is FC for powering A/C-R system. Under scenario 1, fuel savings are more than 7 percent after RAPS is introduced to the conventional service vehicle in column Save[1]. In addition, the MPCs with 10 seconds step size save more than the ones with shorter step size. In this study, the average power (1kW) of A/C-R system is relatively smaller compared to vehicle power. These vehicles are called light service vehicle. However, for heavy service vehicles, they can witness more fuel saving using the RAPS. Regarding the FC2 and Save2, the FC of the A/C-R system in the conventional vehicle is 1.56 L, whereas the FC in the systems with RAPS is just 9 times less. Scenario 2 shows a similar characteristic. However, the drive cycle used for prediction is more different than the real one, thus, the savings are a little bit less than scenario 1. It means the performance of the proposed MPC was not affected by such large disturbances and its robustness is verified.

Table 6.4 Result comparison of Two Scenarios

Systems		Scenario 1					Scenario 2				
		Final SoC	FC[1] (L)	Save[1] (%)	FC[2] (L)	Save[2] (%)	Final SoC	FC[1] (L)	Save[1] (%)	FC[2] (L)	Save[2] (%)
Without RAPS		N/A	19.7	basis	1.56	basis	N/A	19.7	basis	1.56	basis
With RAPS	MPC[1] $(T_s = 10)$	0.8649	18.273	7.24	0.133	91.46	0.8722	18.279	7.21	0.139	91.05
	MPC[2] $(T_s = 10)$	0.8782	18.277	7.22	0.137	91.19	0.8817	18.309	7.06	0.169	89.14
	MPC[1] $(T_s = 1)$	0.7689	18.302	7.09	0.162	89.58	0.7708	18.308	7.07	0.168	89.26
	MPC[2] $(T_s = 1)$	0.7756	18.31	7.06	0.17	89.13	0.7756	18.412	6.54	0.272	82.53
Vehicle		N/A	18.14	N/A	N/A	N/A	N/A	18.14	N/A	N/A	N/A

FC[1]: total FC; FC[2]: FC of A/C-R system; Save[1]: fuel saving percentage due to RAPS; Save[2]: fuel saving percentage of A/C-R system;

Note: the above results are obtained based on a light service vehicle with only 10% braking power can be captured via a serpentine belt. For the heavy service vehicle with a PTO configuration, more fuel saving will be witnessed by recovering more braking power.

6.2.2 Unknown Drive Cycles

This section presents a model predictive PMS for RAPS used in service vehicles, which do not know the future drive information *a priori*. As an optimization-based approach, the MPC usually requires the drive cycle or the drivers' command to be known a priori. However, in this study, an average concept based MPC is developed without such knowledge. The analysis shows that the RAPS with the proposed MPC saves fuel consumption. Meanwhile, the average concept based MPC has a similar performance as the prescient MPC. In addition, the robustness of this MPC is also tested under other drive cycles. The proposed MPC is independent of powertrain topology such that it can be directly extended to other types of HEVs, and it provides a way to apply the MPC even though the future driving information is unavailable [152].

6.2.2.1 Driving Information Estimation

In this section, the future driving information required by the MPC is estimated by the proposed approach. Take the urban dynamometer driving schedule (UDDS) as an example. Figure 6.12 shows

the velocity, acceleration, and vehicle power calculated by Equation (1) during the first 1200s. The positive power represents the power needed to drive the vehicle; whereas, the negative power represents the available regenerative power, which can be partially recovered during vehicle braking.

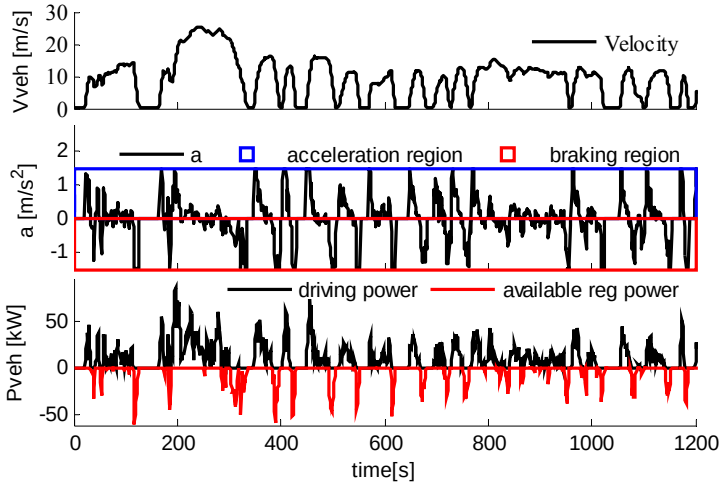

Figure 6.12 Driving information of UDDS

By observing the profile of the vehicle power, it can be seen that both the positive and negative power appears alternately; meanwhile, the amplitudes are relatively similar. Intuitively, it is possible to use a moving window with an appropriate width where the average vehicle power of the covered region can be calculated.

In Figure 6.13, the blue window in the solid line is the current position of the moving window, and the one in the dotted line is the position in the last step, where w and δt indicate the window width and moving interval, respectively. When the window moves at each step, the average value of the vehicle power over the covered region is assigned to the current point.

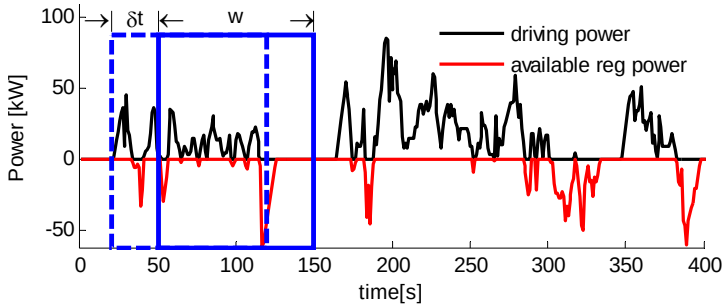

Figure 6.13 Vehicle power with the moving window

In this study, the moving interval δt is fixed at 1 second; whereas, the window width is studied with three different values (10, 50 and 100 seconds), shown in the following figures. Both the average

driving and regenerative power at each second are obtained with the moving average window.

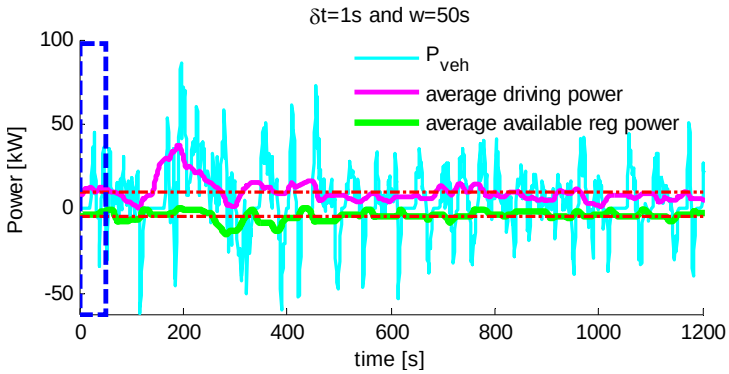

Figure 6.14 Vehicle power with a 50s window

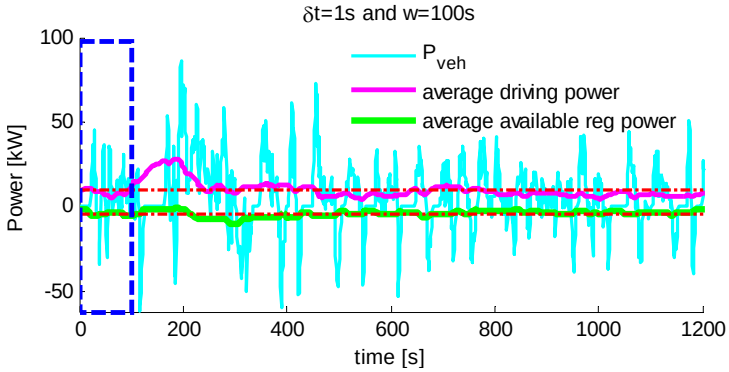

Figure 6.15 Vehicle power with a 100s window

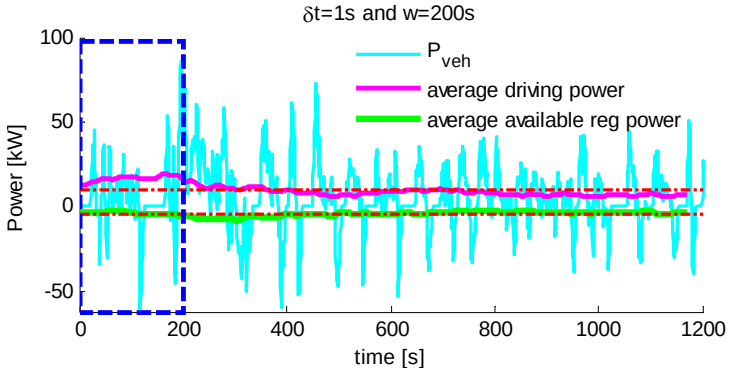

Figure 6.16 Vehicle power with a 200s window

Figure 6.14 to Figure 6.16 indicate that as the window width increases, the profiles of the driving and braking power tend to be smoother. Finally, a window size of 100s will be chosen and used in the MPC development by considering the prediction accuracy and computational cost.

As a prerequisite for developing the MPC, the vehicle power in the prediction horizon should be known a priori. In this research, inspired by the frozen-time MPC, the future vehicle power

information in the prediction horizon will be repeated by the latest historical data. In other words, the vehicle power in the last 100s will be mirrored by the one in the next 100s shown in Figure 6.17.

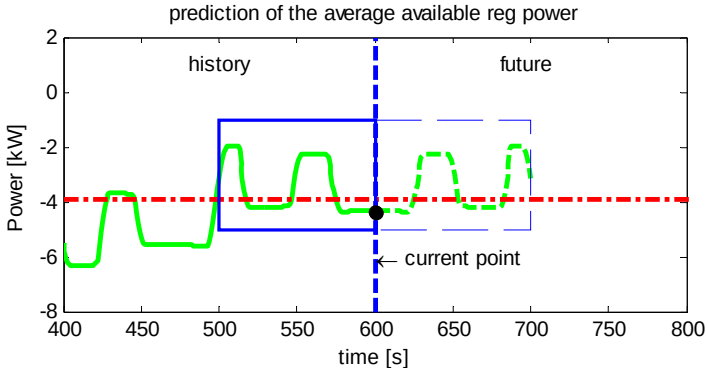

Figure 6.17 Vehicle power estimation

6.2.2.2 Model predictive PMS Development

The same procedure is used as that discussed in section 6.2.1. After the generic process of developing an MPC, different MPCs can be designed based on different future information acquisition methods. In Table 6.5, three MPCs are provided and compared in next section. The estimated average future information cannot know when the engine works at a high efficiency in the prediction horizon. Thus, an extra rule is added to the MPC^2. More specifically, MPC^2 does not directly send it to the system after obtaining the solution. Instead, it calculates the current efficiency of the engine at the same time. If the efficiency is over a limit, the calculated optimal control input will send a signal to the system; otherwise, a zero is sent out. This way, the proposed MPC can only generate the control input during a high engine efficiency period.

Table 6.5 MPC Types

MPC types	Description
MPC^1	Prescient MPC
MPC^2	Utilizes the latest 100s driving info as the future driving info
MPC^3	MPC^2 +a rule

6.2.2.3 Case Study

In this section, three cases are studied. First, the aforementioned three MPCs are simulated under the standard urban drive cycle UDDS, which is used to tune the controller parameters. Secondly, with the preliminary knowledge of the urban drive cycle obtained by studying UDDS, all the MPCs are tested

under a new highway drive cycle. Finally, a more real drive cycle for a long-haul truck or a delivery truck is created, under which all the simulations are conducted. The service load is the same as discussed in the previous section.

6.2.2.3.1 UDDS

Before running the simulation, the parameters of the MPC should be set. The tuned parameters of the MPCs are provided in Table 6.6. In order to protect the battery and elongate its lifespan, the SoC should be in a certain range. In addition, the energy stored in the battery will be used to power the A/C-R system and reduce idling, so the SoC should maintain at a high level during travel. Furthermore, the SoC should not reach its limits in order to enhance the overall efficiency [117]. Therefore, in this paper, the SoC reference (0.9) is chosen and a relatively small weight (0.5) is used to avoid the actual SoC deviating from its reference too far. The prediction horizontal length N should not be too large or small to consider both the prediction accuracy and optimality. A weight that is ten times larger terminal is chosen to enhance the stability of the controllers [141].

Table 6.6 MPC Parameters

Parameters	$T_s(\text{sec})$	N	Q	P	R	y_{ref}
Value	10	10	0.5	10Q	1	0.9

The SoC performance for each MPC is presented in Figure 6.18, where all SoCs start from a same initial value of 0.9.

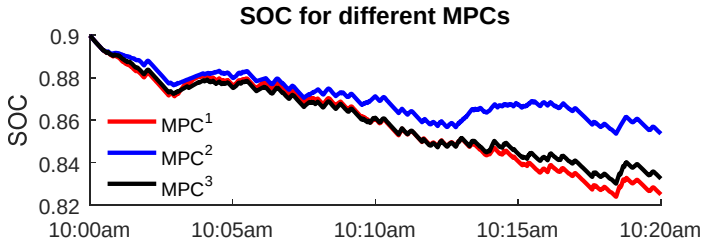

Figure 6.18 SoC performance of different MPC

The prescient MPC (MPC^1) charges the battery less than others because the SoC is still far from its lower limit of 0.6, and it only charges the battery during high engine efficiency if needed, as shown in Figure 6.19.

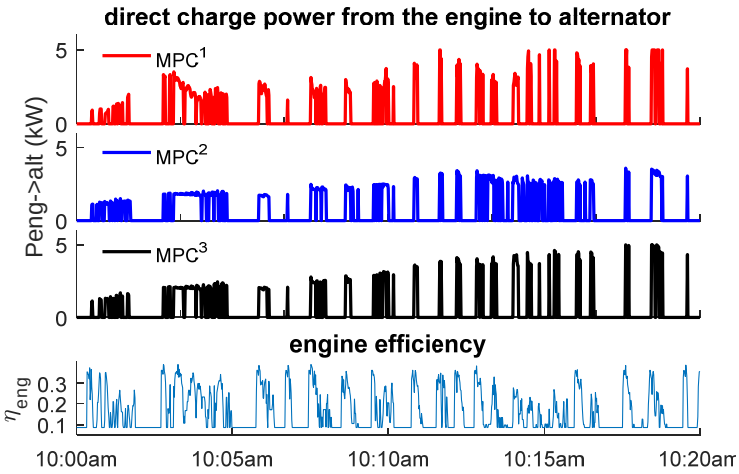

Figure 6.19 system input and engine efficiency

The MPC^2 utilizes the latest data as future information, and it charges the battery much more than others during both high and low engine efficiency periods while presenting the highest SoC. If an efficiency limit is added, it can be seen that the MPC^3 charges the battery when the efficiency is over its limit. The engine efficiency is also provided.

In order to demonstrate the advantage of the proposed RAPS as well as the MPC regarding the energy efficiency, the fuel consumption in different cases are provided in Table 6.7. The fuel consumption of the conventional configuration is 2.083L, while the power used for driving the vehicle is 1.755L. Since the RAPS is introduced to electrify the auxiliary system (e.g. A/C-R system in this study), it has nothing to do with the fuel used to power the vehicle. Instead, it can minimize the fuel consumption of the A/C-R system in an optimal way. To compensate for the SoC difference between the initial and final values, the correction method proposed in [151] is used such that the comparison can be performed. After introducing RAPS into the service vehicle, it witnesses obvious fuel savings under the studied scenario. However, the saving percentage depends on the MPC used. MPC^2 saves less than MPC^1, but after the efficiency limit is introduced, MPC^3 performs similarly to MPC^1. The engine efficiency limit (15%) in MPC^3 is tuned in this scenario and will be used in other cases.

Table 6.7 Result comparison for each MPC

		FINAL SOC	FC^1 (L)	$SAVE^1$ (%)	FC^2 (L)	$SAVE^2$ (%)
w/o RAPS		N/A	2.083	basis	0.328	basis
With RAPS	MPC^1	0.8251	1.841	9.22	0.136	58.55
	MPC^2	0.8536	1.912	6.72	0.188	42.70
	MPC^3	0.8326	1.849	9.08	0.139	57.63
Vehicle		N/A	1.755	N/A	N/A	N/A

FC^1: total fuel consumption; FC^2: fuel consumption of A/C-R system; $Save^1$: fuel saving percentage due to adding RAPS; $Save^2$: fuel saving percentage of A/C-R system due to adding RAPS;

6.2.2.3.2 Highway (HWFET+US06)

In order to verify the reliability of the obtained parameters in the last section and the robustness of the proposed MPC, a highway drive cycle is created, which consists of two standard highway cycles. From the following figures and table, the similar conclusion as that of the UDDS can be drawn with less fuel saving.

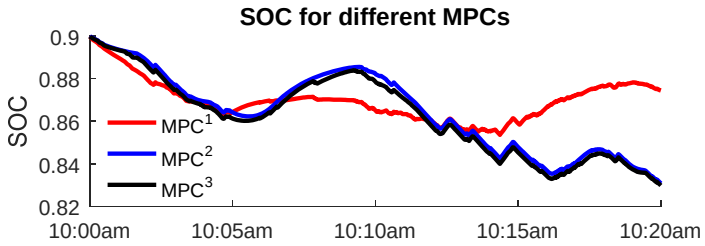

Figure 6.20 SoC performance of different MPC

This is because highway driving cannot recover as much braking power as the urban driving and with much less engine idling. It can be seen that although vehicle power used for predictions obtained from the historical data (UDDS), MPC^3 still guarantees good performance as MPC^1 under a totally different drive cycle. Thus, the robustness of the proposed MPC is verified.

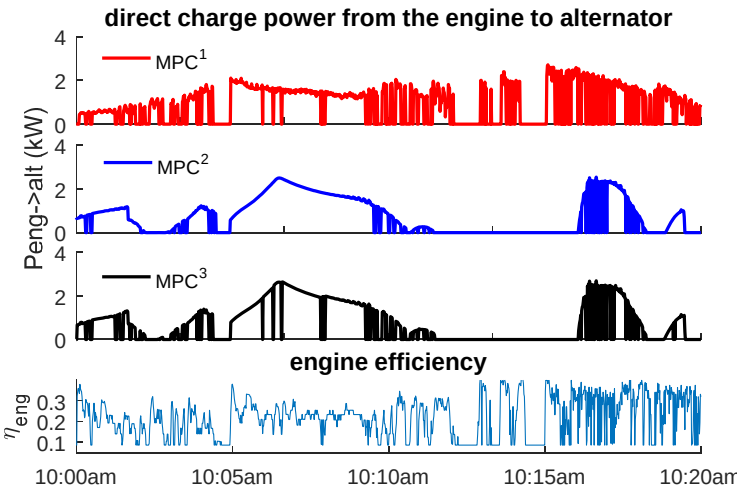

Figure 6.21 System input and engine efficiency

Table 6.8 Result Comparison for each MPC

		Final SoC	FC[1] (L)	Save[1] (%)	FC[2] (L)	Save[2] (%)
w/o RAPS		N/A	4.240	basis	0.278	basis
With RAPS	MPC[1]	0.8744	4.158	1.93	0.153	34.86
	MPC[2]	0.8308	4.178	1.46	0.173	26.31
	MPC[3]	0.8298	4.165	1.77	0.160	31.99
Vehicle		N/A	4.005	N/A	N/A	N/A

6.2.2.3.3 Combined Drive Cycle

This drive cycle is created to simulate the driving schedule of long-haul trucks or delivery trucks. The combined drive cycle is composed of urban driving, highway driving, and even rest or loading & unloading stops. The detailed information of the combined drive cycle for 2.5 hours is shown in Table 6.9 and Figure 6.22.

Table 6.9 Combined Drive cycle

Segment	Duration (s)
FTP75	1874
HWFET	765
Resting	600
UDDS	1370
FTP75	1874
US06	600
Resting	600
UDDS	1017

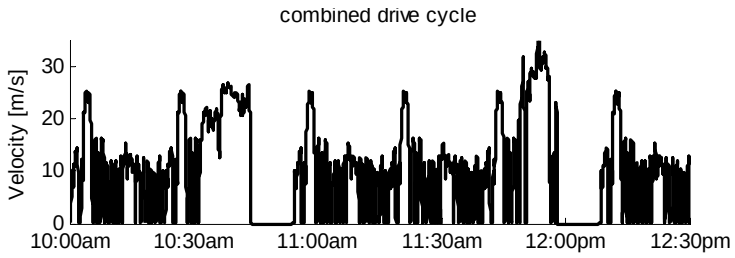

Figure 6.22 Combined drive cycle

All the MPCs are simulated over this drive cycle by using the same parameters as the first two cases. SoC performance and the system input are obtained and provided in the following two figures. It can be seen that even under a more complex and different drive cycle and without knowing any future driving information, MPC^3 performs similarly to the MPC^1. The conclusion can be drawn that the proposed, average concept based MPC^3 can be applied in RAPS with a sub-optimal performance.

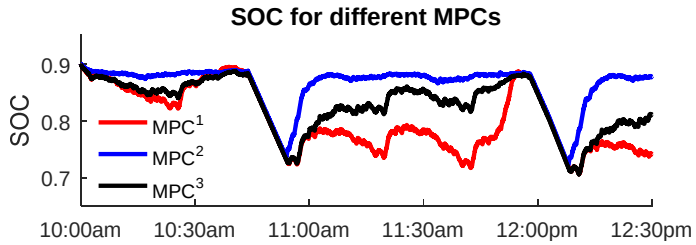

Figure 6.23 SoC performance of different MPC

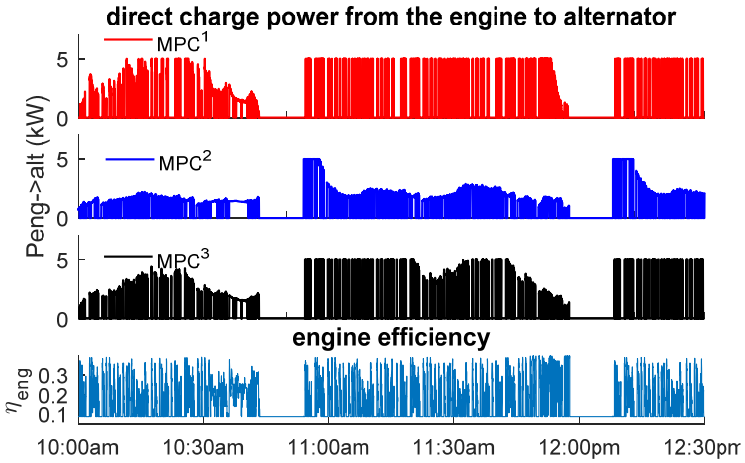

Figure 6.24 System input and engine efficiency

In addition, two points should be noted. First, the auxiliary power is less than 1 kW, which makes it a light duty service vehicle. Even so, RAPS can save approximately 10% in fuel savings. For heavy duty service vehicles, more savings will be witnessed. Second, all the simulations above are running in a charge-sustaining mode. Actually, if the destination or charging station information is available from GPS, the charge-depleting model can also be implemented. The basic idea is that based on the average regenerative braking, the auxiliary power needed, the current SoC, and the time left to the charging station, the controller is able to decide if it is necessary to charge the battery such that the SoC reaches its lower limit when the vehicle arrives at the charging station.

Table 6.10 Result comparison for each MPC

		Final SoC	FC[1] (L)	Save[1] (%)	FC[2] (L)	Save[2] (%)
w/o RAPS		N/A	16.3941	basis	2.563	basis
With RAPS	MPC[1]	0.7414	14.955	8.75	1.126	56.02
	MPC[2]	0.8779	15.934	2.78	2.105	17.78
	MPC[3]	0.8106	14.990	8.54	1.160	54.70
Vehicle		N/A	13.831	N/A	N/A	N/A

6.2.2.4 Conclusions

The goal of this section was to develop a robust model predictive PMS without knowing future driving information for the proposed RAPS. By integrating the proposed RAPS and power management into the powertrain of a conventional service vehicle, auxiliary systems are electrified and idling will be eliminated. The RAPS with different MPCs were simulated under several cases.

The first case was used to find and tune the controller parameters while others were utilized to verify the robustness of the controller. The results demonstrated that approximately 10% fuel can be saved by applying the proposed RAPS and the MPC-based power management in light service vehicles under all cases. In addition, the proposed MPC^3 can find a solution very close to the optimal one without knowing future driving information. The results demonstrate that the proposed MPC is robust and applicable to any drive and load cycles.

Chapter 7
Holistic Controller Development for the Whole System

This chapter presents a holistic controller of the RAPS. The holistic controller is an MPC to guarantee the service vehicle save energy by achieving two objectives: minimize the energy consumption of the auxiliary systems, optimize the output power of the engine. Thanks to the multi-objective optimization feature of the MPC, the proposed holistic controller optimizes the power consumption of auxiliary systems and power flow of the powertrain simultaneously for the first time. In order to show the advantages brought by the proposed RAPS with the controller over the conventional vehicles, a case study is performed and analyzed. The results demonstrate that the RAPS can help a light service vehicle save about 7 % fuel under the study scenario and even more for heavy vehicles.

7.1 Holistic Controller Configuration and Modeling

The dynamics of the powertrain, as well as the A/C-R system, can be represented by a seven-state model with four inputs: the direct charge power $P_{eng\to alt}$, the compressor speed N_{comp} as well as the frequencies (N_{evap} and N_{cond}) of two variable frequency drives used to manipulate the speed of the evaporator and condenser fans. The frequencies are proportional to the two fan speeds. The seven states are pressures of the evaporator and the condenser, the two-phase section lengths, equivalent tube wall & fins temperatures of two heat exchangers, and the temperature of the cargo, respectively. The outputs are the air temperature T_{cargo} of the cargo and the SoC of the battery. The whole model can be put into a discrete-time linear compact form after linearization and discretization as follows：

$$\begin{cases} x(k+1) = A(k)x(k) + B_u(k)u(k) + B_v(k) \\ y(k) = C(k)x(k) \end{cases} \tag{7.1}$$

$$x = \left[P_e, P_c, l_e, T_{wfe}, T_{wfc}, T_{cargo}, SOC \right]^T \tag{7.2}$$

$$u = \left[N_{comp}, N_{evap}, N_{cond}, P_{eng\to alt} \right]^T \tag{7.3}$$

$$y = \left[T_{cargo}, SOC \right]^T \tag{7.4}$$

The complete version of the whole system model is provided in Appendix B.

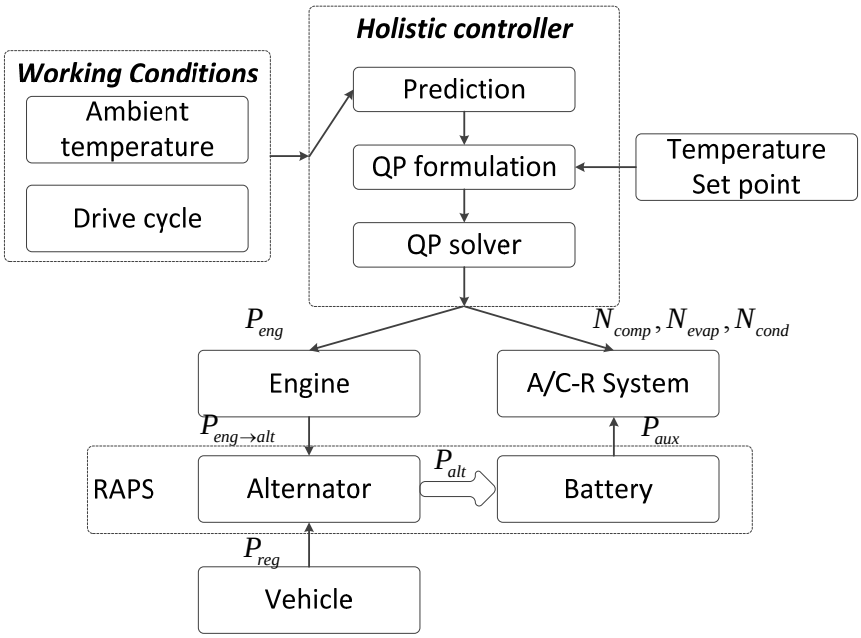

Figure 7.1 Whole structure of the RAPS with the holistic controller

7.2 Case study

7.2.1 Drive Cycle

The nominal drive cycle is used to simulate the predefined drive cycle of the service vehicle and created based on the segment information shown in the first column of Table 7.1.

Table 7.1 Drive cycles

Nominal		Real	
Segment	Duration (s)	Segment	Description
Loading	900	Unloading	
FTP75	1874	FTP75	
HWFET	765	HWFET	
FTP75	1874	UDDS	Switch the orders of two
Unloading	600	Unloading	segments + disturbance
UDDS	1370	FTP75	
Unloading	600	Unloading	
UDDS	1017	UDDS	

Due to the aforementioned factors that affect the driving in the real world, about 15% white noise is added and two segments are switched to form the real-world drive cycle. The new 2.5-hour drive

cycle is described in Figure 7.2, where the bottom figure shows the amplified vehicle velocity around 10:30 am.

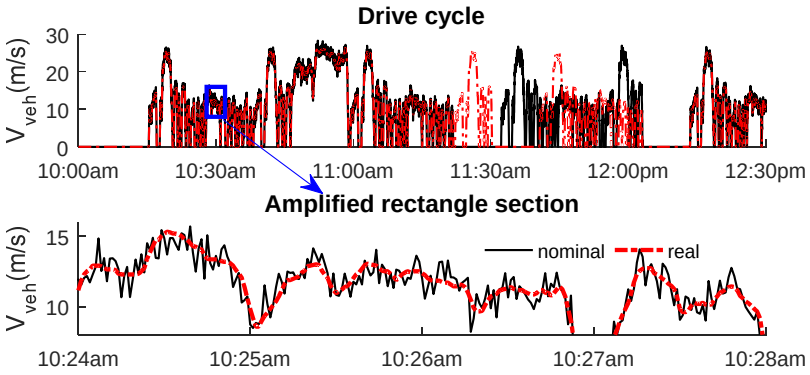

Figure 7.2 Nominal and real drive cycles

7.2.2 Service Cycle

The service cycle shows the power consumed by the auxiliary devices of the service vehicle. As the main auxiliary device, the A/C-R systems consume much more fuel than other auxiliary systems, and its power consumption is varying with the ambient and operating conditions of service vehicles. Figure 7.3 shows the ambient temperature and the heating load (HL) applied to the cargo in a typical summer morning from 10:00 am to 12:30 pm. For simplicity, the HL is assumed to be proportional to the temperature difference.

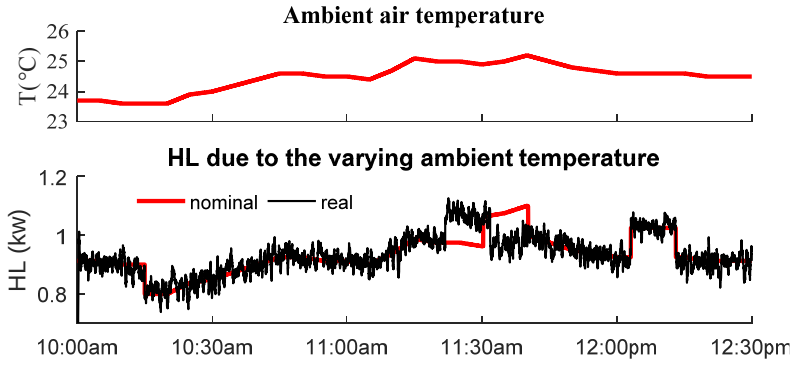

Figure 7.3 Ambient temperature and HL

In addition, some extra HL appears during the periods of loading and unloading due to the door opening. The extra HL is roughly assumed to be 0.1 kW and added to the existing HL forming the

nominal service cycle as shown in Figure 7.3. The real one with the disturbances is obtained by using the same method as that of the drive cycle.

7.2.3 Results Analysis

In this section, in order to show the benefits brought by the proposed RAPS with the holistic controller, it is compared to the conventional vehicle with an On/off A/C-R system controller. Meanwhile, to demonstrate the proposed controller is robust, two MPCs are simulated and compared. The first one (MPC^1) as the prescient MPC knows the full real-world drive cycle and service cycle as a priori; whereas the second one (MPC^2) only knows the nominal drive and service cycle. The parameters of the MPCs are provided in Table 7.2.

Table 7.2 MPC Parameters

T_s	N	Q	P	R	r	y_{ref}
$10s$	10	$\begin{bmatrix} 10 & 0 \\ 0 & 1 \end{bmatrix}$	$10Q$	$\begin{bmatrix} 10 & & & \\ & 0 & & \\ & & 0 & \\ & & & (1/\eta)^T 1(1/\eta) \end{bmatrix}$	$\begin{bmatrix} 1 & & \\ & 0.1 & \\ & & 0 \\ & & & 0 \end{bmatrix}$	$\begin{bmatrix} 10 \\ 0.9 \end{bmatrix}$

In order to protect and elongate the lifespan of the battery, it should not be drained and its SoC should not reach its limits to pursue high overall efficiency [117]. In addition, the battery is used to power the A/C-R system and reduce idling, so the SoC should maintain a high level during the vehicle in travel. Therefore, the SoC reference 0.9 is chosen and a relatively small weight is used to avoid it deviating from the reference too far. The prediction horizontal length N should not be too large or small to balance the prediction accuracy and optimality. A ten-time larger terminal weight is chosen to enhance the stability of the controllers as suggested in [141]. The engine efficiency item is added into the input weight matrix to guarantee the direct charging happens at the high-efficiency periods. The QP is solved by an open source solver, which can solve the QP in milliseconds to guarantee its real-time applicability [136].

Figure 7.4 shows SoC response of the battery. During the loading & unloading periods, the battery is discharging without any charging from the engine in order to eliminate the engine idling. When the vehicle is braking, the battery is charged by the recovered braking energy. However, if the SoC is far from the reference or the regenerative braking energy is not enough, the battery is charged by the engine automatically during the high-efficiency periods. The controller determines whether or when to charge the battery according to the prediction behaviors. Figure 7.5 describes the inside temperature response of the cargo. The initial temperature is assumed to be equal to the ambient

temperature at 10 am when the A/C-R system starts working. After about 15 minutes, the temperature reaches its reference 10°C and stay there, even under the extra HL periods.

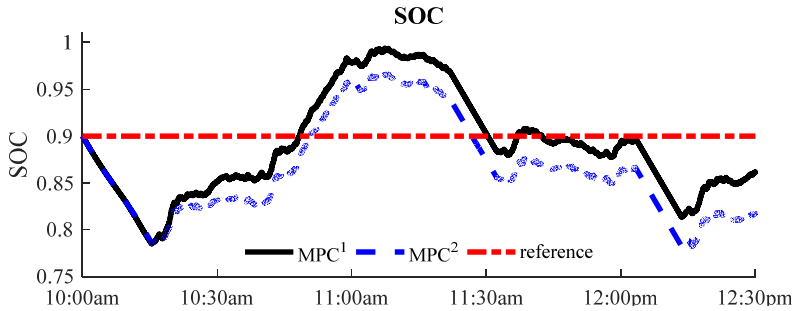

Figure 7.4 SoC trajectories

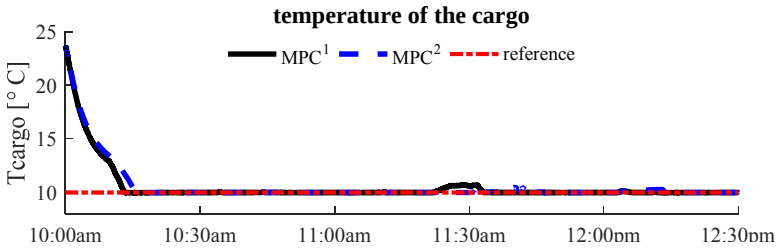

Figure 7.5 Temperature performance of the cargo

The A/C-R system inputs are presented in Figure 7.6 to Figure 7.8. At the beginning, the initial temperature is far from the set point. The A/C-R system runs at the maximum capacity to cool the cargo. After it arrives at its set point, the inputs start to change according to the ambient HL. Figure 7.9 shows the charging power of the battery by the engine during the high-efficiency periods when the SoC is too far from its set point. When the vehicle is not moving, the charging does not happen.

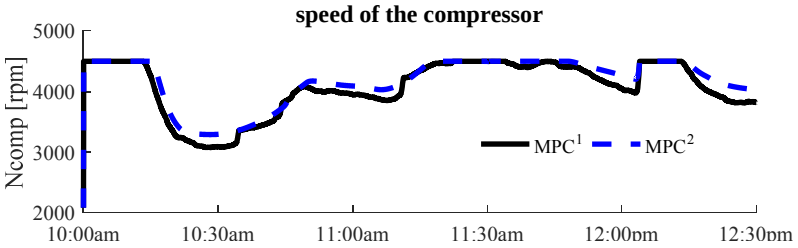

Figure 7.6 Speed of the compressor

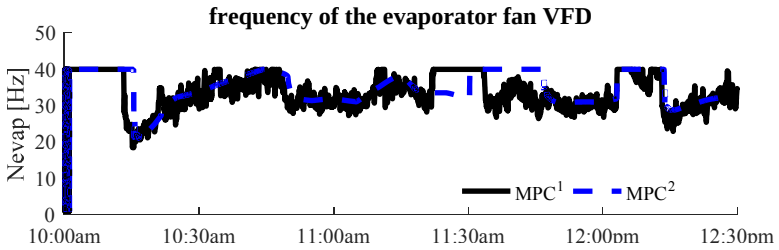

Figure 7.7 Frequency of the evaporator fan VFD

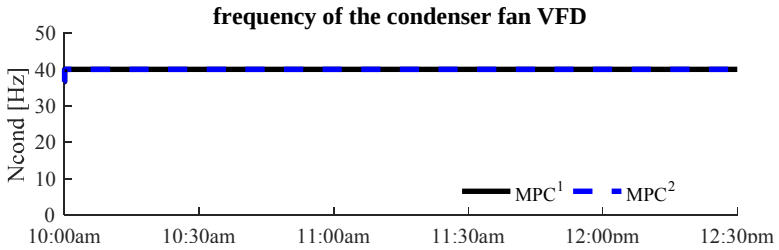

Figure 7.8 Frequency of the condenser fan VFD

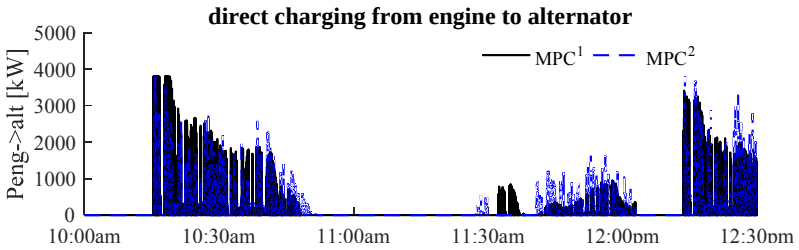

Figure 7.9 Direct charging power

To demonstrate the saving taken by the RAPS, the conventional service vehicle with an on/off controller of A/C-R system is used to compare to. Please refer to [129] for the on/off controller design procedure.

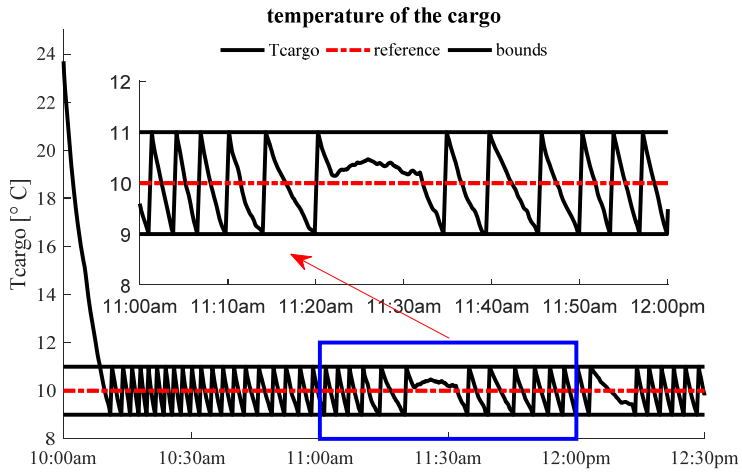

Figure 7.10 Temperature of the cargo in the conventional vehicle

The corresponding inputs of the A/C-R system are shown in the following figure. It can be seen that when the temperature goes beyond the bounds, the system inputs will switch between the maximum and zeros. During the early morning, the outside HL is low, such that the switching frequency is high. Instead, during noon, the switching frequency is low.

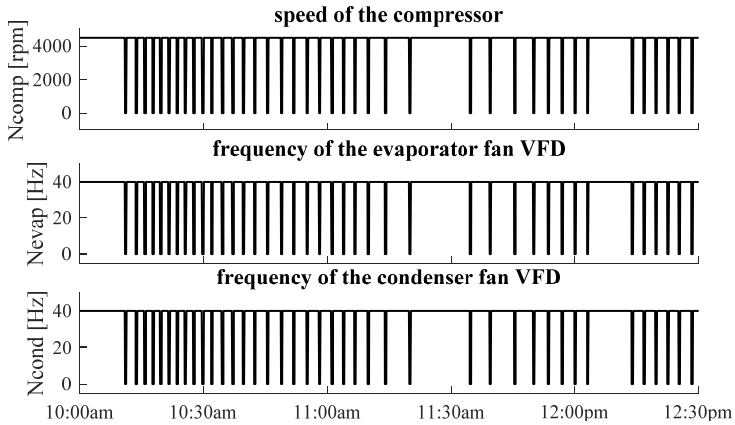

Figure 7.11 A/C-R system inputs in the conventional vehicle

The fuel consumption results are provided in Table IV. In order to eliminate the effects of the fuel consumption brought by the deviation of the final SoC of the controllers, an SoC-correction method [151] is adopted. The total fuel consumption (19.6 L) of the conventional vehicle with an on/off A/C-R system controller [129] is provided as a basis to compare with; meanwhile, the fuel consumption (18.14L) just used for driving vehicle is also provided and their difference is utilized for powering A/C-R system. By using RAPS and two MPCs, 6.9 % and 6.7% fuel are saved, respectively. That

means MPC^2 has a very close saving with the prescient MPC^1 and MPC^2 is robust enough under such large disturbed situation. In this paper, the average power (about 1kW) of A/C-R system is relatively smaller compared to vehicle power. These vehicles are called light service vehicle. However, for heavy service vehicles, they can witness more fuel saving using the RAPS. Regarding the FC^2 and $Save^2$, the FC of the A/C-R system in the conventional vehicle is 1.48 L, whereas the FC in the systems with RAPS is just 9 times less. In other words, the electrification of the A/C-R system can bring a significant saving to the vehicle owners and then to the environment.

Table 7.3 Result comparison for each MPC

		FINAL SOC	FC^1 (L)	$SAVE^1$ (%)	FC^2 (L)	$SAVE^2$ (%)
Conventional & on/off controller		N/A	19.62	basis	1.48	basis
RAPS	MPC^1	0.86	18.27	6.9	0.13	91.3
	MPC^2	0.82	18.31	6.7	0.17	88.8
Vehicle		N/A	18.14	N/A	N/A	N/A

FC^1: total fuel consumption; FC^2: fuel consumption of A/C-R system; $Save^1$: fuel saving percentage due to adding RAPS; $Save^2$: fuel saving percentage of A/C-R system due to adding RAPS;

Note: the above results are obtained based on a light service vehicle with only 10% braking energy can be captured via a serpentine belt. For the heavy service vehicle with a PTO configuration, more fuel saving will be witnessed by capturing more braking energy.

Chapter 8
Conclusions and Future Work

The ultimate goal of this thesis was to develop and realize a holistic controller for anti-idling systems for service vehicles with A/C-R systems as the major auxiliary devices.

RAPS was proposed to achieve the anti-idling objective. A/C-R systems as the main auxiliary power devices in RAPS, their power consumption should be minimized in order to enhance the energy efficiency. Therefore, a simplified control-oriented dynamic model of the automotive A/C-R system was developed that could provide a similar accuracy as those more complex models reported in the literature. In this simplified model, the fins' effects were considered and lumped into two equivalent parameters. In addition, the effects of the superheat section of the condenser were also included into the model by studying the experimental data. This model was simulated and experimentally validated under several scenarios. The results showed that this model is simple and accurate enough to be used in real-time control systems.

Based on this model, several controllers were designed, analyzed and compared for both the control performance and energy consumption. The results illustrated that the MPC was a promising controller for A/C-R systems with continuously variable components, and the hybrid MPCs could be the best choices for A/C-R systems with discrete variable components. The robustness of the proposed MPC was also tested under a large disturbed scenario and frosting conditions.

The introduction of the RAPS enables full electrification of A/C-R systems and using better controllers for them could effectively maximize the energy efficiency of the A/C-R systems in service vehicles. Another feature brought by the RAPS besides the electrification of A/C-R systems is the energy recovery by the regenerative braking to power the A/C-R systems. Obviously, the more energy captured by the RAPS the higher overall efficiency can be achieved. Therefore, a strategy based on series braking system was developed to exploit the potential of the recovered energy under the condition that the drivability of the vehicle is not affected.

By introducing the RAPS to a conventional service vehicle, its powertrain turns into parallel hybrid due to the addition of a battery. The only difference is that the battery only powers the auxiliary devices instead of assisting the engine to power the vehicle. Even so, it necessitates a PMS to decide when and how to charge/discharge the battery. Accordingly, a predictive power management was designed for both service vehicles with and without a predefined driving route. In addition, an online

KF-based identification algorithm for the vehicle mass was integrated into the PMS to develop an adaptive MPC, accounting for the varying loads due to changing passengers or cargo masses. A large step size prediction method was used in the proposed MPC to alleviate uncertainties and reduce computational costs. The robustness of the proposed MPC-based power management strategies was also tested under the uncertainties caused by traffic situations, weather conditions, or other factors in practice. Finally, the proposed MPC was compared with the prescient MPC to demonstrate its advantages over the conventional MPC. It was shown that its performance was comparable to that of the prescient MPC.

A robust model predictive PMS without knowing future driving information for the proposed RAPS was also proposed for service vehicles without a predefined driving cycle in the daily working environment. An average concept was adopted in this method. The controller was simulated under several driving scenarios and the results demonstrated that an obviously saving in fuel consumption could be achieved by applying the proposed RAPS and the MPC-based power management in light service vehicles under all cases. The results demonstrated that the proposed MPC was robust and applicable to many drive and load cycles.

For the ease of implementation, a holistic controller was presented to solve the thermal management of the cargo and power management of the powertrain system simultaneously to maximize the fuel economy. Due to the ability of prediction and multi-objective optimization, the MPC method was used for the holistic controller development. The results demonstrated approximately 7 percent of the total fuel can be saved by applying RAPS and the proposed controller in light service vehicles and more for heavy service vehicles. In addition, the proposed MPC could find the solution very close to the optimal one even under situations that the prediction drive cycle deviates far from the real one.

Future work could be focused on the following aspects:

Regarding the modeling and controllers of the A/C-R system, future studies will focus on developing some online parameter estimator to improve the accuracy of the proposed model, integrating the power consumption model of the whole system into the objective function instead of only control efforts, designing a fully controllable experimental system to test the proposed continuous MPC controller, and implementing the controller into a real vehicle to test its performance in practice.

In terms of the regenerative braking controller, the normal force of each axle or wheel can be identified to calculate the accurate friction force for each axle. In this way, the system can extract the maximum energy without influencing the drivability or stability of the vehicle.

A more adaptive algorithm for the window size should be developed to make the average-MPC concept a predictive controller to work well under all conditions. In addition, the route information obtained by the telematics technology and electric grid station information can be integrated into the power management algorithm to enhance its performance. The future work will also emphasize on the distributed MPC development for RAPS and the real performance study of the holistic or distributed controller in a delivery truck.

Bibliography

[1] M. Morshed, "Unnecessary idling of vehicles: an analysis of the current situation and what can be done to reduce it," *M.S. thesis*, McMaster University, Hamilton, Ontario., Canada, 2010.

[2] E. Dinçmen and B. A. Güvenç, "A control strategy for parallel hybrid electric vehicles based on extremum seeking," *Vehicle System Dynamics*, vol. 50, no. 2, pp. 199–227, Feb. 2012.

[3] E. Lust, "System-level analysis and comparison of long-haul truck idle-reduction technologies," *M.S. thesis*, University of Maryland, College Park, Maryland, USA, 2008.

[4] H. Khayyam *et al.*, "Intelligent energy management control of vehicle air conditioning via look-ahead system," *Applied Thermal Engineering*, vol. 31, no. 16, pp. 3147–3160, Nov. 2011.

[5] J. Liu, H. Zhou and X. Zhou, "Automotive air conditioning control–a survey," *In: International conference on electronic and mechanical engineering and information technology*, Harbin, Heilongjiang, People's Republic of China, 12–14 August, 2011, pp. 3408–3412.

[6] F. Chiara and M. Canova, "A review of energy consumption, management, and recovery in automotive systems, with considerations of future trends," *Proceedings of the Institution of Mechanical Engineers, Part D: Journal of Automobile Engineering*, vol. 227, no. 6, pp. 914–936, Mar. 2013.

[7] H. Budde-Meiwes *et al.*, "A review of current automotive battery technology and future prospects," *Proceedings of the Institution of Mechanical Engineers, Part D: Journal of Automobile Engineering*, vol. 227, no. 5, pp. 761–776, Apr. 2013.

[8] R. Johri and Z. Filipi, "Optimal energy management of a series hybrid vehicle with combined fuel economy and low-emission objectives," *Proceedings of the Institution of Mechanical Engineers, Part D: Journal of Automobile Engineering*, vol. 228, no. 12, pp. 1424–1439, Jun. 2014.

[9] M. Jalali, A. Khajepour, S. Chen, and B. Litkouhi, "Integrated stability and traction control for electric vehicles using model predictive control," *Control Engineering Practice*, vol. 54, pp. 256–266, Sep. 2016.

[10] C. Weng, X. Zhang, and J. Sun, "Adaptive model predictive control for hybrid electric vehicles power management," *Proceedings of the 32nd Chinese Control Conference*, July, 2013

[11] Website: http://www.mass.gov/eea/docs/doer/clean-cities/air-dock.pdf, Accessed: 2016-08-03.

[12] Y. Wang, *et al*, "Investigating the cost, liability and reliability of anti-idling equipment for trucks," *Delaware Department of Transportation*, report, 2007.

[13] P. Kuo, "Evaluation of Freight Truck Anti-idling Strategies for Reduction of Greenhouse Gas Emissions," *Ph.D. dissertation*, North Carolina State University, Raleigh, North Carolina, USA, 2008.

[14] H. Christopher and P. Kuo, "Best Practices Guidebook for Greenhouse Gas Reductions in Freight Transportation," *U.S. Department of Transportation*, report, 2007.

[15] Website:http://www.fors-online.org.uk/resource.php?name=PF_AA_PROCGUIDE,Accessed: 2016-08-03.

[16] J. Penney, "A Model Idling Control Program for Municipal Fleets," *Greater Toronto Area Clean Air Council*, report, 2005.

[17] G. Gereffi and K. Dubay, "Auxiliary Power Units: Reducing Carbon Emissions by Eliminating Idling in Heavy-Duty Trucks," *Duke CGGC*, report, 2008.

[18] Transport Canada, “Truck Auxiliary Power Unit Field Trial,” *Mechron Power Systems*, 2007.

[19] Website: http://www.trailermag.com.au/featured/article/thermo-kings-quiet-achiever, Accessed: 2016-08-03.

[20] Website: http://idlefreesystems.com/no-idle-elimination-systems-battery.html, Accessed: 2016-08-03.

[21] Website: http://www.ecamion.com/portfolio/eapu/, Accessed: 2016-08-03.

[22] Website: http://en.wikipedia.org/wiki/Hybrid_electric_vehicle, Accessed: 2016-08-03.

[23] Website: http://www.eaton.com/Eaton/ProductsServices/HybridPower/index.htm, Accessed: 2016-08-03.

[24] Website: http://www.freightlinertrucks.com/Trucks/Alternative-Power-Trucks/Hybrid-Electric, Accessed: 2016-08-03.

[25] Website:http://www.mitsubishifuso.com/en/products/truck/canter_hev/12/concepts/environment/hybrid/index.html, Accessed: 2016-08-03.

[26] Website:http://www.carsandracingstuff.com/library/f/freightliner.php, Accessed: 2016-08-03.

[27] Michael A. Tunnell, *et al*, "Idle Reduction Technology: Fleet Preferences Survey," *New York State Energy Research and Development*, report, 2006.

[28] Government of Alberta, "Draft Quantification Protocol for reduced vehicle idling through the use of direct fired heaters," *Climate Change Secretariat*, Edmonton, Alberta, 2011.

[29] Website: https://www.idleair.com/features/, Accessed: 2016-08-03.

[30] H. Khayyam *et al.*, "Intelligent energy management control of vehicle air conditioning via look-ahead system," *Applied Thermal Engineering*, vol. 31, no. 16, pp. 3147–3160, Nov. 2011.

[31] Kania, M., Koeln, J., Alleyne, A., McCarthy, K. et al., "A Dynamic Modeling Toolbox for Air Vehicle Vapor Cycle Systems," *SAE Technical Paper* 2012-01-2172, 2012, doi:10.4271/2012-01-2172.

[32] X. He, "Dynamic modeling and multivariable control of vapor compression cycles in air conditioning systems," *Ph.D. dissertation*, Massachusetts Institute of Technology, Cambridge, Massachusetts, USA, 1996

[33] J. W. MacArthur and E. W. Grald, "Unsteady compressible two-phase flow model for predicting cyclic heat pump performance and a comparison with experimental data," *International Journal of Refrigeration*, vol. 12, no. 1, pp. 29–41, Jan. 1989.

[34] B. Rasmussen and A. Alleyne, "Dynamic modeling and advanced control of air conditioning and refrigeration systems," *ACRC Technical Report* 244, Air Conditioning and Refrigeration Center, University of Illinois, Urbana, Illinois, USA, 2006.

[35] G. L. Wedekind, B. L. Bhatt, and B. T. Beck, "A system mean void fraction model for predicting various transient phenomena asSoCiated with two-phase evaporating and condensing flows," *International Journal of Multiphase Flow*, vol. 4, no. 1, pp. 97–114, Mar. 1978.

[36] B. Li, "Dynamic modeling and control of vapor compression cycle systems with shut-down and start-up operations," M.S. thesis, University of Illinois at Urbana–Champaign, Champaign, Illinois, USA, 2009.

[37] B. Eldredge and A. Alleyne, "Improving the accuracy and scope of control-oriented vapor compression cycle system models," *ACRC Technical Report* 246, Air Conditioning and Refrigeration Center, University of Illinois, USA, 2006.

[38] M. Fasl, "Modeling and control of hybrid vapor compression cycles," *M.S. thesis*, University of Illinois at Urbana–Champaign, Champaign, Illinois, USA, 2013.

[39] R. Shah, A. Alleyne, C. Bullard et al, "Dynamic modeling and control of single and multi-evaporator subcritical vapor compression systems," *ACRC Technical Report* 216, Air Conditioning and Refrigeration Center, University of Illinois, Urbana, Illinois, USA, 2003.

[40] B. Rasmussen, "Control-oriented modeling of transcritical vapor compression systems," *M.S. Thesis*, University of Illinois at Urbana-Champaign, Champaign, Illinois, USA, 2002.

[41] B. Li, N. Jain, W. Mohs, *et al*. "Dynamic modeling of refrigerated transport systems with cooling-mode/heating-mode switch operations," *HVAC&R Res*, 18(5): 974–996, 2012.

[42] T. L. McKinley and A. G. Alleyne, "An advanced nonlinear switched heat exchanger model for vapor compression cycles using the moving-boundary method," *International Journal of Refrigeration*, vol. 31, no. 7, pp. 1253–1264, Nov. 2008.

[43] X. He, S. Liu, and H. H. Asada, "Modeling of vapor compression cycles for Multivariable feedback control of HVAC systems," *Journal of Dynamic Systems, Measurement, and Control*, vol. 119, no. 2, p. 183, 1997.

[44] J. Cai, "Control of refrigeration systems for Trade-off between energy consumption and food quality loss," *Ph.D. dissertation*, Fredrik BajersVej 7C, 9220 Aalborg East, Denmark, 2007.

[45] A. Leva, L. Piroddi, M. Di Felice, A. Boer, and R. Paganini, "Adaptive relay-based control of household freezers with on–off actuators," *Control Engineering Practice*, vol. 18, no. 1, pp. 94–102, Jan. 2010.

[46] B. Li, R. Otten, V. Chandan, W. F. Mohs, J. Berge, and A. G. Alleyne, "Optimal on–off control of refrigerated transport systems," *Control Engineering Practice*, vol. 18, no. 12, pp. 1406–1417, Dec. 2010.

[47] M. Mohanraj, S. Jayaraj, and C. Muraleedharan, "Applications of artificial neural networks for refrigeration, air-conditioning and heat pump systems—A review," *Renewable and Sustainable Energy Reviews*, vol. 16, no. 2, pp. 1340–1358, Feb. 2012.

[48] B. Koo, Y. Yoo, and S. Won, "Super-twisting algorithm-based sliding mode controller for a refrigeration system," *In Control, Automation and Systems (ICCAS)*, 12th International Conference on (pp. 34-38). IEEE, October, 2012.

[49] B. Rasmussen, and A. Alleyne, "Dynamic modeling and advanced control of air conditioning and refrigeration systems," *ACRC* report. College of Engineering. University of Illinois at Urbana-Champaign, 2006

[50] L. Larsen, "Model based control of refrigeration systems," *Ph.D. dissertation*, Department of Control Engineering, Aalborg University, DK - 9100 Aalborg, Denmark, 2006.

[51] J. M. Sousa, R. Babuška, and H. B. Verbruggen, "Fuzzy predictive control applied to an air-conditioning system," *Control Engineering Practice*, vol. 5, no. 10, pp. 1395–1406, Oct. 1997.

[52] M. He, W. Cai, and S. Li, "Multiple fuzzy model-based temperature predictive control for HVAC systems," *Information Sciences*, vol. 169, no. 1-2, pp. 155–174, Jan. 2005.

[53] M. Razi, M. Farrokhi, and M. Saeidi, "Neuro-predictive control for automotive air conditioning system," In Engineering of Intelligent Systems, IEEE International Conference on (pp. 1-6). IEEE, April, 2006.

[54] M. Elliott, and B. Rasmussen, "Model-based predictive control of a multi-evaporator vapor compression cooling cycle," *In American Control Conference*, (pp. 1463-1468). IEEE, 2008.

[55] G. Huang and A. L. Dexter, "Realization of robust nonlinear model predictive control by offline optimisation," *Journal of Process Control*, vol. 18, no. 5, pp. 431–438, Jun. 2008.

[56] N. Jain, and A. Alleyne, "Thermodynamics-based optimization and control of vapor-compression cycle operation: optimization criteria," In American Control Conference (ACC), pp. 1352-1357. IEEE, June, 2011.

[57] J. Ma, J. Qin, T. Salsbury, and P. Xu, "Demand reduction in building energy systems based on economic model predictive control," *Chemical Engineering Science*, vol. 67, no. 1, pp. 92–100, Jan. 2012.

[58] A. Gustavsson, "Dynamic modeling and Model Predictive Control of a vapor compression system," *PhD dissertation*, Department of Electrical Engineering, Automatic Control. Linköping University, The Institute of Technology, Linköping University, 2012.

[59] T. G. Hovgard, L. F. S. Larsen, J. B. Jørgensen, and S. Boyd, "Fast Nonconvex model predictive control for commercial refrigeration," *IFAC Proceedings Volumes*, vol. 45, no. 17, pp. 514–521, 2012.

[60] F. Blanchin and W. Ukovich, "Linear programming approach to the control of discrete-time periodic systems with uncertain inputs," *Journal of Optimization Theory and Applications*, vol. 78, no. 3, pp. 523–539, Sep. 1993.

[61] A. Aswani, N. Master, J. Taneja, D. Culler, and C. Tomlin, "Reducing transient and steady state electricity consumption in HVAC using learning-based model-predictive control," *Proceedings of the IEEE*, vol. 100, no. 1, pp. 240–253, Jan. 2012.

[62] M. S. Elliott and B. P. Rasmussen, "Decentralized model predictive control of a multi-evaporator air conditioning system," *Control Engineering Practice*, vol. 21, no. 12, pp. 1665–1677, Dec. 2013.

[63] A. Afram and F. Janabi-Sharifi, "Theory and applications of HVAC control systems – A review of model predictive control (MPC)," *Building and Environment*, vol. 72, pp. 343–355, Feb. 2014.

[64] K. K. Sørensen, J. Stoustrup, and T. Bak, "Adaptive MPC for a reefer container," *Control Engineering Practice*, vol. 44, pp. 55–64, Nov. 2015.

[65] F. R. Salmasi, "Control strategies for hybrid electric vehicles: Evolution, classification, comparison, and future trends," *IEEE Transactions on Vehicular Technology*, vol. 56, no. 5, pp. 2393–2404, Sep. 2007.

[66] K. T. Chau and Y. S. Wong, "Overview of power management in hybrid electric vehicles," *Energy Conversion and Management*, vol. 43, no. 15, pp. 1953–1968, Oct. 2002.

[67] S. G. Wirasingha and A. Emadi, "Classification and review of control strategies for plug-in hybrid electric vehicles," *IEEE Transactions on Vehicular Technology*, vol. 60, no. 1, pp. 111–122, Jan. 2011.

[68] K. Çağatay Bayindir, M. A. Gözüküçük, and A. Teke, "A comprehensive overview of hybrid electric vehicle: Powertrain configurations, powertrain control techniques and electronic control units," *Energy Conversion and Management*, vol. 52, no. 2, pp. 1305–1313, Feb. 2011.

[69] L. Serrao, S. Onori, and G. Rizzoni, "A comparative analysis of energy management strategies for hybrid electric vehicles," *Journal of Dynamic Systems, Measurement, and Control*, vol. 133, no. 3, p. 031012, 2011.

[70] S. F. Tie and C. W. Tan, "A review of energy sources and energy management system in electric vehicles," *Renewable and Sustainable Energy Reviews*, vol. 20, pp. 82–102, Apr. 2013.

[71] A. A. Malikopoulos, "Supervisory power management control Algorithms for hybrid electric vehicles: A survey," *IEEE Transactions on Intelligent Transportation Systems*, vol. 15, no. 5, pp. 1869–1885, Oct. 2014.

[72] P. Zhang, F. Yan, and C. Du, "A comprehensive analysis of energy management strategies for hybrid electric vehicles based on bibliometrics," *Renewable and Sustainable Energy Reviews*, vol. 48, pp. 88–104, Aug. 2015.

[73] M. F. M. Sabri, K. A. Danapalasingam, and M. F. Rahmat, "A review on hybrid electric vehicles architecture and energy management strategies," *Renewable and Sustainable Energy Reviews*, vol. 53, pp. 1433–1442, Jan. 2016.

[74] A. Panday and H. O. Bansal, "A review of optimal energy management strategies for hybrid electric vehicle," *International Journal of Vehicular Technology*, vol. 2014, pp. 1–19, 2014.

[75] A. Boukehili, Y. T. Zhang, Q. Zhao, C. Q. Ni, H. F. Su, and G. J. Huang, "Hybrid vehicle power management modeling and refinement," *International Journal of Automotive Technology*, vol. 13, no. 6, pp. 987–998, Oct. 2012.

[76] Johnson, V., Wipke, K., and Rausen, D., "HEV Control Strategy for Real-Time Optimization of Fuel Economy and Emissions," *SAE Technical Paper* 2000-01-1543, doi:10.4271/2000-01-1543.

[77] Anthony M. Phillips, "Vehicle system controller design for a hybrid electric vehicle," *Proceedings of the IEEE International Conference on Control Applications Anchorage, Alaska*, USA September 25-27, 2000.

[78] H.-D. Lee and S.-K. Sul, "Fuzzy-logic-based torque control strategy for parallel-type hybrid electric vehicle," *IEEE Transactions on Industrial Electronics*, vol. 45, no. 4, pp. 625–632, 1998.

[79] H.-D. Lee *et al.*, "Torque control strategy for a parallel-hybrid vehicle using fuzzy logic," *IEEE Industry Applications Magazine*, vol. 6, no. 6, pp. 33–38, 2000.

[80] J.-S. Won and R. Langari, "Fuzzy torque distribution control for a parallel hybrid vehicle," *Expert Systems*, vol. 19, no. 1, pp. 4–10, Feb. 2002.

[81] B. M. Baumann, G. Washington, B. C. Glenn, and G. Rizzoni, "Mechatronic design and control of hybrid electric vehicles," *IEEE/ASME Transactions on Mechatronics*, vol. 5, no. 1, pp. 58–72, Mar. 2000.

[82] N. J. Schouten, M. A. Salman, and N. A. Kheir, "Fuzzy logic control for parallel hybrid vehicles," *IEEE Transactions on Control Systems Technology*, vol. 10, no. 3, pp. 460–468, May 2002.

[83] P. Pisu, K. Koprubasi and G. Rizzoni, "Energy management and drivability control problems for hybrid electric vehicles," *44th IEEE Conference on Decision and Control, and the European Control Conference*, 2005.

[84] M. O'Keefe and T. Market, "Dynamic programming applied to investigate energy management strategies for a plug-in HEV," *Conference Paper NREL/CP-540-40376*, 2006.

[85] S. J. Moura, H. K. Fathy, D. S. Callaway, and J. L. Stein, "A stochastic optimal control approach for power management in plug-in hybrid electric vehicles," *IEEE Transactions on Control Systems Technology*, vol. 19, no. 3, pp. 545–555, May 2011.

[86] M. Montazeri-Gh, A. Poursamad, and B. Ghalichi, "Application of genetic algorithm for optimization of control strategy in parallel hybrid electric vehicles," *Journal of the Franklin Institute*, vol. 343, no. 4-5, pp. 420–435, Jul. 2006.

[87] M. M. Gh and A. Poursamad, "Application of genetic algorithm for simultaneous optimisation of HEV component sizing and control strategy," *International Journal of Alternative Propulsion*, vol. 1, no. 1, p. 63, 2006.

[88] A. Piccolo, *et al*. "Optimization of energy flow management in hybrid electric vehicles via genetic algorithms," *IEEUASME International Conference on Advanced Intelligent Mechatronics Proceedings*, Como, Italy, 2001.

[89] R. A. Rutenbar, "Simulated annealing algorithms: An overview," *IEEE Circuits and Devices Magazine*, vol. 5, no. 1, pp. 19–26, Jan. 1989.

[90] S. Delprat, J. Lauber, T. M. Guerra, and J. Rimaux, "Control of a parallel hybrid powertrain: Optimal control," *IEEE Transactions on Vehicular Technology*, vol. 53, no. 3, pp. 872–881, May 2004.

[91] L. Serrao, S. Onori, and G. Rizzoni, "ECMS as a realization of Pontryagin's minimum principle for HEV control, " *in Proc. Amer. Control Conf. (ACC)*, pp. 3964–3969, Jun. 2009,

[92] N. Kim, S. Cha, and H. Peng, "Optimal control of hybrid electric vehicles based on Pontryagin's minimum principle," *IEEE Transactions on Control Systems Technology*, vol. 19, no. 5, pp. 1279–1287, Sep. 2011.

[93] P. Pisu and G. Rizzoni, "A comparative study of supervisory control strategies for hybrid electric vehicles," *IEEE Transactions on Control Systems Technology*, vol. 15, no. 3, pp. 506–518, May 2007.

[94] C. Musardo, G. Rizzoni, Y. Guezennec, and B. Staccia, "A-ECMS: An Adaptive algorithm for hybrid electric vehicle energy management," *European Journal of Control*, vol. 11, no. 4-5, pp. 509–524, Jan. 2005.

[95] B. Gu and G. Rizzoni, "An adaptive algorithm for hybrid electric vehicle energy management based on driving pattern recognition," *in Proc. ASME Int. Mech. Eng. Congr. Expo*., Jan. 2006, pp. 249–258.

[96] F. Borrelli, A. Bemporad, M. Fodor, and D. Hrovat, "An MPC/hybrid system approach to traction control," *IEEE Transactions on Control Systems Technology*, vol. 14, no. 3, pp. 541–552, May 2006.

[97] N. Giorgetti, G. Ripaccioli, A. Bemporad, I. V. Kolmanovsky, and D. Hrovat, "Hybrid model predictive control of direct injection stratified charge engines," *IEEE/ASME Transactions on Mechatronics*, vol. 11, no. 5, pp. 499–506, Oct. 2006.

[98] D. Corona and B. De Schutter, "Adaptive cruise control for a SMART car: A comparison benchmark for MPC-PWA control methods," *IEEE Transactions on Control Systems Technology*, vol. 16, no. 2, pp. 365–372, Mar. 2008.

[99] J. Ji, A. Khajepour, W. Melek, and Y. Huang, "Path planning and tracking for vehicle collision avoidance based on model predictive control with multi-constraints," *IEEE Transactions on Vehicular Technology*, pp. 1–1, 2016.

[100] D. Zhao, C. Liu, R. Stobart, J. Deng, E. Winward, and G. Dong, "An explicit model predictive control framework for Turbocharged diesel engines," *IEEE Transactions on Industrial Electronics*, vol. 61, no. 7, pp. 3540–3552, Jul. 2014.

[101] O. Konig, C. Hametner, G. Prochart, and S. Jakubek, "Battery Emulation for Power-HIL using local model networks and robust Impedance control," *IEEE Transactions on Industrial Electronics*, vol. 61, no. 2, pp. 943–955, Feb. 2014.

[102] L. Johannesson, M. Asbogard, and B. Egardt, "Assessing the potential of predictive control for hybrid vehicle Powertrains using stochastic dynamic programming," *IEEE Transactions on Intelligent Transportation Systems*, vol. 8, no. 1, pp. 71–83, Mar. 2007.

[103] G. Ripaccioli, D. Bernardini, S. Di Cairano, A. Bemporad, & I. Kolmanovsky, "A stochastic model predictive control approach for series hybrid electric vehicle power management," *In American Control Conference*, IEEE, pp. 5844-5849, Jun, 2010

[104] S. Fekri, and F. Assadian, "Fast Model Predictive Control and its Application to Energy Management of Hybrid Electric Vehicles," *INTECH Open Access Publisher*, 2011.

[105] F. Yan, J. Wang, and K. Huang, "Hybrid electric vehicle model predictive control torque-split strategy incorporating engine transient characteristics," *IEEE Transactions on Vehicular Technology*, vol. 61, no. 6, pp. 2458–2467, Jul. 2012.

[106] Y. L. Murphey, J. Park, Z. Chen, M. L. Kuang, M. A. Masrur, and A. M. Phillips, "Intelligent hybrid vehicle power Control—Part I: Machine learning of optimal vehicle power," *IEEE Transactions on Vehicular Technology*, vol. 61, no. 8, pp. 3519–3530, Oct. 2012.

[107] Y. L. Murphey *et al.*, "Intelligent hybrid vehicle power Control—Part II: Online intelligent energy management," *IEEE Transactions on Vehicular Technology*, vol. 62, no. 1, pp. 69–79, Jan. 2013.

[108] H. Borhan, A. Vahidi, A. M. Phillips, M. L. Kuang, I. V. Kolmanovsky, and S. Di Cairano, "MPC-Based energy management of a power-split hybrid electric vehicle," *IEEE Transactions on Control Systems Technology*, vol. 20, no. 3, pp. 593–603, May 2012.

[109] S. Kermani, S. Delprat, T. M. Guerra, R. Trigui, and B. Jeanneret, "Predictive energy management for hybrid vehicle," *Control Engineering Practice*, vol. 20, no. 4, pp. 408–420, Apr. 2012.

[110] F. A. Bender, M. Kaszynski, and O. Sawodny, "Drive cycle prediction and energy management optimization for hybrid hydraulic vehicles," *IEEE Transactions on Vehicular Technology*, vol. 62, no. 8, pp. 3581–3592, Oct. 2013.

[111] A. Styler, and I. Nourbakhsh, "Model predictive control with uncertainty in human driven systems," *In Twenty-Seventh AAAI Conference on Artificial Intelligence*, Jun. 2013.

[112] D. F. Opila, X. Wang, R. McGee, and J. W. Grizzle, "Real-time implementation and hardware testing of a hybrid vehicle energy management controller based on stochastic dynamic programming," *Journal of Dynamic Systems, Measurement, and Control*, vol. 135, no. 2, p. 021002, Nov. 2012.

[113] S. Di Cairano, D. Bernardini, A. Bemporad, and I. V. Kolmanovsky, "Stochastic MPC with learning for driver-predictive vehicle control and its application to HEV energy management," *IEEE Transactions on Control Systems Technology*, vol. 22, no. 3, pp. 1018–1031, May 2014.

[114] F. Soriano, M. Moreno-Eguilaz, and J. Alvarez-Florez, "Drive cycle identification and energy demand estimation for refuse-collecting vehicles," *IEEE Transactions on Vehicular Technology*, vol. 64, no. 11, pp. 4965–4973, Nov. 2015.

[115] A. Santucci, A. Sorniotti, and C. Lekakou, "Power split strategies for hybrid energy storage systems for vehicular applications," *Journal of Power Sources*, vol. 258, pp. 395–407, Jul. 2014.

[116] C. Sun, S. J. Moura, X. Hu, J. K. Hedrick, and F. Sun, "Dynamic traffic feedback data enabled energy management in plug-in hybrid electric vehicles," *IEEE Transactions on Control Systems Technology*, vol. 23, no. 3, pp. 1075–1086, May 2015.

[117] X. Zeng and J. Wang, "A parallel hybrid electric vehicle energy management strategy using stochastic model predictive control with road grade preview," *IEEE Transactions on Control Systems Technology*, vol. 23, no. 6, pp. 2416–2423, Nov. 2015.

[118] L. Li, S. You, C. Yang, B. Yan, J. Song, and Z. Chen, "Driving-behavior-aware stochastic model predictive control for plug-in hybrid electric buses," *Applied Energy*, vol. 162, pp. 868–879, Jan. 2016.

[119] T. Liu, Y. Zou, D. Liu, and F. Sun, "Reinforcement learning of Adaptive energy management with transition probability for a hybrid electric tracked vehicle," *IEEE Transactions on Industrial Electronics*, vol. 62, no. 12, pp. 7837–7846, Dec. 2015.

[120] C. Sun, X. Hu, S. J. Moura, and F. Sun, "Velocity predictors for predictive energy management in hybrid electric vehicles," *IEEE Transactions on Control Systems Technology*, vol. 23, no. 3, pp. 1197–1204, May 2015.

[121] X. Li, Z. Sun, D. Cao, Z. He, and Q. Zhu, "Real-time trajectory planning for autonomous urban driving: Framework, Algorithms, and Verifications," *IEEE/ASME Transactions on Mechatronics*, vol. 21, no. 2, pp. 740–753, Apr. 2016.

[122] Q. Gong, Y. Li, and Z.-R. Peng, "Trip-based optimal power management of plug-in hybrid electric vehicles," *IEEE Transactions on Vehicular Technology*, vol. 57, no. 6, pp. 3393–3401, Nov. 2008.

[123] L. Erlston, and M. Miles, "Retrofittable Regenerative Braking in Heavy Vehicle Applications," *SAE Technical Paper* 2008-01-2558, 2008, doi:10.4271/2008-01-2558.

[124] G. Rizzoni, L. Guzzella, and B. M. Baumann, "Unified modeling of hybrid electric vehicle drivetrains," *IEEE/ASME Transactions on Mechatronics*, vol. 4, no. 3, pp. 246–257, 1999.

[125] Refrigerant reference guide. 4th edition. Philadelphia, Pennsylvania: National Refrigerants, Inc., 2006. http://www.refrigerants.com/ReferenceGuide2006.pdf.

[126] E. K. Nejad, "Modeling and Second law based optimization of plate fin and tube heat exchanger using MOPSO," *Journal of Applied Mechanical Engineering*, vol. 02, no. 02, 2013.

[127] J. M. S. Jabardo and W. G. Mamani, "Modeling and experimental evaluation of parallel flow micro channel condensers," *Journal of the Brazilian Society of Mechanical Sciences and Engineering*, vol. 25, no. 2, Apr. 2003.

[128] S. Mohagheghi Fard. "A New Regenerative Anti-Idling System for Service Vehicles: Load Identification, Optimal Power Management." *Ph.D. dissertation*, University of waterloo, Canada, 2016.

[129] Y. Huang, A. Khajepour, F. Bagheri, and M. Bahrami, "Modelling and optimal energy-saving control of automotive air-conditioning and refrigeration systems," *Proceedings of the Institution of Mechanical Engineers, Part D: Journal of Automobile Engineering*, Mar. 2016.

[130] Y. Huang, A. Khajepour, M. Khazraee, M. Bahrami, "A Comparative Study of the Energy-saving Controllers for Automotive Air-conditioning/Refrigeration Systems," *Journal of Dynamic Systems, Measurement, and Control*, 2016.

[131] G. Hogh and R. Nielsen, "Model Based Nonlinear Control of Refrigeration Systems," *M.S. thesis*, AAU, Section for Automation and Control, 2008.

[132] H. Glaoui, A. Hazzab, B. Boussemaha, and I. Bousserhane, "SISO and MIMO Sliding Mode Control for Web Winding System," *International Electrical Engineering Journal (IEEJ)*, Vol. 2 No. 3, pp. 581-588, 2011.

[133] A. Benamor, L. Chrifi-alaui, H. Messaoud, and M. Chaabane, "Sliding mode control, with integrator, for a class of Mimo Nonlinear systems," *Engineering*, vol. 03, no. 05, pp. 435–444, 2011.

[134] L. Grüne and J. Pannek, "Nonlinear Model Predictive Control-Theory and algorithms," © *Springer-Verlag* London Limited, 2011.

[135] F. Borrelli, A. Bemporad, and M. Morari. Predictive control for linear and hybrid systems. http://www.mpc.berkeley.edu/mpc-course-material/MPC_Book.pdf. Accessed: 2016-08-03.

[136] H. J. Ferreau, C. Kirches, A. Potschka, H. G. Bock, and M. Diehl, "QpOASES: A parametric active-set algorithm for quadratic programming," *Mathematical Programming Computation*, vol. 6, no. 4, pp. 327–363, Apr. 2014.

[137] A. Gustavsson, "Dynamic modeling and Model Predictive Control of a vapor compression system," *Ph.D. dissertation*, Department of Electrical Engineering, Automatic Control. Linköping University, The Institute of Technology, Linköping University, 2012

[138] A. Bemporad, M. Morari, and N. Ricker, "Model Predictive Control Toolbox 3 User's Guide," *The Mathworks*, 2010.

[139] P. O. M. Scokaert and J. B. Rawlings, "Constrained linear quadratic regulation," *IEEE Transactions on Automatic Control*, vol. 43, no. 8, pp. 1163–1169, 1998.

[140] N. Jain, *et al*. "Model Predictive Control of Variable Refrigerant Flow Systems," *The International Refrigeration and Air Conditioning Conference*, 2014.

[141] L. Fagiano and A. R. Teel, "Generalized terminal state constraint for model predictive control," *Automatica*, vol. 49, no. 9, pp. 2622–2631, Sep. 2013.

[142] L. Fagiano, and A. R. Teel, "On generalized terminal state constraints for model predictive control, 2013, http://arxiv.org/abs/1207.0788v2, Accessed: 2016-08-03.

[143] C. Tian, X. Li, and X. Yang, "Numerical analysis of evaporator frosting in automotive air-conditioning system with a variable-displacement compressor," *Applied Energy*, vol. 82, no. 1, pp. 1–22, Sep. 2005.

[144] M. K. Yoong, *et al*. "Studies of Regenerative Braking in Electric Vehicle," *IEEE Conference on Sustainable Utilization and Development in Engineering and Technology*, Nov. 2010.

[145] J. M. Olafsdottir, "Integrated vehicle dynamics control for energy recuperation in fully electric vehicles." M.S. thesis , Chalmers *University* of Technology, Goteborg, Sweden, 2011.

[146] M. Ehsani, Y. Gao, S. E. Gay and A. Emadi, "Modern Electric, Hybrid Electric, and Fuel Cell Vehicles," *CRC Press LCC*, Boca Raton, U.S., 2005.

[147] J. Guo, J. Wang and B. Cao, "Regenerative Braking Strategy for Electric Vehicles," *IEEE Intelligent Vehicles Symposium*, Jun. 2009.

[148] O. Nelles, "Nonlinear system identification: from classical approaches to neural networks and fuzzy models," *Springer Science & Business Media*; 2013 Mar 9.

[149] Website: http://www.gmc.com/vans/savana-cargo-van/features-specs/trims.html, Accessed: 016-08-03.

[150] H. Wang, Y. Huang, A. Khajepour, and Q. Song, "Model predictive control-based energy management strategy for a series hybrid electric tracked vehicle," *Applied Energy*, vol. 182, pp. 105–114, Nov. 2016.

[151] J. Liu and H. Peng, "Modeling and control of a power-split hybrid vehicle," *IEEE Transactions on Control Systems Technology*, vol. 16, no. 6, pp. 1242–1251, Nov. 2008.

[152] Y. Huang, A. Khajepour, and H. Wang, "A predictive power management controller for service vehicle anti-idling systems without a priori information," *Applied Energy*, vol. 182, pp. 548–557, Nov. 2016.

Appendix A

The complete version of the simplified A/C-R system model:

$\dot{x}$	$f(x,u)$	f_{12x}	$\left(\dot{m}_v \frac{dh_{ge}}{dP_e} + \alpha_i A_i \frac{l_e}{L_e}\frac{dT_{re}}{dP_e}\right) \Big/ \left(\rho_{le} h_{lge} A_e (1-\bar{\gamma}_e)\right)$
y	$g(x,u)$	f_{13x}	$-\alpha_i A_i l_e \Big/ \left(\rho_{le} h_{lge} A_e (1-\bar{\gamma}_e) L_e\right)$
u	$\left[N_{comp}, N_{evap}, N_{cond}\right]^T$	f_{22x}	$\left(\dot{m}_v \frac{dh_{le}}{dP_e} - \alpha_i A_i \frac{l_e}{L_e}\frac{dT_{re}}{dP_e}\right) \Big/ \left(h_{lge} A_e L_e \frac{d\rho_{ge}}{dP_e}\right)$
x	$\left[l_e, P_e, T_{we}, P_c, T_{wc}, T_{cargo}\right]^T$	f_{23x}	$\alpha_i A_i l_e \Big/ \left(h_{lge} A_e L_e^{\,2} \frac{d\rho_{ge}}{dP_e}\right)$
y	T_{cargo}	f_{24x}	$\dot{m}_v \frac{dh_{ie}}{dP_c} \Big/ \left(h_{lge} A_e L_e \frac{d\rho_{ge}}{dP_e}\right)$
$f = \begin{bmatrix} f_1 \\ f_2 \\ f_3 \\ f_4 \\ f_5 \\ f_6 \end{bmatrix}$	$\begin{bmatrix} \left(\dot{m}_v\left(h_{ge}-h_{ie}\right)-\alpha_{ie}\pi D_{ie} l_e \left(T_{wfe}-T_{re}\right)\right)\Big/\left(\rho_{le} h_{lge} A_e (1-\bar{\gamma}_e)\right) \\ \left(\dot{m}_v \frac{h_{ie}-h_{le}}{h_{lge}} - \dot{m}_{comp} + \frac{\alpha_{ie}\pi D_{ie} l_e \left(T_{wfe}-T_{re}\right)}{h_{lge}}\right)\Big/\left(A_e L_e \frac{d\rho_{ge}}{dP_e}\right) \\ \left(\alpha_{oe} A_{oe}\left(T_{ae}-T_{wfe}\right)-\alpha_{ie}\pi D_{ie} l_e \left(T_{wfe}-T_{re}\right)\right)\Big/\left(C_p m\right)_{we} \\ \left(-\alpha_{iesh}\pi D_{ie}(L_e-l_e)\left(T_{wfe}-T_{re}\right)\right)\Big/\left(C_p m\right)_{we} \\ \left(\dot{m}_{com} - \frac{\alpha_{ic}\pi D_{ic} l_c \left(T_{rc}-T_{wc}\right)}{h_{lgc}}\right)\Big/\left(A_c L_c \frac{d\rho_{gc}}{dP_c}\right) \\ \left(\dot{m}_{comp} - \frac{\alpha_{ic}\pi D_{ic} l_c \left(T_{rc}-T_{wfc}\right)}{h_{lgc}}\right)\Big/\left(C_p m\right)_{wc} \\ \left(\dot{Q}_{out} - \alpha_o A_o l_e \left(T_a - T_{we}\right)\right)\Big/\left(MC\right)_{air} \end{bmatrix}$	f_{32x}	$\alpha_i A_i \frac{dT_{re}}{dP_e} \Big/ \left(C_p m\right)_{we}$
		f_{33x}	$-\alpha_i A_i + \alpha_o A_o \left(\frac{dT_a}{dT_{we}} - 1\right) \Big/ \left(C_p m\right)_{we}$
		f_{36x}	$\alpha_o A_o \left(\frac{dT_a}{dT_{cargo}}\right) \Big/ \left(C_p m\right)_{we}$
		f_{41x}	$-\alpha_{ic} A_{ic} \left(T_{rc} - T_{wc}\right) \frac{\partial l_c}{\partial l_e} \Big/ \left(h_{lgc} A_c L_c^{\,2} \frac{d\rho_{gc}}{dP_c}\right)$
		f_{44x}	$-\alpha_{ic} A_{ic} l_c \frac{dT_{rc}}{dP_c} \Big/ \left(h_{lge} A_c L_c^{\,2} \frac{d\rho_{gc}}{dP_c}\right)$
		f_{45x}	$\alpha_{ic} A_{ic} l_c \Big/ \left(h_{lge} A_c L_c^{\,2} \frac{d\rho_{gc}}{dP_c}\right)$
$g(x,u)$	x_6	f_{54x}	$\alpha_{ic} A_{ic} \frac{dT_{rc}}{dP_c} \Big/ \left(C_p m\right)_{wc}$
A_c	$\begin{bmatrix} f_{11x} & f_{12x} & f_{13x} & f_{14x} & 0 & 0 \\ f_{21x} & f_{22x} & f_{23x} & f_{24x} & 0 & 0 \\ 0 & f_{32x} & f_{33x} & 0 & f_{35x} & 0 \\ f_{41x} & 0 & 0 & f_{44x} & f_{45x} & 0 \\ 0 & 0 & 0 & f_{54x} & f_{55x} & 0 \\ f_{61x} & 0 & f_{63x} & 0 & 0 & f_{66x} \end{bmatrix}$	f_{55x}	$-\alpha_{ic} A_{ic} + \alpha_{oc} A_{oc} \left(\left(\frac{dT_{ac}}{dT_{wc}} - 1\right)\right) \Big/ \left(C_p m\right)_{wc}$
		f_{61x}	$-\alpha_o A_o \left(T_a - T_{we}\right) \Big/ \left(MC\right)_{air}$
		f_{63x}	$-\alpha_o A_o l_e \left(\frac{dT_a}{dT_{we}} - 1\right) \Big/ \left(MC\right)_{air}$

		f_{66x}	$-\alpha_o A_o l_e \left(\frac{dT_a}{dT_{cargo}} \right) \Big/ \left(MC \right)_{air}$
B_c	$\begin{bmatrix} f_{11u} & 0 & 0 \\ f_{21u} & f_{22u} & 0 \\ 0 & 0 & f_{33u} \\ 0 & f_{42u} & 0 \\ 0 & 0 & 0 \\ 0 & 0 & f_{63u} \end{bmatrix}$	f_{11u}	$-\left(h_{ie} - h_{ge} \right) \frac{d\dot{m}_v}{du_v} \Big/ \left(\rho_{le} h_{lge} A_e \left(1 - \bar{\gamma}_e \right) \right)$
		f_{21u}	$\frac{h_{ie} - h_{le}}{h_{lge}} \frac{d\dot{m}_v}{du_v} \Big/ \left(A_e L_e \frac{d\rho_{ge}}{dP_e} \right)$
		f_{22u}	$-\frac{d\dot{m}_{comp}}{dN_{comp}} \Big/ \left(A_e L_e \frac{d\rho_{ge}}{dP_e} \right)$
		f_{33u}	$\left(\frac{d\alpha_o}{dN_{evap}} A_o \left(T_a - T_{we} \right) + \alpha_o A_o \frac{dT_a}{d\alpha_o} \frac{d\alpha_o}{dN_{evap}} \right) \Big/ \left(C_p m \right)_{we}$
C_c	$\begin{bmatrix} 0 & 0 & 0 & 0 & 0 & 1 \end{bmatrix}$	f_{42u}	$\frac{d\dot{m}_{comp}}{dN_{comp}} \Big/ \left(A_c L_c \frac{d\rho_{gc}}{dP_c} \right)$
f_{11x}	$-\alpha_i A_i \left(T_{we} - T_{re} \right) \Big/ \rho_{le} h_{lge} A_e \left(1 - \bar{\gamma}_e \right) L_e$	f_{63u}	$\left(-\frac{d\alpha_o}{dN_{evap}} A_o l_e \left(T_a - T_{we} \right) - \alpha_o A_o l_e \frac{dT_a}{d\alpha_o} \frac{d\alpha_o}{dN_{evap}} \right) \Big/ \left(\left(MC \right)_{air} \right)$

Appendix B

The discrete-time model of the whole system:

$\begin{cases} x(k+1) = A(k)x(k) + B_u(k)u(k) + B_v(k) \\ y(k) = C(k)x(k) \end{cases}$	$A(k) = \begin{bmatrix} A_d & 0 \\ 0 & 1 \end{bmatrix}$
$x = \left[P_e, P_c, l_e, T_{wfe}, T_{wfc}, T_{cargo}, SOC \right]^T$	$B_u(k) = \begin{bmatrix} B_d & 0 \\ 0 & \dfrac{\eta_{gen}\eta_{char}}{V_{OC}C_{batt}} \end{bmatrix}$
$u = \left[N_{comp}, N_{evap}, N_{cond}, P_{eng \to alt} \right]^T$	$B_v(k) = \left[0 \quad 0 \quad 0 \quad 0 \quad 0 \quad 0 \quad \dfrac{\eta_{reg}\eta_{char}P_{veh}}{V_{OC}C_{batt}} + \dfrac{P_{aux}}{V_{OC}C_{batt}\eta_{disc}} \right]^T$
$y = \left[T_{cargo}, SOC \right]^T$	$C(k) = \begin{bmatrix} 0 & 0 & 0 & 0 & 0 & 1 & 0 \\ 0 & 0 & 0 & 0 & 0 & 0 & 1 \end{bmatrix}$

where A_d and B_d are the discrete version of the A_c and B_c in Appendix A.